

¹ A Search in the Two-Photon Final State for
² Evidence of New Particle Production in pp
³ Collisions at $\sqrt{s} = 7$ TeV

⁴ Rachel P. Yohay
University of Virginia
`rpy3y@virginia.edu`

⁵ May 6, 2012

Contents

7	1	Overview of the Standard Model of Particle Physics	3
8	1.1	Particle Content	6
9	1.2	Electroweak Symmetry Breaking and the Higgs Mechanism	6
10	1.3	The Hierarchy Problem, The Origins of Mass, and Fine Tuning	6
11	2	The Supersymmetric Extension to the Standard Model	7
12	2.1	Supermultiplet Representation	7
13	2.2	The Unbroken SUSY Lagrangian	8
14	2.3	Soft SUSY Breaking	14
15	2.4	Gauge-Mediated SUSY Breaking	16
16	2.5	Phenomenology of General Gauge Mediation	19
17	2.6	Experimental Status of SUSY	23
18	3	Event Selection	29
19	3.1	Object Reconstruction	30
20	3.1.1	Photons	30
21	3.1.2	Electrons	41
22	3.1.3	Jets and Missing Transverse Energy	41
23	3.2	HLT	47
24	3.3	Event Quality	50
25	3.4	Photon Identification Efficiency	52

26	3.4.1 Tag and Probe Method	54
27	3.4.2 Photon Efficiency Scale Factor $\epsilon_e^{\text{data}}/\epsilon_e^{\text{MC}}$	57
28	4 Data Analysis	63
29	4.1 Modeling the QCD Background	67
30	4.1.1 Outline of the Procedure	67
31	4.1.2 Reweighting	68
32	4.1.3 Normalization	79
33	4.2 Modeling the Electroweak Background	79
34	4.3 Errors on the Background Prediction	85
35	4.4 Results	93
36	5 Interpretation of Results in Terms of GMSB Models	97
37	5.1 Simplified Models	97
38	5.2 Upper Limit Calculation	97
39	5.2.1 Signal Acceptance \times Efficiency	98
40	5.2.2 CL_s and the Profile Likelihood Test Statistic	98
41	5.3 Translation of Upper Limits to Model Exclusions	98
42	5.4 Cross Section Upper Limits	98
43	5.5 Exclusion Contours	98
44	A Monte Carlo Samples	99
45	A.0.1 List of Samples	99
46	A.0.2 Explanation of Naming Conventions	100

⁴⁷ **Chapter 1**

⁴⁸ **Overview of the Standard Model of
Particle Physics**

⁵⁰ In the 1960s, Sheldon Glashow, Steven Weinberg, and Abdus Salam proposed a math-
⁵¹ ematical framework that unified the electromagnetic and weak forces at an energy
⁵² scale in the hundreds of GeV/c, as well as a mechanism for breaking the electroweak
⁵³ symmetry at low energies [1]. At the same time, Murray Gell-Mann introduced the
⁵⁴ concept of quarks to describe hadron spectroscopy, a concept that would later grow
⁵⁵ into quantum chromodynamics (QCD), the full theory of the strong force [2]. These
⁵⁶ two key developments motivated the unified representation of particle physics as a
⁵⁷ set of fields whose dynamics are invariant under the Standard Model gauge group

$$SU(3)_C \otimes SU(2)_L \otimes U(1)_{EM} \quad (1.1)$$

⁵⁸ where $SU(3)_C$ describes the quark QCD interactions, $SU(2)_L$ describes the weak
⁵⁹ interactions among quarks and leptons, and $U(1)_{EM}$ describes the electromagnetic
⁶⁰ interaction.

⁶¹ The Standard Model, in particular the electroweak theory, has been an extremely
⁶² successful predictor of particle production and interaction cross-sections and decay

63 rates, as well as of the exact masses of the electroweak force carriers. The case for
64 the validity of the Standard Model was bolstered by the many precision QCD and
65 electroweak measurements carried out at the Large Electron-Positron (LEP) collider,
66 which ran from 1989-2000 at center-of-mass energies between 65 and 104 GeV/c [3].
67 Figure 1.1 shows some of the highlights of the LEP program.

68 However, there are still deep theoretical problems with the Standard Model, stem-
69 ming from the introduction of the Higgs scalar into the theory to break electroweak
70 symmetry [4]. Since the Higgs self-energy diagram is quadratically sensitive to the
71 ultraviolet cutoff scale(footnote: this is a general property of scalar fields), and as-
72 suming that there are no new important energy scales of physics between the weak
73 scale ($\mathcal{O}(10^2 \text{ GeV}/c)$) and the Planck scale ($\mathcal{O}(10^{19} \text{ GeV}/c)$), in order to be consistent
74 with experimental measurements, this diagram must include a remarkable 17-orders-
75 of-magnitude cancellation that is otherwise poorly motivated [5]. The quest to find
76 new physics at an intermediate energy scale between the weak and Planck scales, and
77 thus extend the Standard Model, was the driving force behind the construction of the
78 Large Hadron Collider (LHC) in 2009, the world's highest energy particle accelerator
79 to date.

80 In this chapter I will briefly describe the Standard Model particle content, the the-
81 ory and major results of electroweak symmetry breaking (EWSB), and the problems
82 that the Standard Model is as yet ill-prepared to address.

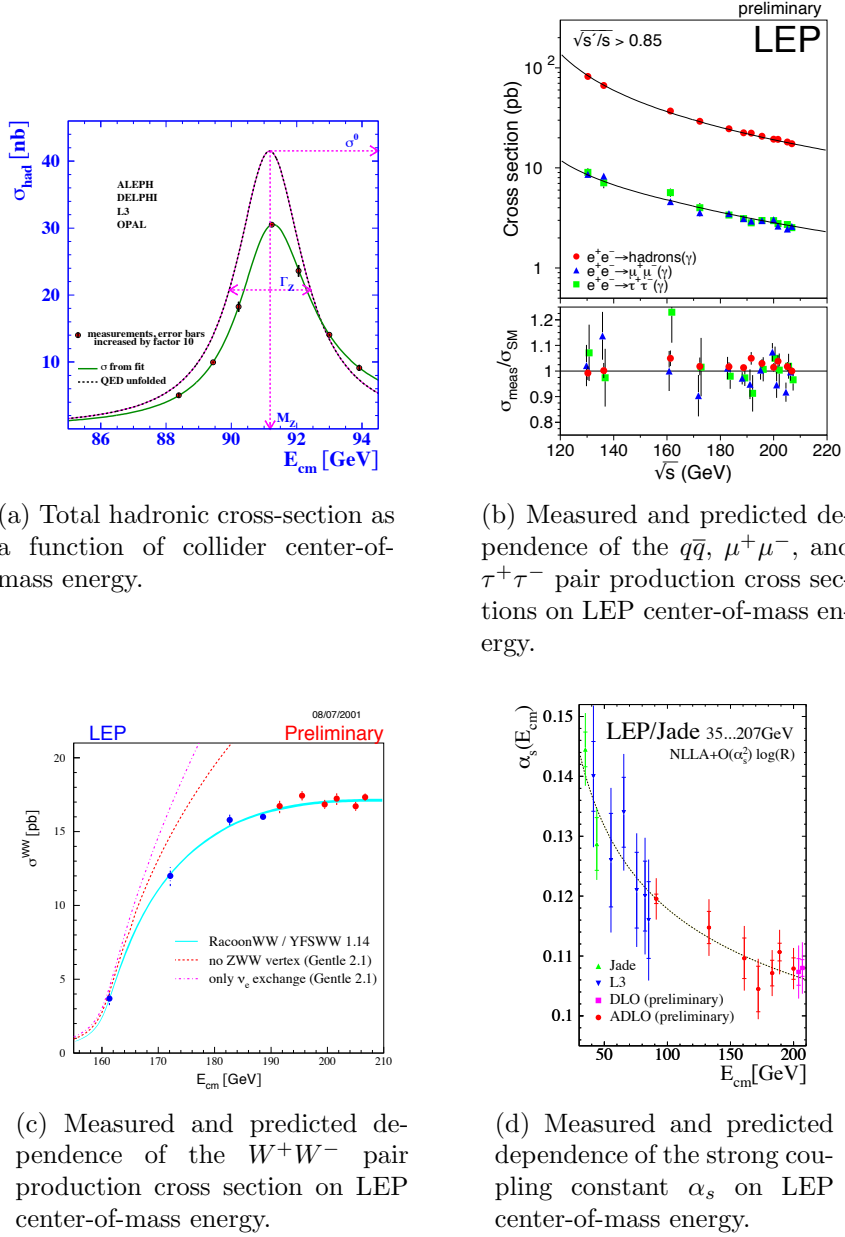


Figure 1.1: Selected LEP measurements demonstrating its contribution to the precise understanding of the Standard Model. Reprinted from [3].

⁸³ **1.1 Particle Content**

⁸⁴ **1.2 Electroweak Symmetry Breaking and the Higgs Mechanism**

⁸⁵ ⁸⁶ **1.3 The Hierarchy Problem, The Origins of Mass, and Fine Tuning**

⁸⁷

⁸⁸ **Chapter 2**

⁸⁹ **The Supersymmetric Extension to
⁹⁰ the Standard Model**

⁹¹ The following introduction to SUSY focuses primarily on the aspects of the formalism that are relevant to phenomenology. In particular, most of the details of SUSY breaking (about which there is little theoretical consensus) are omitted, except where they are relevant to experiment. The notation is similar to that used in refs. [5] and [6], and much of the information presented is culled from those references.

⁹⁶ **2.1 Supermultiplet Representation**

⁹⁷ The Standard Model is extended to include supersymmetry by the introduction of a supersymmetry transformation that takes fermionic states to bosonic states and vice versa. The resulting model is called the *minimal supersymmetric Standard Model* (MSSM). In analogy with the known symmetries of the Standard Model, the SUSY transformation has associated generators that obey defining commutation and anti-commutation relations, and a fundamental representation. All SM particles and their superpartners fall into one of two *supermultiplet* representations. Using the property that

$$n_F = n_B, \quad (2.1)$$

105 where n_F is the number of fermionic degrees of freedom per supermultiplet and n_B is
106 the number of bosonic degrees of freedom, the two types of supermultiplets are

- 107 1. *Chiral supermultiplets*: one Weyl fermion (two helicity states $\Rightarrow n_F = 2$) and
108 one complex scalar field (with two real components $\Rightarrow n_B = 2$)
- 109 2. *Gauge supermultiplets*: One spin-1 vector boson (two helicity states $\Rightarrow n_B = 2$)
110 and one Weyl fermion (two helicity states $\Rightarrow n_F = 2$)

111 In the gauge supermultiplet, the vector boson is assumed massless (i.e. before
112 EWSB generates a mass for it). Since the superpartners to the SM particles have not
113 yet been discovered, they must be significantly heavier than their SM counterparts.
114 Unbroken SUSY predicts that the SM particles and their superpartners must have
115 exactly the same mass, so ultimately a mechanism for SUSY breaking must be intro-
116 duced to generate masses for the superpartners (see Sec. 2.3). Tables 2.1 and 2.2 show
117 the chiral and gauge supermultiplets of the MSSM, respectively. Note that the scalar
118 partners to the SM fermions are denoted by placing an “s” in front of their names,
119 while the chiral fermion partners to the SM gauge bosons are denoted by appending
120 “ino” to their names.

121 2.2 The Unbroken SUSY Lagrangian

122 The first piece of the full unbroken SUSY Lagrangian density consists of the kinetic
123 and interacting terms related to the chiral supermultiplets. As explained in Sec. 2.1,
124 a chiral supermultiplet consists of a Weyl fermion ψ (the ordinary fermion) and a
125 complex scalar ϕ (the sfermion). For a collection of such chiral supermultiplets, the
126 Lagrangian is

Table 2.1: Chiral supermultiplets of the supersymmetric Standard Model. Adapted from Table 1.1 of ref. [6].

Type of supermultiplet	Notation	Spin-0 component	Spin-1/2 component	Representation under $SU(3)_C \otimes SU(2)_L \otimes U(1)_Y$
Left-handed quark/squark doublet ($\times 3$ families)	Q	$(\tilde{u}_L \tilde{d}_L)$	$(u_L d_L)$	$(\mathbf{3}, \mathbf{2}, \frac{1}{6})$
Right-handed up-type quark/squark singlet ($\times 3$ families)	\bar{u}	\tilde{u}_R^*	u_R^\dagger	$(\bar{\mathbf{3}}, \mathbf{1}, -\frac{2}{3})$
Right-handed down-type quark/squark singlet ($\times 3$ families)	\bar{d}	\tilde{d}_R^*	d_R^\dagger	$(\bar{\mathbf{3}}, \mathbf{1}, \frac{1}{3})$
Left-handed lepton/slepton doublet ($\times 3$ families)	L	$(\tilde{\nu}_{eL} \tilde{e}_L)$	$(\bar{\nu}_{eL} e_L)$	$(\mathbf{1}, \mathbf{2}, -\frac{1}{2})$
Right-handed lepton/slepton singlet ($\times 3$ families)	\bar{e}	\tilde{e}_R^*	e_R^\dagger	$(\bar{\mathbf{1}}, \mathbf{1}, 1)$
Up-type Higgs/Higgsino doublet	H_u	$(H_u^+ H_u^0)$	$(\tilde{H}_u^+ \tilde{H}_u^0)$	$(\mathbf{1}, \mathbf{2}, \frac{1}{2})$
Down-type Higgs/Higgsino doublet	H_d	$(H_d^0 H_d^-)$	$(\tilde{H}_d^0 \tilde{H}_d^-)$	$(\mathbf{1}, \mathbf{2}, -\frac{1}{2})$

Table 2.2: Gauge supermultiplets of the supersymmetric Standard Model. Adapted from Table 1.2 of ref. [6].

Type of supermultiplet	Spin-1/2 component	Spin-1 component	Representation under $SU(3)_C \otimes SU(2)_L \otimes U(1)_Y$
Gluon/gluino	\tilde{g}	g	$(\mathbf{8}, \mathbf{1}, 0)$
W/wino	$\tilde{W}^\pm \tilde{W}^0$	$W^\pm W^0$	$(\mathbf{1}, \mathbf{3}, 0)$
B/bino	\tilde{B}^0	B^0	$(\mathbf{1}, \mathbf{1}, 0)$

$$\begin{aligned}\mathcal{L}_{\text{chiral}} = & -\partial^\mu \phi^{*i} \partial_\mu \phi_i - V_{\text{chiral}}(\phi, \phi^*) - i\psi^{\dagger i} \bar{\sigma}^\mu \partial_\mu \psi_i - \frac{1}{2} M^{ij} \psi_i \psi_j \\ & - \frac{1}{2} M_{ij}^* \psi^{\dagger i} \psi^{\dagger j} - \frac{1}{2} y^{ijk} \phi_i \psi_j \psi_k - \frac{1}{2} y_{ijk}^* \phi^{*i} \psi^{\dagger j} \psi^{\dagger k}\end{aligned}\quad (2.2)$$

where i runs over all supermultiplets in Table 2.1, $\bar{\sigma}^\mu$ are $-1 \times$ the Pauli matrices (except for $\sigma^0 = \bar{\sigma}^0$), M^{ij} is a mass matrix for the fermions, y^{ijk} are the Yukawa couplings between one scalar and two spinor fields, and $V_{\text{chiral}}(\phi, \phi^*)$ is the scalar potential

$$\begin{aligned}V_{\text{chiral}}(\phi, \phi^*) = & M_{ik}^* M^{kj} \phi^{*i} \phi_j + \frac{1}{2} M^{in} y_{jkn}^* \phi_i \phi^{*j} \phi^{*k} \\ & + \frac{1}{2} M_{in}^* y^{jkn} \phi^{*i} \phi_j \phi_k + \frac{1}{4} y^{ijn} y_{klm}^* \phi_i \phi_j \phi^{*k} \phi^{*l}.\end{aligned}\quad (2.3)$$

The Lagrangian can also be written as the kinetic terms plus derivatives of the *superpotential* W :

$$\begin{aligned}\mathcal{L}_{\text{chiral}} = & -\partial^\mu \phi^{*i} \partial_\mu \phi_i - i\psi^{\dagger i} \bar{\sigma}^\mu \partial_\mu \psi_i \\ & - \frac{1}{2} \left(\frac{\delta^2 W}{\delta \phi^i \delta \phi^j} \psi_i \psi_j + \frac{\delta^2 W^*}{\delta \phi_i \delta \phi_j} \psi^{\dagger i} \psi^{\dagger j} \right) - \frac{\delta W}{\delta \phi^i} \frac{\delta W^*}{\delta \phi_i}\end{aligned}\quad (2.4)$$

where

$$W = M^{ij} \phi_i \phi_j + \frac{1}{6} y^{ijk} \phi_i \phi_j \phi_k. \quad (2.5)$$

The second part of the Lagrangian involves the gauge supermultiplets. In terms of the spin-1 ordinary gauge boson A_μ^a and the spin-1/2 Weyl spinor gaugino λ^a of

¹³⁶ the gauge supermultiplet, where a runs over the number of generators for the SM
¹³⁷ subgroup (i.e. 1-8 for $SU(3)_C$, 1-3 for $SU(2)_L$, and 1 for $U(1)_Y$), this part of the
¹³⁸ Lagrangian is

$$\mathcal{L}_{\text{gauge}} = -\frac{1}{4}F_{\mu\nu}^a F^{\mu\nu a} - i\lambda^{\dagger a}\bar{\sigma}^\mu D_\mu \lambda^a + \frac{1}{2}D^a D^a \quad (2.6)$$

¹³⁹ where

$$F_{\mu\nu}^a = \partial_\mu A_\nu^a - \partial_\nu A_\mu^a + g f^{abc} A_\mu^b A_\nu^c \quad (2.7)$$

¹⁴⁰ (g is the coupling constant and f^{abc} are the structure constants for the particular SM
¹⁴¹ gauge group),

$$D_\mu \lambda^a = \partial_\mu \lambda^a + g f^{abc} A_\mu^b \lambda^c, \quad (2.8)$$

¹⁴² and D^a is an auxiliary field that does not propagate (in the literature, it is used as a
¹⁴³ bookkeeping tool and can be removed via its algebraic equation of motion).

¹⁴⁴ To build a fully supersymmetric and gauge-invariant Lagrangian, the ordinary
¹⁴⁵ derivatives in $\mathcal{L}_{\text{chiral}}$ (Eq. 2.2) must be replaced by covariant derivatives

$$D_\mu \phi_i = \partial_\mu \phi_i - ig A_\mu^a (T^a \phi)_i \quad (2.9)$$

$$D_\mu \phi^{*i} = \partial_\mu \phi^{*i} + ig A_\mu^a (\phi^* T^a)^i \quad (2.10)$$

$$D_\mu \psi_i = \partial_\mu \psi_i - ig A_\mu^a (T^a \psi)_i. \quad (2.11)$$

¹⁴⁶ This leads to the full Lagrangian

$$\begin{aligned}
\mathcal{L} &= \mathcal{L}_{\text{chiral}} + \mathcal{L}_{\text{gauge}} \\
&\quad - \sqrt{2}g(\phi^{*i}T^a\psi_i)\lambda^a - \sqrt{2}g\lambda^{\dagger a}(\psi^{\dagger i}T^a\phi_i) + g(\phi^{*i}T^a\phi_i)D^a \\
&= -\partial^\mu\phi^{*i}\partial_\mu\phi_i - i\psi^{\dagger i}\bar{\sigma}^\mu\partial_\mu\psi_i + ig\partial^\mu\phi^{*i}A_\mu^a(T^a\phi)_i - ig\partial_\mu\phi_iA^{\mu a}(\phi^*T^a)^i \\
&\quad - g^2A^{\mu a}(\phi^*T^a)^iA_\mu^a(T^a\phi)_i - g\psi^{\dagger i}\bar{\sigma}^\mu A_\mu^a(T^a\psi)_i - V_{\text{chiral}}(\phi, \phi^*) \\
&\quad - \frac{1}{2}M^{ij}\psi_i\psi_j - \frac{1}{2}M_{ij}^*\psi^{\dagger i}\psi^{\dagger j} - \frac{1}{2}y^{ijk}\phi_i\psi_j\psi_k - \frac{1}{2}y_{ijk}^*\phi^{*i}\psi^{\dagger j}\psi^{\dagger k} \\
&\quad - \frac{1}{4}F_{\mu\nu}^aF^{\mu\nu a} - i\lambda^{\dagger a}\bar{\sigma}^\mu\partial_\mu\lambda^a - ig\lambda^{\dagger a}\bar{\sigma}^\mu f^{abc}A_\mu^b\lambda^c + \frac{1}{2}D^aD^a \\
&\quad - \sqrt{2}g(\phi^{*i}T^a\psi_i)\lambda^a - \sqrt{2}g\lambda^{\dagger a}(\psi^{\dagger i}T^a\phi_i) + g(\phi^{*i}T^a\phi_i)D^a. \tag{2.12}
\end{aligned}$$

¹⁴⁷ Writing out $F_{\mu\nu}^a$ and $V_{\text{chiral}}(\phi, \phi^*)$ explicitly combining the D^a terms using the equation

¹⁴⁸ of motion $D^a = -g\phi^{*i}T^a\phi_i$, and rearranging some terms, the final unbroken SUSY

¹⁴⁹ Lagrangian is

$$\begin{aligned}
\mathcal{L} = & -\partial^\mu \phi^{*i} \partial_\mu \phi_i - i\psi^{\dagger i} \bar{\sigma}^\mu \partial_\mu \psi_i \\
& - \frac{1}{4} (\partial_\mu A_\nu^a - \partial_\nu A_\mu^a) (\partial^\mu A^{\nu a} - \partial^\nu A^{\mu a}) - i\lambda^{\dagger a} \bar{\sigma}^\mu \partial_\mu \lambda^a \\
& - M_{ik}^* M^{kj} \phi^{*i} \phi_j - \frac{1}{2} M^{ij} \psi_i \psi_j - \frac{1}{2} M_{ij}^* \psi^{\dagger i} \psi^{\dagger j} \\
& + ig \partial^\mu \phi^{*i} A_\mu^a (T^a \phi)_i - ig \partial_\mu \phi_i A^{\mu a} (\phi^* T^a)^i - g \psi^{\dagger i} \bar{\sigma}^\mu A_\mu^a (T^a \psi)_i \\
& - ig \lambda^{\dagger a} \bar{\sigma}^\mu f^{abc} A_\mu^b \lambda^c \\
& - \frac{1}{4} g f^{abc} [(\partial_\mu A_\nu^a - \partial_\nu A_\mu^a) A^{\mu b} A^{\nu c} + A_\mu^b A_\nu^c (\partial^\mu A^{\nu a} - \partial^\nu A^{\mu a})] \\
& - \frac{1}{2} M_{in}^* y^{jkn} \phi^{*i} \phi_j \phi_k - \frac{1}{2} M^{in} y_{jkn}^* \phi_i \phi^{*j} \phi^{*k} \\
& - \frac{1}{2} y^{ijk} \phi_i \psi_j \psi_k - \frac{1}{2} y_{ijk}^* \phi^{*i} \psi^{\dagger j} \psi^{\dagger k} \\
& - \sqrt{2} g (\phi^{*i} T^a \psi_i) \lambda^a - \sqrt{2} g \lambda^{\dagger a} (\psi^{\dagger i} T^a \phi_i) \\
& - g^2 A^{\mu a} (\phi^* T^a)^i A_\mu^a (T^a \phi)_i - \frac{1}{4} g^2 f^{abc} A_\mu^b A_\nu^c f^{abc} A^{\mu b} A^{\nu c} \\
& - \frac{1}{4} y^{ijn} y_{kln}^* \phi_i \phi_j \phi^{*k} \phi^{*l} - \frac{1}{2} g^2 (\phi^{*i} T^a \phi_i)^2.
\end{aligned} \tag{2.13}$$

150 The above Lagrangian applies to chiral supermultiplets interacting with one kind
151 of gauge supermultiplet (i.e. one SM gauge group). In the general case, there are
152 additional terms corresponding to interactions with all three SM gauge groups.

153 The following list gives a description of the terms in Eq. 2.13:

- 154 • First two lines: kinetic terms for the four types of fields ϕ_i , ψ_i , A_μ^a , and λ^a
- 155 • Third line: mass terms for the ϕ_i and ψ_i (see Figs. 2.1(a) and 2.1(b))
- 156 • Fourth and fifth lines: cubic couplings in which ϕ_i , ψ_i , or λ^a radiates an A_μ^a (see
157 Figs. 2.1(c), 2.1(d), and 2.1(e))
- 158 • Sixth line: triple gauge boson couplings (see Fig. 2.1(f))
- 159 • Seventh line: triple sfermion couplings (see Fig. 2.1(g))

- 160 • Eighth line: cubic couplings in which ψ_i radiates a ϕ_i (see Fig. 2.1(h))
- 161 • Ninth line: ϕ_i - ψ_i - λ^a vertices (see Fig. 2.1(i))
- 162 • 10th line: A_μ^a - A_μ^a - ϕ_i - ϕ_i and quadruple gauge boson couplings (see Figs. 2.1(j)
163 and 2.1(k))
- 164 • 11th line: ϕ_i^4 vertices (see Figs. 2.1(l) and 2.1(m))

165 2.3 Soft SUSY Breaking

166 Since quadratic divergences in sfermion masses vanish to all orders in perturbation
167 theory in plain unbroken SUSY [6] due to the presence of gauge and Yukawa interac-
168 tions with the necessary relationships between coupling constants, it is desirable that
169 the terms that break SUSY not disturb this property. In addition, SUSY should be
170 broken spontaneously, as electroweak symmetry is broken in the Standard Model, so
171 that it is only made manifest at high energies. To satisfy these constraints, SUSY-
172 breaking terms are simply added to the unbroken SUSY Lagrangian in Eq. 2.13 such
173 that $\mathcal{L}_{\text{total}} = \mathcal{L}_{\text{unbroken}} + \mathcal{L}_{\text{breaking}}$. The coefficients of terms in $\mathcal{L}_{\text{breaking}}$ must have
174 positive mass dimension in order not to contribute quadratically divergent loop cor-
175 rections to the scalar masses (like the Higgs mass).¹ This form of SUSY breaking is
176 called *soft*, and all coefficients of soft SUSY breaking terms are expected to be of
177 order m_{soft} or m_{soft}^2 .

¹This point can be argued via dimensional analysis. Radiative corrections take the form Δm_S^2 , where m_S is the mass of the scalar particle in question. The dimensions of Δm_S^2 are mass². Δm_S^2 is proportional to some coupling constant or mass coefficient k multiplied by a function of Λ_{UV} , the high energy cutoff scale. The function of Λ_{UV} is determined by a loop integral, and thus typically takes the form Λ_{UV}^2 (quadratically divergent) or $\ln \frac{\Lambda_{\text{UV}}}{m_{\text{low}}}$ (logarithmically divergent, where m_{low} is some other lower-mass scale in the problem). Now, if k already contributes at least one power of mass to Δm_S^2 , then the high-energy behavior—the function of Λ_{UV} —can only contribute at most one power of the dimensionful parameter Λ_{UV} . However, there are typically no loop integrals that diverge linearly in Λ_{UV} , so by forcing k to have positive mass dimension, the form of the radiative corrections contributed by SUSY-breaking terms is limited to $\Delta m_S^2 \sim m_{\text{low}}^2 \ln \frac{\Lambda_{\text{UV}}}{m_{\text{low}}}$. In effect, the possibility of dangerous corrections proportional to Λ_{UV}^2 is excluded by dimensional analysis if the requirement that k contribute at least one power of mass is enforced.

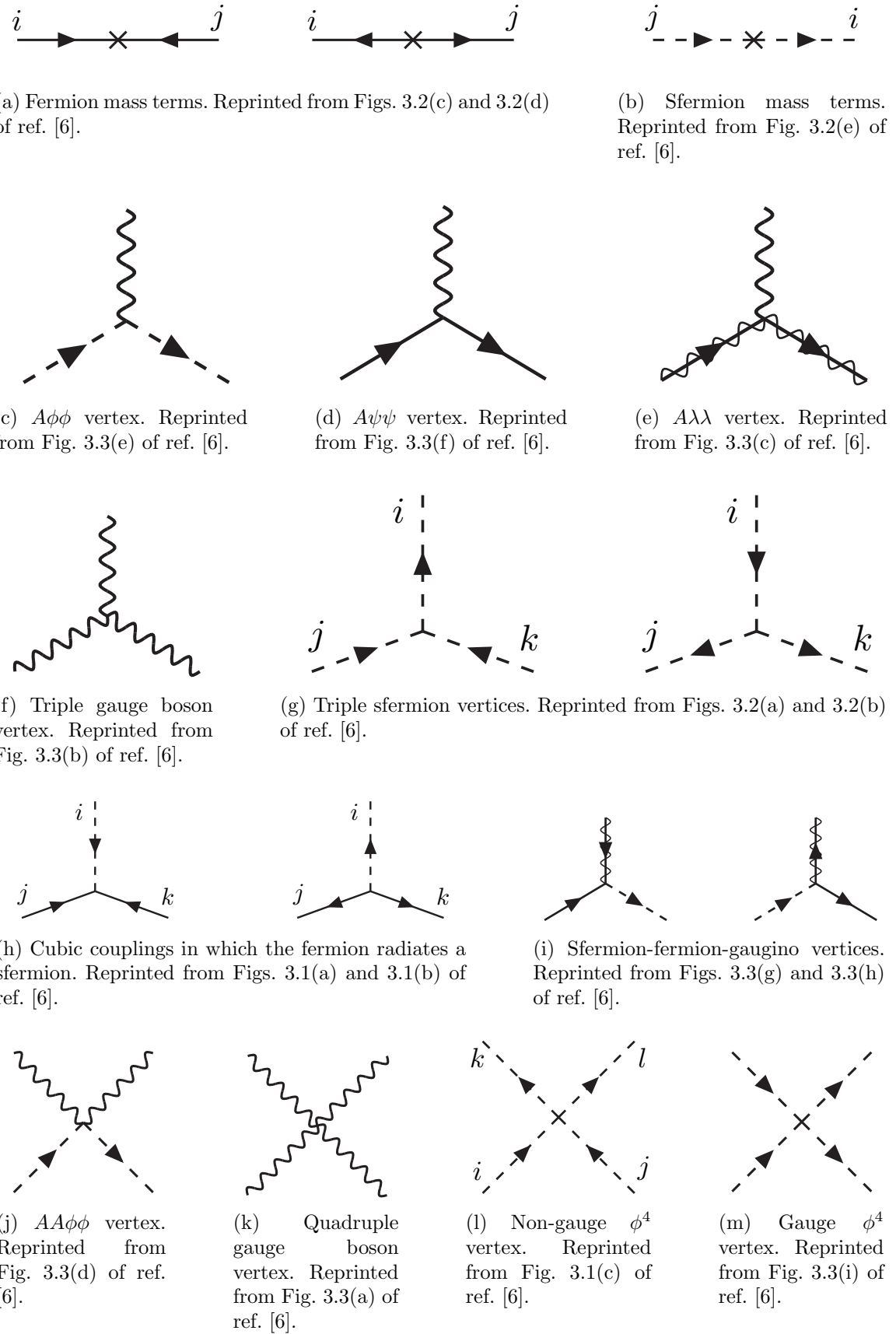


Figure 2.1: Interactions in the unbroken SUSY Lagrangian.

¹⁷⁸ Soft SUSY breaking terms give masses to the sfermions and gauginos and introduce
¹⁷⁹ a cubic sfermion vertex. The soft terms are given by

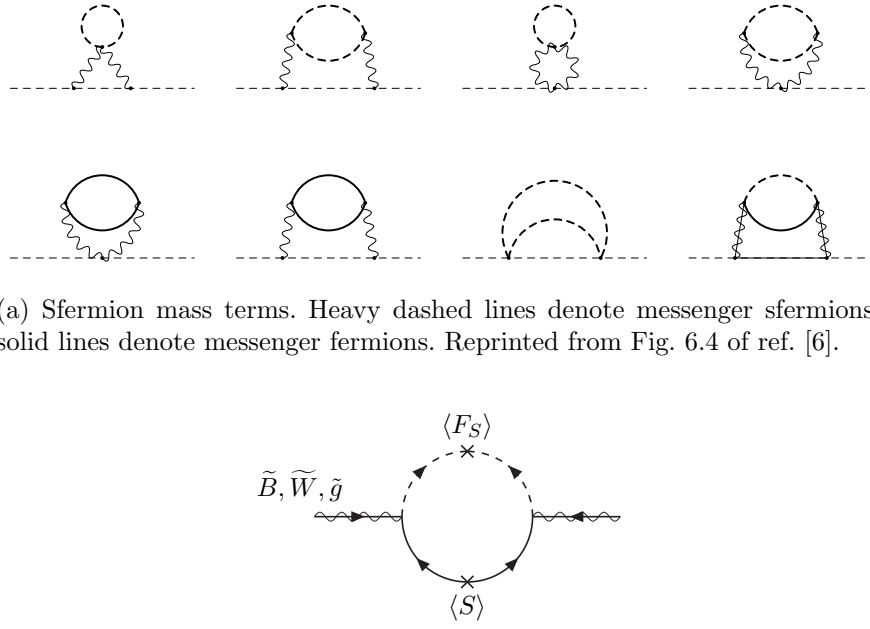
$$\begin{aligned}
 \mathcal{L}_{\text{soft}} = & -\frac{1}{2}(M_3 \tilde{g}^a \tilde{g}^a + M_2 \tilde{W}^a \tilde{W}^a + M_1 \tilde{B} \tilde{B} + \text{h.c.}) \\
 & - (a_u^{ij} \tilde{u}_{Ri}^* \tilde{Q}_j H_u - a_d^{ij} \tilde{d}_{Ri}^* \tilde{Q}_j H_d - a_e^{ij} \tilde{e}_{Ri}^* \tilde{L}_j H_d + \text{h.c.}) \\
 & - m_{\tilde{Q}_{ij}}^2 \tilde{Q}_i^\dagger \tilde{Q}_j - m_{\tilde{L}_{ij}}^2 \tilde{L}_i^\dagger \tilde{L}_j \\
 & - m_{\tilde{u}_{ij}}^2 \tilde{u}_{Ri} \tilde{u}_{Rj}^* - m_{\tilde{d}_{ij}}^2 \tilde{d}_{Ri} \tilde{d}_{Rj}^* - m_{\tilde{e}_{ij}}^2 \tilde{e}_{Ri} \tilde{e}_{Rj}^* \\
 & - m_{H_u}^2 H_u^* H_u - m_{H_d}^2 H_d^* H_d - (b H_u H_d + \text{h.c.})
 \end{aligned} \tag{2.14}$$

¹⁸⁰ where a runs from 1-8 for \tilde{g}^a and from 1-3 for \tilde{W}^a , and i, j run over the three families.
¹⁸¹ The color indices are not shown. The first line of Eq. 2.14 contains the gaugino mass
¹⁸² terms. The second line contains cubic scalar couplings that contribute to mixing
¹⁸³ between the left- and right-handed third generation sfermions (it is assumed in the
¹⁸⁴ supersymmetric Standard Model that the a_u^{ij} , a_d^{ij} , and a_e^{ij} are negligible unless $i =$
¹⁸⁵ $j = 3$). The third and fourth lines of Eq. 2.14 contain squark and slepton mass terms,
¹⁸⁶ and finally the last line contains the Higgs mass terms.

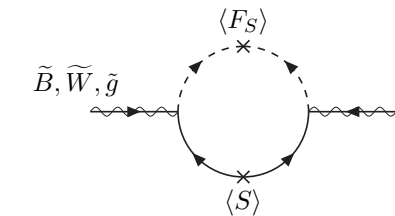
¹⁸⁷ Many viable models of achieving soft SUSY breaking have been studied over the
¹⁸⁸ last 30 years. For an overview, see Sec. 6 of ref. [6]. However, this thesis will only cover
¹⁸⁹ *gauge-mediated SUSY breaking* (GMSB), because the two-photon search performed
¹⁹⁰ is far more sensitive to this model than to other models of SUSY breaking.

¹⁹¹ 2.4 Gauge-Mediated SUSY Breaking

¹⁹² In gauge-mediated models [7], “hidden” fields spontaneously break the supersymme-
¹⁹³ try of very heavy chiral *messenger* supermultiplets. There are a number of compet-
¹⁹⁴ ing models (see ref. [7]) that explain the precise mechanism of spontaneous SUSY



(a) Sfermion mass terms. Heavy dashed lines denote messenger sfermions; solid lines denote messenger fermions. Reprinted from Fig. 6.4 of ref. [6].



(b) Gaugino mass term. The $\langle S \rangle$ part of the loop is a messenger fermion contribution; the $\langle F_S \rangle$ part is a messenger sfermion contribution. Reprinted from Fig. 6.3 of ref. [6].

Figure 2.2: Contributions to sfermion and gaugino masses from loop interactions with messenger particles in the GMSB framework.

195 breaking, but fortunately the details of those models mostly decouple from the phe-
 196 nomenology of GMSB. The messengers then communicate the SUSY breaking to the
 197 sparticles via loop diagrams of gauge interaction strength (i.e. via vertices like those
 198 shown in Figs. 2.1(c), 2.1(d), 2.1(i), 2.1(j), and 2.1(m), which are proportional to
 199 the SM gauge coupling constants). Feynman diagrams corresponding to gaugino and
 200 sfermion mass terms are shown in Figure 2.2.

201 Historically, GMSB and gravity-mediated SUSY breaking, or mSUGRA [8], have
 202 been the two most thoroughly experimentally studied scenarios of SUSY breaking.
 203 One advantage of GMSB over mSUGRA is that it naturally suppresses flavor vio-
 204 lation, a generic prediction of supersymmetry. Flavor violation is introduced in the
 205 scalar³ couplings and sfermion mass terms of $\mathcal{L}_{\text{soft}}$ (second, third, and fourth lines of

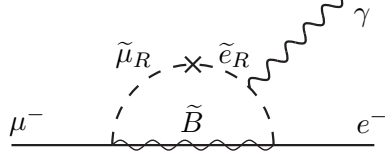


Figure 2.3: Possible contribution to $\mu \rightarrow e\gamma$ from $m_{\tilde{e}ij}$ soft term. Reprinted from Fig. 5.6(a) of ref. [6].

Eq. 2.14). Since a_u^{ij} , a_d^{ij} , a_e^{ij} , $m_{\tilde{Q}ij}$, $m_{\tilde{L}ij}$, $m_{\tilde{u}ij}$, $m_{\tilde{d}ij}$, and $m_{\tilde{e}ij}$ are matrices in family space, any nonzero off-diagonal elements will lead to mixing between sfermions of different families. This can lead, for example, to contributions to the diagram $\mu \rightarrow e\gamma$ (Figure 2.3) exceeding the experimental bounds. To avoid this disaster, *universality* conditions are assumed:

$$\mathbf{m}_{\tilde{\mathbf{Q}}}^2 = m_{\tilde{Q}}^2 \mathbf{1}, \mathbf{m}_{\tilde{\mathbf{L}}}^2 = m_{\tilde{L}}^2 \mathbf{1}, \mathbf{m}_{\tilde{\mathbf{u}}}^2 = m_{\tilde{u}}^2 \mathbf{1}, \mathbf{m}_{\tilde{\mathbf{d}}}^2 = m_{\tilde{d}}^2 \mathbf{1}, \mathbf{m}_{\tilde{\mathbf{e}}}^2 = m_{\tilde{e}}^2 \mathbf{1} \quad (2.15)$$

i.e. all sfermion mass matrices arising from the soft terms are assumed to be proportional to the unit matrix $\mathbf{1}$, such that there can be no flavor mixing from these terms and contributions to flavor-changing processes are drastically reduced.² In mSUGRA models, universality is assumed from the beginning, while in GMSB it is a natural consequence of the fact that the sparticle-messenger vertices are flavor-blind.

In minimal GMSB (mGMSB), there are four messenger supermultiplets q, \bar{q}, l, \bar{l} providing the messenger (s)quarks and (s)leptons. There is one breaking scale Λ . The gaugino masses computed from diagrams like Fig. 2.2(b) are given by

$$M_a = \frac{\alpha_a}{4\pi} \Lambda \quad (2.16)$$

²Universality also includes some assumptions about the form of a_{uij} , a_{dij} , and a_{eij} and the stipulation that the soft terms not introduce any CP-violating phases.

²¹⁹ where a runs from 1-3 and the α_a are the SM gauge coupling constants. The sfermion
²²⁰ masses computed from diagrams like Fig. 2.2(a) are given by

$$m_{\phi_i}^2 = 2\Lambda^2 \sum_{a=1}^3 \left(\frac{\alpha_a}{4\pi}\right)^2 C_a(i) \quad (2.17)$$

²²¹ where $C_a(i)$ are group theory factors that are identical for all particles residing in
²²² the same type of supermultiplet (e.g. for all left-handed (s)quarks or left-handed
²²³ (s)leptons). As explained in the previous paragraph, the gaugino and sfermion masses
²²⁴ do not depend on fermion family.

²²⁵ In recent years, much theoretical progress has been made in unifying models of
²²⁶ gauge mediation and developing less restrictive models than mGMSB. *General gauge*
²²⁷ *mediation* (GGM) [9] retains the essential features of mGMSB, such as flavor de-
²²⁸ generacy and communication of SUSY breaking via messengers, but does not make
²²⁹ assumptions about the specific messenger sector or SUSY breaking scale. Many dif-
²³⁰ ferent collider final states can be interpreted in terms of GGM, and conversely, GGM
²³¹ implies a wealth of signatures, only a small fraction of which have been searched for
²³² at colliders [10, 11, 12]. The following section discusses the aspects of GGM collider
²³³ phenomenology relevant to this thesis.

²³⁴ 2.5 Phenomenology of General Gauge Mediation

²³⁵ The main distinguishing feature of all GMSB phenomenology is that the gravitino \tilde{G} is
²³⁶ very light (eV-keV). In general, the gravitino mass is proportional to $\langle F \rangle / M_P$, where
²³⁷ $\langle F \rangle$ is the vacuum expectation value (VEV) of a field F that spontaneously breaks
²³⁸ SUSY in the vacuum state and M_P is the Planck mass. In GGM models, $\langle F \rangle \sim 10^8$
²³⁹ GeV, leading to a very light gravitino. In contrast, mSUGRA predicts $\langle F \rangle \sim 10^{20}$
²⁴⁰ GeV. The fact that the gravitino is so much lighter than any other particles in the

²⁴¹ supersymmetric Standard Model, and that it interacts only gravitationally (and thus
²⁴² extremely feebly), leads to two important phenomenological consequences:

- ²⁴³ 1. All sparticle decay chains end with the production of a gravitino.
- ²⁴⁴ 2. The gravitino escapes 4π , hermetic collider detectors without interacting, leav-
²⁴⁵ ing a signature of “missing” momentum transverse to the beam direction.

²⁴⁶ Even if the gravitino were lighter than any other sparticle, but heavier than an
²⁴⁷ ordinary SM particle, it still could not decay to the SM particle due to *R-parity*. R-
²⁴⁸ parity is a conserved quantity of the supersymmetric Standard Model that enforces
²⁴⁹ baryon and lepton number conservation, which would otherwise be generically allowed
²⁵⁰ at levels in conflict with experiment (e.g. the non-observation of baryon- and lepton-
²⁵¹ number-violating proton decay). All sparticles have R-parity -1, while all ordinary SM
²⁵² particles have R-parity +1, and R-parity conservation dictates that at any vertex, the
²⁵³ product of the R-parities of each leg must be +1. This leads to two more important
²⁵⁴ consequences:

- ²⁵⁵ 1. Since conservation of energy only allows it to decay to ordinary SM particles,
²⁵⁶ but R-parity prevents a sparticle-particle-particle vertex, the *lightest supersym-
²⁵⁷ metric particle* (LSP) must be absolutely stable. All sparticle decays proceed
²⁵⁸ through the *next-to-lightest supersymmetric particle* (NLSP), which in turn de-
²⁵⁹ cays to the LSP. The fact that it is stable and only gravitationally interacting
²⁶⁰ makes the gravitino a candidate dark matter particle (see Sec. 2.6).
- ²⁶¹ 2. In colliders, sparticles are produced in pairs (particle + particle \rightarrow sparticle +
²⁶² sparticle).

²⁶³ In GMSB, then, the gravitino is the LSP. If the NLSP is a gaugino,³ then the
²⁶⁴ possible decays depend on mixing among the gauginos. Due to the effects of EWSB,

³In principle, the NLSP could be anything, but in most popular GGM models, it is either a gaugino or a stau. The stau NLSP search is not the subject of this thesis, so it will not be considered in this section.

the four neutral gauginos $\tilde{H}_u^0, \tilde{H}_d^0, \tilde{B}, \tilde{W}^0$ mix into four *neutralino* mass eigenstates $\tilde{\chi}_1^0, \tilde{\chi}_2^0, \tilde{\chi}_3^0, \tilde{\chi}_4^0$, and the four charged gauginos $\tilde{H}_u^+, \tilde{H}_d^-, \tilde{W}^+, \tilde{W}^-$ mix into two *chargino* mass eigenstates $\tilde{\chi}_1^\pm, \tilde{\chi}_2^\pm$ (two mass eigenstates each with two possible charges = four particles). In the limit that EWSB effects are small, the neutralino and chargino masses can be written as the gauge eigenstate masses plus a small perturbation:

$$m_{\tilde{\chi}_1^0} = M_1 - \frac{m_Z^2 \sin^2 \theta_W (M_1 + \mu \sin 2\beta)}{\mu^2 - M_1^2} + \dots \quad (2.18)$$

$$m_{\tilde{\chi}_2^0} = M_2 - \frac{m_W^2 (M_2 + \mu \sin 2\beta)}{\mu^2 - M_2^2} + \dots \quad (2.19)$$

$$m_{\tilde{\chi}_3^0} = |\mu| + \frac{m_Z^2 (\text{sgn}(\mu) - \sin 2\beta)(\mu + M_1 \cos^2 \theta_W + M_2 \sin^2 \theta_W)}{2(\mu + M_1)(\mu + M_2)} + \dots \quad (2.20)$$

$$m_{\tilde{\chi}_4^0} = |\mu| + \frac{m_Z^2 (\text{sgn}(\mu) + \sin 2\beta)(\mu - M_1 \cos^2 \theta_W - M_2 \sin^2 \theta_W)}{2(\mu - M_1)(\mu - M_2)} + \dots \quad (2.21)$$

$$m_{\tilde{\chi}_1^\pm} = M_2 - \frac{m_W^2 (M_2 + \mu \sin 2\beta)}{\mu^2 - M_2^2} + \dots \quad (2.22)$$

$$m_{\tilde{\chi}_2^\pm} = |\mu| + \frac{m_W^2 \text{sgn}(\mu)(\mu + M_2 \sin 2\beta)}{\mu^2 - M_2^2} + \dots \quad (2.23)$$

where $\tan \beta = \langle H_u^0 \rangle / \langle H_d^0 \rangle$.

The two scenarios studied in ref. [12] are the following:

• **Bino NLSP:** $M_1 \sim$ few hundred GeV, $M_2, |\mu| \gg M_1$. All but the lightest neutralino are effectively inaccessible at the LHC due to their large masses. The NLSP can always decay to $\gamma + \tilde{G}$, and if it is heavy enough, to $Z + \tilde{G}$ or $H + \tilde{G}$.

• **Wino NLSP:** $M_2 \sim$ few hundred GeV, $M_1, |\mu| \gg M_2$. The lightest neutralino and the lightest chargino are nearly degenerate in mass, and are the only two particles to play a role at the LHC. The decays described in the previous bullet point can happen, as well as chargino decays to $W + \tilde{G}$.

The subject of this thesis is the classic bino NLSP decay $\gamma + \tilde{G}$.

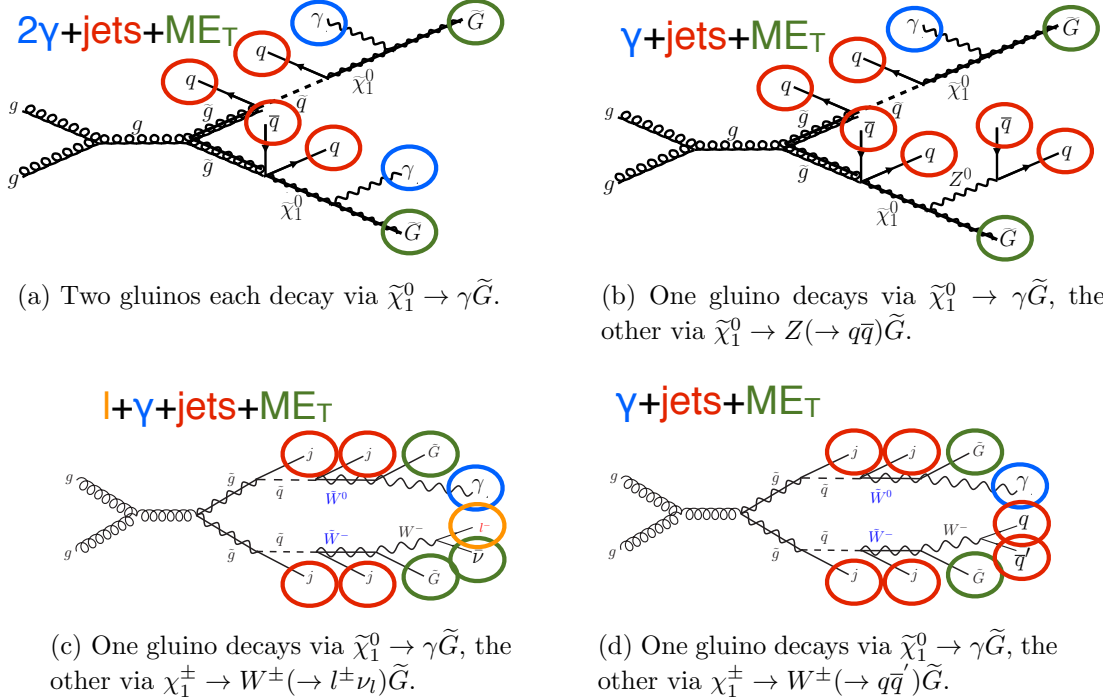


Figure 2.4: Typical LHC signatures of the bino and wino NLSP scenarios.

280 Since strong production of SUSY particles dominates over electroweak production
281 at the LHC due to the enhanced gg parton luminosity over the $q\bar{q}$ parton luminosity,
282 early LHC searches are particularly sensitive to light squarks and gluinos. General
283 gauge mediation makes no a priori restrictions on the mass splitting between the
284 strongly interacting sparticles and the weakly interacting sparticles, so models with
285 light squarks and gluinos are viable. In fact, such models could not be probed as
286 well at the Tevatron⁴ as they are at the LHC due to the aforementioned parton
287 luminosities.

288 Typical LHC signatures of the bino and wino NLSP scenarios are shown in Fig-
289 ure 2.4.

⁴Located on the Fermilab site in Batavia, Illinois, the Tevatron was a proton-antiproton collider operating at 1.96 TeV center-of-mass energy. The Tevatron ran from 1987 to 2011 [13].

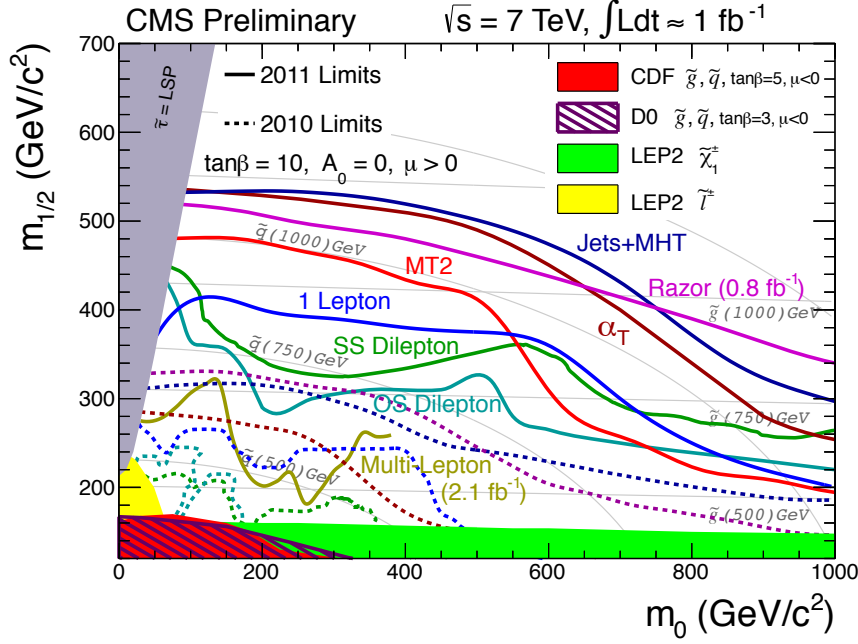


Figure 2.5: CMS limits on mSUGRA with $\tan \beta = 10$. The limits set by individual searches are shown as separate colored lines. Solid lines refer to 2011 searches (i.e. using an integrated luminosity of $\sim 1 \text{ fb}^{-1}$), while dashed lines refer to 2010 searches ($\sim 36 \text{ pb}^{-1}$). Reprinted from ref. [16].

290 2.6 Experimental Status of SUSY

291 Collider searches for evidence of supersymmetry began in earnest in the 1980s [14]
 292 and continue to this day. Most recently, the LHC and Tevatron experiments have set
 293 the strictest limits on a variety of SUSY breaking scenarios, including GMSB and
 294 mSUGRA.

295 Figure 2.5 shows the current limits set by the CMS experiment on the mSUGRA
 296 model (with $\tan \beta = 10$) in the m_0 - $m_{1/2}$ plane. (Note that although the plot is trun-
 297 cated at $m_0 = 1000 \text{ GeV}/c^2$, some searches are sensitive out to $m_0 \sim 2000 \text{ GeV}/c^2$.)
 298 Although the LHC has pushed m_0 above $\sim 1 \text{ TeV}/c^2$ for $m_{1/2}$ up to $\sim 400 \text{ GeV}/c^2$,
 299 casting some doubt onto the theory's prospects for solving the hierarchy problem,
 300 there is still a sizable chunk of mSUGRA parameter space that is not ruled out by
 301 collider experiments. Furthermore, parts of the CMS unexplored regions overlap with
 302 areas allowed by astrophysics experiments [15].

303 Figure 2.6 shows the most up-to-date limit (using 1 fb^{-1} of integrated luminosity
 304 collected by the ATLAS experiment [17] at the LHC) on the Snowmass Points and
 305 Slopes (SPS) model of mGMSB, dubbed SPS8 [18]. The best limits on a variety
 306 of GGM models are shown in Figure 2.7 [19]. In these models, no assumptions are
 307 made about the specific parameters common to many gauge mediation models (e.g.
 308 the number of messengers or the relationship between the messenger mass and the
 309 SUSY breaking scale). Instead, it is only assumed that the lightest neutralino is light
 310 enough to be produced on-shell at the LHC (by setting M_1 and M_2 appropriately, see
 311 Sec. 2.5) and that it decays to a gravitino, that the gravitino is extremely relativistic
 312 (mass of order eV-keV), and that the gravitino is stable. The one-dimensional scan
 313 over SUSY breaking scales in the SPS8 model (in which the full sparticle spectrum is
 314 specified by the model parameters) is replaced by a two-dimensional scan over gluino
 315 and lightest neutralino mass in the GGM models (in which all sparticles except the
 316 gluino, first- and second-generation squarks, and neutralinos are forced to be at ~ 1.5
 317 TeV/c^2 , effectively decoupling them from the dynamics that can be probed with 1
 318 fb^{-1} at a $7 \text{ TeV}/c$ pp collider).

319 In general, the lifetime of the lightest neutralino in GMSB models can take on any
 320 value between hundreds of nanometers to a few kilometers depending on the mass
 321 of the lightest neutralino and the SUSY breaking scale [6]. The search published in
 322 ref. [10] (from which Figs. 2.6 and ?? are culled) considers only *prompt* neutralino
 323 variants, i.e. with neutralino lifetime short enough that the distance traveled by the
 324 neutralino before decay cannot be resolved by the detector. The most recent limits
 325 on non-prompt SPS8-style neutralino models were set by the Collider Detector at
 326 Fermilab (CDF) collaboration with 570 pb^{-1} , and are shown in Figure 2.8 [11].

327 Finally, if the gravitino is to make up some or all of the dark matter, constraints
 328 on the form of gauge mediation must come from cosmological considerations and
 329 astronomical observations. The gravitino in gauge mediation models is usually very

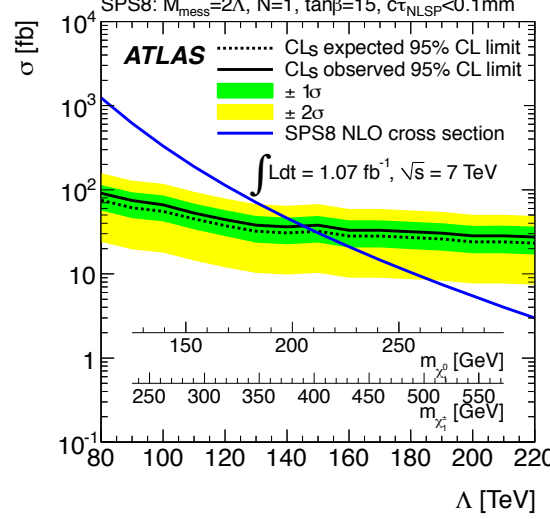


Figure 2.6: ATLAS cross section upper limit on the SPS8 [18] model of mGMSB as a function of SUSY breaking scale Λ , lightest neutralino mass $m_{\tilde{\chi}_1^0}$, or lightest chargino mass $m_{\tilde{\chi}_1^\pm}$. Values of Λ , $m_{\tilde{\chi}_1^0}$, or $m_{\tilde{\chi}_1^\pm}$ below the intersection point between the blue (predicted SPS8 cross section) and black (observed cross section upper limit) curves are excluded. The model parameters listed above the plot are defined in Secs. 2.4 and 2.5, except for τ_{NLSP} , which is the neutralino lifetime. Reprinted from ref. [10].

330 light ($\mathcal{O}(\text{eV-MeV})$) because it is proportional to the SUSY breaking scale divided by
 331 the Planck mass, and in GMSB the breaking scale is typically only of order a few
 332 hundred TeV ([6] and Sec. 2.5). A light, highly relativistic dark matter particle might
 333 have been produced, for instance, in the early, radiation-dominated period of the
 334 universe [20]. This *warm dark matter* (WDM) may be responsible for all of the dark
 335 matter needed to account for galactic structure, or it may share the duties with *cold*
 336 *dark matter* (CDM, weakly interacting particles with masses in the GeV range). In
 337 any viable model, the predicted relic density of the dark matter species must match
 338 the observed value of $\Omega h^2 \sim 0.1$ [21]. For many GMSB models, this measurement
 339 constrains the gravitino mass to the keV range [22]. This constraint, however, does
 340 not translate into a very strong bound on the lifetime of the lightest neutralino. Using
 341 the following equation (taken from [22]):

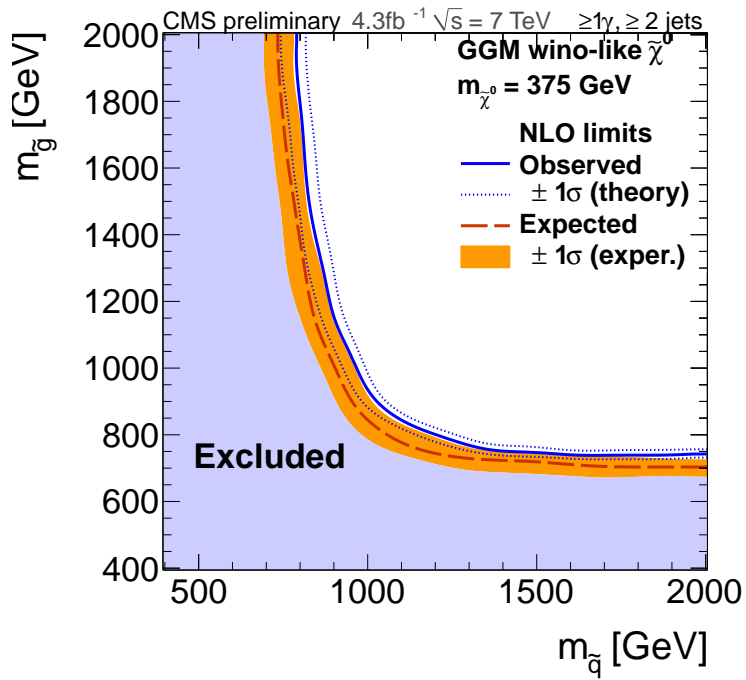
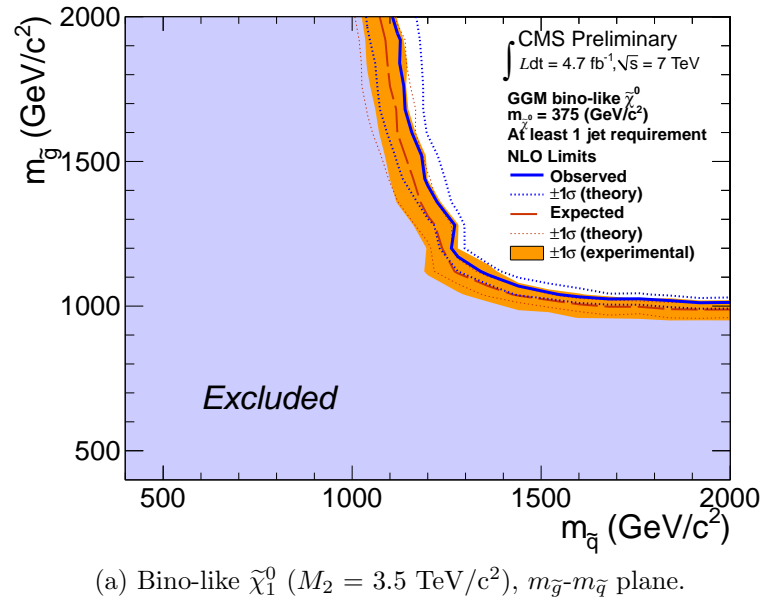


Figure 2.7: CMS exclusion contours for GGM models using 5 fb^{-1} of LHC data. Reprinted from ref. [12].

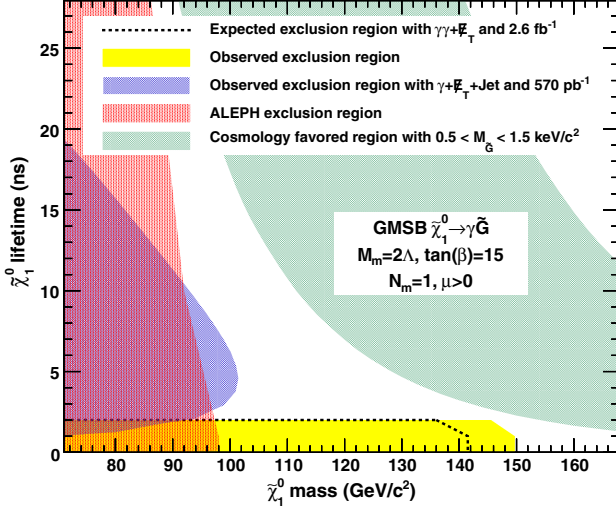


Figure 2.8: CDF exclusion contour in the $\tau_{\tilde{\chi}_1^0}$ - $m_{\tilde{\chi}_1^0}$ plane, where $\tau_{\tilde{\chi}_1^0}$ is the lifetime of the neutralino. Reprinted from ref. [11].

$$\tau_{\tilde{\chi}_1^0} \sim 130 \left(\frac{100 \text{ GeV}}{m_{\tilde{\chi}_1^0}} \right)^5 \left(\frac{\sqrt{\langle F \rangle}}{100 \text{ TeV}} \right)^4 \mu\text{m} \quad (2.24)$$

and applying the gravitino mass constraint $\sqrt{\langle F \rangle} \lesssim 3000 \text{ TeV}$ (cf. the first paragraph of Sec. 2.5 with $m_{\tilde{G}} \sim \text{keV}$) and $m_{\tilde{\chi}_1^0} = 100 \text{ GeV}$, the upper bound on the neutralino lifetime is 100 meters. For $\sqrt{\langle F \rangle} \sim 100 \text{ TeV}$, the neutralino lifetime is detectable on collider time scales.

Recently, a lower bound on the WDM particle mass in either pure warm or mixed warm and cold dark matter scenarios was set using observations of the Lyman- α forest. For pure WDM, $m_{\text{WDM}} > 8 \text{ keV}$, while for some mixed WDM-CDM scenarios, $m_{\text{WDM}} > 1.1\text{-}1.5 \text{ keV}$ [20, 23]. These bounds and others have motivated the development of more complicated gauge mediation models [23]. However, rather than focus on a specific GMSB model, of which there are many, the search detailed here is interpreted in a minimally model dependent way. With this approach, the results can be applied to many competing models. The remainder of this thesis is devoted to the experimental details of the search, analysis strategy, and presentation of the results. The work described in this thesis forms the basis for the CMS public result ‘‘Search

³⁵⁶ for Supersymmetry in Events with Photons and Missing Energy” [19], published in
³⁵⁷ April 2012.

358 **Chapter 3**

359 **Event Selection**

360 In keeping with the phenomenology described in Sec. 2.5, the candidate GGM events
361 selected in this search consist of two high- E_T photons and a significant momentum
362 imbalance transverse to the beam, indicating the production of an escaping gravitino.
363 This momentum imbalance is usually referred to as *missing transverse energy* and is
364 denoted by the symbol \cancel{E}_T .

365 However, in order to use real CMS data (as opposed to simulation) to derive pre-
366 dictions for the backgrounds to the search, *control samples* distinct from the *candidate*
367 two-photon sample must be collected. These samples consist of different numerical
368 combinations of photons, electrons, and jets, and are explained in more detail in
369 Chapter 4. Since this search is performed in the high- \cancel{E}_T tail of the \cancel{E}_T distribution,
370 where adequate detector simulation is very difficult, it is advantageous to use *data-
371 driven* background estimates, which capture the true detector response, over numbers
372 derived from simulation.

373 In the following sections, the reconstruction of photons, electrons, jets, and \cancel{E}_T
374 is explained. Sec. 3.1 begins with an explanation of the high level reconstruction.
375 It is followed by Sec. 3.2, which describes the triggers used to collect the candidate
376 and control samples. Sec. 3.3 describes event cleaning cuts that are applied to the

³⁷⁷ candidate and control samples. Finally, the chapter concludes with a measurement of
³⁷⁸ the photon identification efficiency in Sec. 3.4.

³⁷⁹ 3.1 Object Reconstruction

³⁸⁰ This section describes the *offline* object reconstruction, i.e. the reconstruction of par-
³⁸¹ ticle objects from events that have already been triggered and written to permanent
³⁸² storage, as opposed to the building of trigger objects explained in Secs. ?? and 3.2.

³⁸³ 3.1.1 Photons

³⁸⁴ Uncalibrated EB/EE Hits

³⁸⁵ Photon reconstruction begins with the ADC count value for each of the 10 recorded
³⁸⁶ time samples per ECAL crystal per trigger. To construct an *uncalibrated hit*, the
³⁸⁷ gain (1, 6, or 12; see Sec. ??) of each sample is determined and the ADC count
³⁸⁸ value scaled appropriately. The pedestal is estimated from the average of the first
³⁸⁹ three samples, which, for a properly timed in hit, should contain no signal. This
³⁹⁰ pedestal value is subtracted from the rest of the samples. Finally, the amplitude of the
³⁹¹ pulse is reconstructed using a predetermined weight for each sample [24]. The weights
³⁹² correspond to the pulse shape expected from the MGPA and shaping circuit response.
³⁹³ The time of the hit is also reconstructed using the ratios between neighboring time
³⁹⁴ samples [25]. A typical ECAL channel pulse shape is shown in Figure 3.1.

³⁹⁵ Calibrated EB/EE Hits

³⁹⁶ In the next phase of the photon reconstruction, calibrations are applied to the un-
³⁹⁷ calibrated hits to form *calibrated hits* with energy measured in GeV. Channels are
³⁹⁸ excluded from seeding calibrated hits if

- ³⁹⁹ • they are excessively noisy,

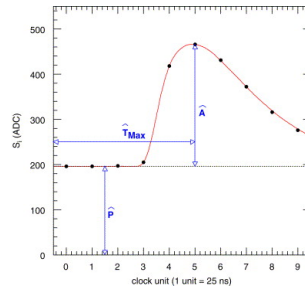


Figure 3.1: Typical ECAL channel pulse shape. \hat{P} is the pedestal value, \hat{A} is the pulse amplitude, and \hat{T}_{\max} is the hit time. The red line is the assumed pulse shape from which the weights are derived. Reprinted from ref. [24].

- 400 • they are stuck in fixed gain (i.e. the MGPA gain does not change properly to
401 avoid saturation),
- 402 • they are totally dead,
- 403 • they have one or more neighboring dead channels, or
- 404 • they do not have good trigger primitives (i.e. trigger primitive is missing, satu-
405 rated, or *spike-like*).

Added

406 *ECAL spikes* are hits in which low energy protons and heavy ions from jets ionize this
407 in the sensitive volume of the EB APD, causing the APD to register a fake large- para-
408 amplitude hit. Because they are not the result of a real electromagnetic shower, spikes graph
409 tend to be isolated. They may also appear to arrive early or late with respect to the and the
410 nominal bunch crossing. Most spikes are reconstructed with a hit time ~ 10 ns earlier next
411 than real EM hits because unlike real hits, whose pulse shapes include the time about
412 constant associated with crystal scintillation, the reconstructed spikes only involve spikes
413 the rise time of the electronics. There also is a long tail of late arriving spikes due to
414 slow neutrons from jets [26].

415 Because of their particular timing and topological characteristics, cuts have been
416 developed to effectively identify and reject spike-like hits. This analysis utilizes both
417 the “Swiss cross” cut $1 - E_4/E_1 > 0.95$, where E_1 is the energy of the spike candidate

418 crystal and E_4 is the sum of the energies in the four crystals whose edges are parallel to
 419 the four edges of the spike candidate crystal, and a timing cut $t \geq 3$ ns, to flag spikes.
 420 More information about these cuts can be found in ref. [26]. A simpler algorithm
 421 using the fine grain veto bit of the L1 TPG is used to reject spikes at the trigger level
 422 [insert citation].

423 In addition to the trigger primitives, no uncalibrated hits that are spike-like are eli-
 424 gible for calibration. The calibrations applied are crystal transparency loss corrections
 425 measured continuously by the laser/LED system, energy intercalibrations (relative en-
 426 ergy calibration between crystals), absolute scale calibrations between ADC counts
 427 and GeV,¹ and time intercalibrations (relative time calibration between crystals).

428 The ECAL crystals were pre-calibrated before installation in CMS using labora-
 429 tory light yield and photodetector gain measurements [28]. In addition, some EB and
 430 EE crystals were intercalibrated using test beams [29], and all EB crystals were inter-
 431 calibrated with cosmic ray muons [30]. EE precalibrations were validated with LHC
 432 *splash events* in 2009 [30, 31], in which the beam was dumped onto a collimator ap-
 433 proximately 150 meters upstream of CMS, causing a spray of muons to enter CMS at
 434 one endcap and exit at the other. Splash events were also used to derive time intercal-
 435 ibration constants. Before colliding beam operations commenced, the intercalibration
 436 precision was estimated to be 0.5%-2.2% in EB and 1%-5% in EE [32].

437 Three calibration methods were employed once colliding beam operations began:

- 438 • ϕ symmetry relative calibration between crystals, exploiting the azimuthal sym-
 metry of CMS
- 440 • π^0 and η relative calibration between crystals, using the diphoton decays of
 these particles

¹The ADC-GeV scale factors (one for EB and one for EE) are defined such that the sum of fully calibrated and scaled hits in a particular 5×5 cluster of crystals (plus the associated energy deposited in ES) is 50 GeV for a 50 GeV incident unconverted photon [27].

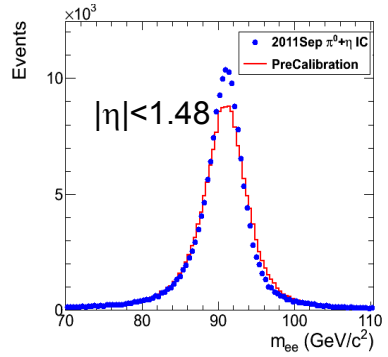


Figure 3.2: Z peak reconstructed using pre-LHC calibration constants (red) or September 2011 π^0/η -derived intercalibration constants (blue). Reprinted from ref. [33].

442 • E/p absolute calibration, comparing the momentum measured in the tracker p
 443 to the energy measured in the ECAL E of a sample of electrons from Z decay

444 By September 2011, the intercalibration precision in EB was measured to be be-
 445 tween 0.3% and 1.1% using the π^0/η method [33]. Figure 3.2 shows the improvement
 446 in Z reconstruction from pre-LHC calibration constants to the latest π^0/η -derived
 447 constants.

448 **Calibrated ES Hits**

Added

449 ES calibrated hits are formed from the three samples read out per sensor. Just as in the paren-
 450 case of EB/EE crystals, ES uncalibrated hits gain-adjusted, pedestal-subtracted, and thetical
 451 reconstructed using weights. To make a calibrated ES hit, intercalibration constants, remark
 452 angle correction constants (for the non-uniformity of sensor angle with respect to the
 453 vertical across ES), and a MIP-GeV absolute scale factor are applied.

454 **Clustering**

455 After calibrated ECAL hits are formed, they must be clustered into shapes that
 456 represent the energy deposit from a single particle. *Basic clusters* are formed around
 457 seed hits, defined as a hit that

- 458 • has calibrated $E_T > 1(0.18)$ GeV in EB(EE),
- 459 • does not originate from a dead channel or one with faulty hardware,
- 460 • is not poorly calibrated,
- 461 • was reconstructed with the standard algorithm (i.e. not a special recovery algo-
- 462 rithm for channels with subpar data integrity),
- 463 • is not saturated,
- 464 • is not spike-like, and
- 465 • is in time (EB).

466 EB basic clusters are formed around the seeds via the *hybrid* algorithm, while EE basic
 467 clusters are formed with the `multi5x5` algorithm [34]. In addition to non-radiating
 468 electrons and unconverted photons, both algorithms are designed to also recover all of
 469 the energy associated with electron bremsstrahlung deposits and photon conversions.
 470 The geometry of the CMS magnetic field means that bremsstrahlung and conversions
 471 will tend to spread the shower out in ϕ , not η . Both algorithms work by forming
 472 basic clusters around seeds, then combining the basic clusters into *superclusters* (SC)
 473 by searching in a window extended in the ϕ direction for all basic clusters consistent
 474 with bremsstrahlung radiation from the primary electron, or with a photon conversion.
 475 Figure 3.3 illustrates the hybrid algorithm in EB. In EE, the energy deposited in ES
 476 must also be added into the total clustered energy sum.

477 Figure 3.4 shows the effect of superclustering on $Z \rightarrow ee$ reconstruction.

478 **Supercluster Corrections**

479 The total clustered ECAL energy is defined as

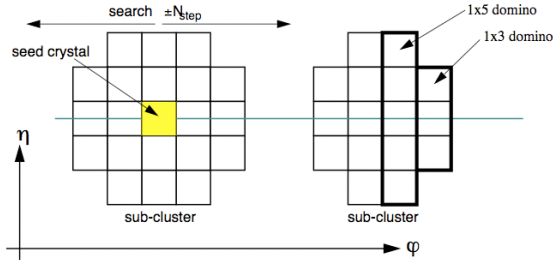


Figure 3.3: Hybrid algorithm in EB. The shower extent is essentially constant in η , but spreads out in ϕ as the two sub-clusters (or basic clusters) are grouped into the same supercluster. Reprinted from ref. [34].

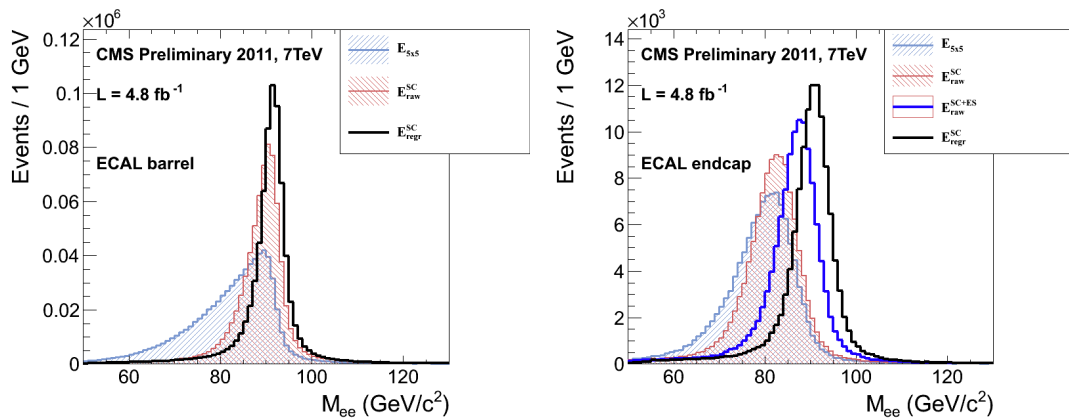


Figure 3.4: Z peak reconstructed in the dielectron channel for different kinds of clustering. The left plot is for EB and the right plot for EE. The constituent hits were calibrated with the best available intercalibrations and laser calibrations as of December 2011. The light blue histogram shows the reconstruction using a 5×5 energy sum, the red histogram shows the reconstruction using the SC energy for crystals only (the dark blue histogram on the right-hand side adds in the energy from ES), and the black histogram shows the reconstruction after the SCs are corrected using a multivariate method [?]. Reprinted from Fig. 30 of ref. [?].

$$E = F \times \sum_{i=1}^{n_{\text{crystal}}} G \times c_i \times A_i \quad (3.1)$$

480 where G is the ADC-GeV or MIP-GeV scale factor, c_i are the intercalibration con-
 481 stants, A_i is the uncalibrated hit amplitude in ADC counts, and F is a SC correction
 482 factor. G and c_i were explained in Sec. 3.1.1. F is a product of three factors for hybrid
 483 SCs (two for multi5x5 SCs) [34]:

- 484 1. $C_{\text{EB}}(\eta)$, which compensates for lateral energy leakage due to the crystal off-
 485 pointing in EB. These corrections are taken from MC simulation [34] and were
 486 confirmed in test beams [29].
- 487 2. $f(\text{brem})$, which corrects for biases in the clustering algorithms for showers char-
 488 acterized by differing amounts of bremsstrahlung. These corrections are taken
 489 from MC simulation [34].
- 490 3. Residual correction $f(E_T, \eta)$, due to the variation in η of detector material
 491 traversed by a primary electron or photon, and to any residual E_T dependence
 492 of the reconstruction. These corrections are determined from MC and validated
 493 on $Z \rightarrow ee$ data samples [35].

Changed

494 As a benchmark of ECAL calibration performance, the extra energy smearing in
 495 MC needed to achieve data/MC agreement in the Z width was between $\sim 0.9\%$ (in
 496 the central part of EB for electrons with little bremsstrahlung) and $\sim 3.3\%$ (in the
 497 outer part of EE for heavily radiating electrons) [36].

498 From Supercluster to Photon

499 The CMS photon object is any SC with $E_T > 10$ GeV and $H/E < 0.5$, unless the SC
 500 $E_T > 100$ GeV, in which case the H/E requirement is dropped. H/E is defined as the

501 ratio of energy in the HCAL in a 0.15 cone around the SC centroid, directly behind
 502 the SC, to the SC energy. SCs with $R9 > 0.94(0.95)$ in EB(EE), where $R9$ is defined
 503 as the ratio of the energy in the central 3×3 cluster of crystals divided by the SC
 504 energy $E_{3 \times 3}/E_{\text{SC}}$, are the best calibrated and most accurate type of electromagnetic
 505 shower. Therefore, for these objects, the photon energy is defined as the energy sum
 506 of the fully calibrated hits in the central 5×5 cluster around the seed (with $C_{\text{EB}}(\eta)$
 507 applied for EB photons). For all other SCs, the photon energy is equal to the fully
 508 corrected SC energy (cf. Sec. 3.1.1).

Reorganized

509 In this search, candidate photons and *fake photons* (f , “fakes”) are further selected next 3
 510 according to the criteria listed in Table 3.1. Fakes are used in the determination of para-
 511 the QCD background, as explained in Chapter 4.

graphs;

Table 3.1: Selection criteria for photons and fakes. “Pixel seed,” I_{comb} , and $\sigma_{i\eta i\eta}$ are edited
defined in the text.

Variable	Cut (γ)	Cut (f)
SC $ \eta $	< 1.4442	< 1.4442
H/E	< 0.05	< 0.05
$R9$	< 1	< 1
Has pixel seed	No	No
$I_{\text{comb}}, \sigma_{i\eta i\eta}$	$< 6 \text{ GeV} \&\& < 0.011$	$(\geq 6 \&\& < 20 \text{ GeV}) \parallel \geq 0.011$

512 I_{comb} is defined as

Updated
effective
area

$$I_{\text{comb}} = I_{\text{ECAL}} - 0.093\rho + I_{\text{HCAL}} - 0.0281\rho + I_{\text{track}} \quad (3.2)$$

513 where I_{ECAL} , I_{HCAL} , and I_{track} are E_T sums in the annular regions defined in Figure 3.5
 514 and ρ is the average pileup energy density in the calorimeters (per unit $\eta \cdot \phi$) as
 515 measured with the Fastjet algorithm [37, 38]. Note that the ECAL and track isolation
 516 veto strips at constant η ensure that the isolation cuts are similarly efficient for
 517 converted photons, radiating electrons, and unconverted photons.

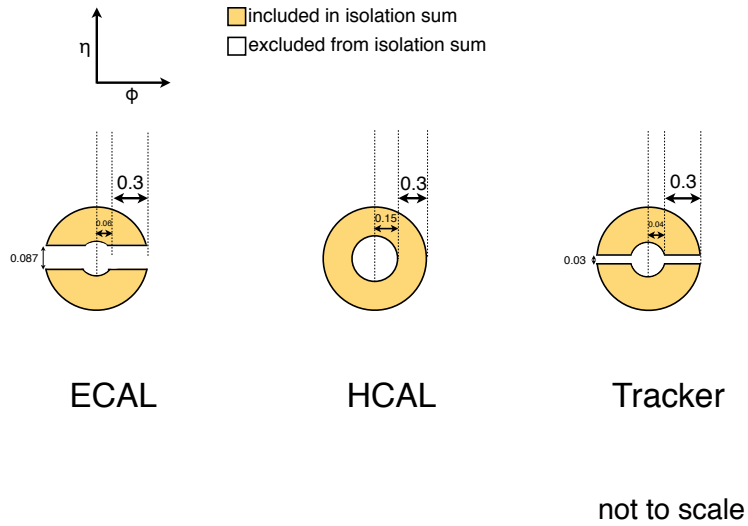


Figure 3.5: ECAL, HCAL, and track Isolation cones.

σ_{iηiη} is the log energy weighted extent of the shower in η and is defined as

$$\sigma_{i\eta i\eta} = \frac{\sum_{i=1}^{25} w_i (\eta_i - \bar{\eta})^2}{\sum_{i=1}^{25} w_i} \quad (3.3)$$

Added
σ_{iηiη}
definition

where the sums run over the 5×5 matrix of crystals surrounding the seed, $w_i = \max(0, 4.7 + \ln(E_i/E))$, E_i is the energy of the i^{th} crystal, E is the total energy in the 25 crystals, η_i is the offset in η of the i^{th} crystal from the seed, and $\bar{\eta}$ is the weighted average η of the 25 crystals (using the w_i as weights) [39].

Changed

Figure 3.6 shows the ρ distribution for a sample of two-photon events, with at least one 40 GeV and one 25 GeV photon, passing the selection requirements in Table 3.1 and the trigger requirements in Table 3.3. This sample represents the full 2011 dataset of 4.7 fb^{-1} . Since the average ρ is $\sim 7.5 \text{ GeV}$, and there is a long tail above this average value, it is necessary to subtract pileup energy from the ECAL and HCAL isolation cones to recover otherwise clean photons in events with large pileup. The ECAL and HCAL *effective areas* of 0.093 and 0.0281, respectively, are

average
 ρ ; up-
dated
fig. 3.6

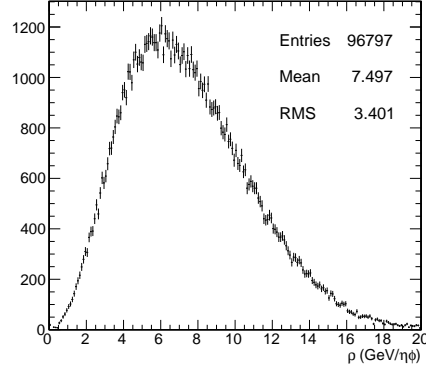


Figure 3.6: ρ distribution for a sample of two-photon events, with at least one 40 GeV and one 25 GeV photon, passing the selection requirements in Table 3.1 and the trigger requirements in Table 3.3. This sample covers the full 2011 dataset of 4.7 fb^{-1} .

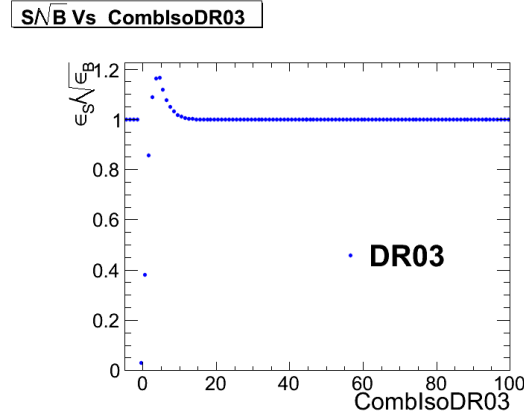


Figure 3.7: S/\sqrt{B} (S and B defined in the text) vs. combined isolation. Reprinted from Fig. 7 of ref. [40].

530 calculated by fitting the average ECAL or HCAL isolation energy vs. ρ in a sample
 531 of $Z \rightarrow ee$ events to a straight line. The slope of the line—which has the units of $\eta \cdot \phi$,
 532 or area—is the effective area.

New

533 The cut on combined isolation of 6 GeV (Table 3.1) is the result of an S/\sqrt{B}
 534 optimization procedure [40]. S is a sample of photons in simulated GGM events that
 535 are products of neutralino decay, while B is a sample of photons matched to generated
 536 hadronic jets in simulated QCD events. Figure 3.7 shows the value of S/\sqrt{B} vs.
 537 combined isolation, in particular the pronounced peak around 6 GeV.

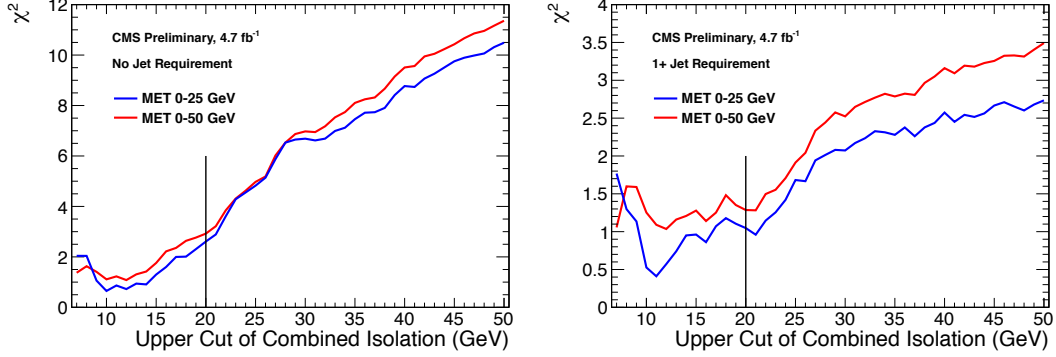


Figure 3.8: Neyman’s χ^2 between the ff and $\gamma\gamma$ \cancel{E}_T distributions, truncated at either 25 (red) or 50 (blue) GeV, vs. upper bound on fake combined isolation. The left plot includes all events; the right plot is for events with ≥ 1 jet defined as in Table 3.2, but with the ΔR cleaning criteria applied to the two primary EM objects and all additional electrons, photons, and fake photons. The full reweighting and normalization procedure is employed in the \cancel{E}_T calculation (see Sec. 4.1). Error bars include statistical, reweighting, and normalization error (see Sec. 4.3). Reprinted from Fig. 9 of ref. [40].

538 The upper bound on fake photon combined isolation guarantees that poorly iso-
 539 lated dijet events, with \cancel{E}_T resolution dissimilar to the candidate diphoton events,
 540 do not enter the ff sample. The exact value of 20 GeV (cf. Table 3.1) arises from
 541 a low- \cancel{E}_T $ff/\gamma\gamma$ χ^2 optimization procedure [40]. Figure 3.8 shows the value of the
 542 Neyman’s χ^2 between the ff and $\gamma\gamma$ \cancel{E}_T distributions, truncated at either 25 or 50
 543 GeV, vs. upper bound on fake combined isolation. As shown in the figure, 20 GeV
 544 very nearly minimizes the χ^2 , while also being large enough that a sufficient number
 545 of ff events may be collected.

546 Finally, a “pixel seed” is defined as a hit in the pixel detector consistent with a
 547 track extrapolated from the position of the ECAL SC back to the primary vertex.
 548 Real photons, having no charge and therefore no bending in the magnetic field, should
 549 not have a pixel seed.

550 **3.1.2 Electrons**

551 Electrons are reconstructed identically to photons, except that in the electron case
 552 the presence of a pixel seed is enforced, rather than vetoed.² Photons and electrons
 553 are defined by very similar criteria so that $Z \rightarrow ee$ events can be used to model
 554 the QCD background in the two-photon sample without introducing any bias in the
 555 electron energy measurement (cf. Sec. 4.1).

556 **3.1.3 Jets and Missing Transverse Energy**

557 **Particle Flow**

558 In this analysis, jets and \cancel{E}_T are formed from *particle flow* (PF) candidates. The parti-
 559 cle flow algorithm [44, 45] uses information from all CMS subdetectors to reconstruct
 560 as accurately as possible the positions and momenta of all visible jet constituents,
 561 exploiting the fine granularity of the tracker and ECAL to achieve a greatly improved
 562 momentum resolution over calorimeter-only jets [46]. The PF algorithm is summa-
 563 rized below [47].

564 1. Reconstruct the fundamental detector objects via iterative procedures

- 565 • Tracks in the inner silicon layers
 - 566 – High efficiency and low fake rate for charged hadrons in jets
 - 567 – Relaxed primary vertex constraint allows photon conversions, parti-
 568 cles originating from nuclear interactions in the silicon, and long-lived
 569 particles to be reconstructed
- 570 • Calorimeter clusters
- 571 • Muon tracks in the outer muon layers

²In many CMS analyses, electrons are reconstructed very differently from photons. In particular, a special tracking algorithm [43] is used to best follow a radiating electron. However, in this analysis, the electron tracking is not used.

572 2. Create a “block” of linked fundamental objects

- 573 • Link silicon tracks to calorimeter clusters via $\Delta R_{\text{track-cluster}}$ (account for
574 electron bremsstrahlung)
- 575 • Link clusters in one calorimeter layer to clusters in a separate layer via
576 $\Delta R_{\text{cluster-cluster}}$
- 577 • Link silicon tracks to muon tracks via global track χ^2

578 3. ID the particles in the block

- 579 • If global (silicon + muon layers) muon p_T is compatible with silicon track
580 p_T , ID as a muon and remove corresponding tracks from block
- 581 • ID electron tracks via special algorithm and removed all corresponding
582 tracks and cluster from block
- 583 • Remove fake tracks from the block Fixed
- 584 • Remove excess track-cluster links via $\Delta R_{\text{track-cluster}}$ minimization (but al-
585 low multiple tracks to be associated to one cluster) typo
- 586 • If the cluster energy is significantly larger then the energy of the linked
587 track, ID as a PF photon or PF neutral hadron and remove corresponding
588 clusters from the block
- 589 • If the cluster is not linked to a track, ID as a PF photon or PF neutral
590 hadron and remove corresponding clusters from the block
- 591 • Remaining track-cluster links are PF charged hadrons

592 Jets

593 PF candidates are clustered into jets by means of the anti- k_T algorithm with $R = 0.5$
594 [48]. In this algorithm, all possible pairs of PF candidates i, j are looped over, and
595 the momenta of the pair that minimize the distance variable

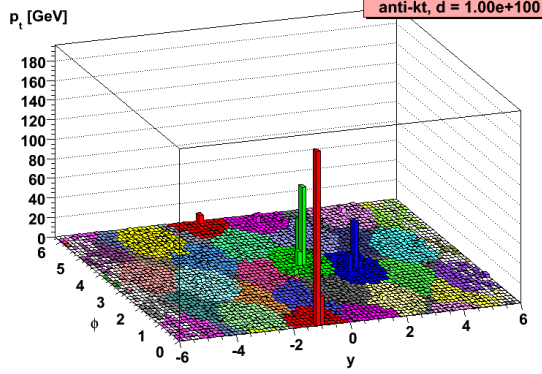


Figure 3.9: Example event display showing jets clustered via the anti- k_T algorithm. y is pseudorapidity.

$$d_{ij} = \frac{\Delta R_{ij}^2}{R^2 \max(k_{Ti}^2, k_{Tj}^2)} \quad (3.4)$$

596 are combined, where k_{Ti} is the transverse momentum of “combined” PF candidate i .
 597 The constituent PF candidates are clustered together. The process is repeated until
 598 $d_{ij} > 1/k_{Ti}^2$ for all pairs of clustered PF momenta [49]. An illustration is given in Fig-
 599 ure 3.9. The anti- k_T algorithm is infrared and collinear safe, leading to well-behaved
 600 theoretical predictions and ease of comparison between data and MC simulation. It
 601 also tends to form circular jets, making it easy for experimental effects such as ex-
 602 pected out-of-cone energy and fiducial acceptance to be measured or simulated. For
 603 these reasons, the anti- k_T jet clustering algorithm was chosen for this analysis.

604 Once jets are clustered, they must be corrected for biases in the energy mea-
 605 surement due to non-compensation [50], invisible energy (lost to overcoming nuclear
 606 binding energy, in neutrinos, or in unclustered muons, for example) [50], detector
 607 geometry and cracks [51], zero suppression and trigger inefficiencies [52], pileup, and
 608 effects of the clustering algorithm [51]. Four multiplicative correction factors are ap-
 609 plied to the raw jet four-momentum p_μ^{raw} [46]:

- 610 • $C_{\text{offset}}(p_T^{\text{raw}})$, which accounts for extra energy due to noise, pileup, and the un-

611 derlying event;

- 612 • $C_{\text{MC}}(C_{\text{offset}}p_T^{\text{raw}}, \eta)$, which is derived from MC and accounts for most of the p_T
 613 and η dependence;
- 614 • $C_{\text{rel}}(\eta)$, which accounts for the remaining differences in uniformity over the
 615 entire calorimeter between data and MC; and
- 616 • $C_{\text{abs}}(C_{\text{rel}}C_{\text{MC}}C_{\text{offset}}p_T^{\text{raw}})$, which accounts for the remaining differences in linear-
 617 ity over the full p_T range between data and MC.

618 Figure 3.10 shows the total jet energy correction factor $C_{\text{offset}}C_{\text{MC}}C_{\text{rel}}C_{\text{abs}}$ vs. η
 619 for jets reconstructed with the anti- k_T algorithm, $R = 0.5$. The PF jet corrections
 620 are more uniform across η than those of CALO jets (composed of simple calorimeter
 621 towers) or JPT jets (Jet Plus Tracks; composed of calorimeter energies replaced,
 622 where possible, with matching track p_T) [53]. In addition, for p_T in the range 30-200
 623 GeV and $|\eta|$ up to 2.0, the PF jet energy correction uncertainty is lower than that of
 624 the other two types of jets, and never exceeds $\sim 3\%$ [46]. The superior performance
 625 of PF jets motivates their use in this search.

626 In this analysis, candidate and QCD control events are binned by number of jets
 627 satisfying the criteria in Table 3.2.

628 Missing Transverse Energy

629 To be consistent with the jet reconstruction, \cancel{E}_T in this analysis is also reconstructed
 630 from PF candidates. Raw \cancel{E}_T is defined as

$$\cancel{E}_{T\text{raw}} = \left| - \sum_{i=1}^{n_{\text{PF}}} \vec{p}_{Ti} \right| \quad (3.5)$$

Table 3.2: Definition of HB/HE hadronic jets.

Variable	Cut
Algorithm	L1FastL2L3Residual corrected PF
p_T	$> 30 \text{ GeV}$
$ \eta $	< 2.6
Neutral hadronic energy fraction	< 0.99
Neutral electromagnetic energy fraction	< 0.99
Number of constituents	> 1
Charged hadronic energy	$> 0.0 \text{ GeV}$ if $ \eta < 2.4$
Number of charged hadrons	> 0 if $ \eta < 2.4$
Charged electromagnetic energy fraction	< 0.99 if $ \eta < 2.4$
ΔR to nearest PF electron ^a , muon ^b , or one of the two primary EM objects	> 0.5

^aA PF electron is defined as an electron reconstructed with the PF algorithm [41] with $p_T > 15 \text{ GeV}$, $|\eta| < 2.6$, and $(I_{\text{charged}} + I_{\text{photon}} + I_{\text{neutral}})/p_T < 0.2$, where $I_{\text{charged}}(I_{\text{photon}})(I_{\text{neutral}})$ is the sum of PF charged hadron(PF photon)(PF neutral hadron) momenta in a $\Delta R = 0.4$ cone around the PF electron.

^bMuons are reconstructed [42] from a combination of muon station and inner tracker hits. Here, a muon must have track $\chi^2 < 10$, at least one good muon station hit, inner track transverse impact parameter $< 0.02 \text{ cm}$, inner track longitudinal impact parameter $< 0.5 \text{ cm}$, $p_T > 15 \text{ GeV}$, $|\eta| < 2.6$, and $(I_{\text{ECAL}} + I_{\text{HCAL}} + I_{\text{track}})/p_T < 0.2$, where $I_{\text{ECAL}}(I_{\text{HCAL}})(I_{\text{track}})$ is the sum of ECAL(HCAL)(track) momenta in a $\Delta R = 0.3$ cone around the muon.

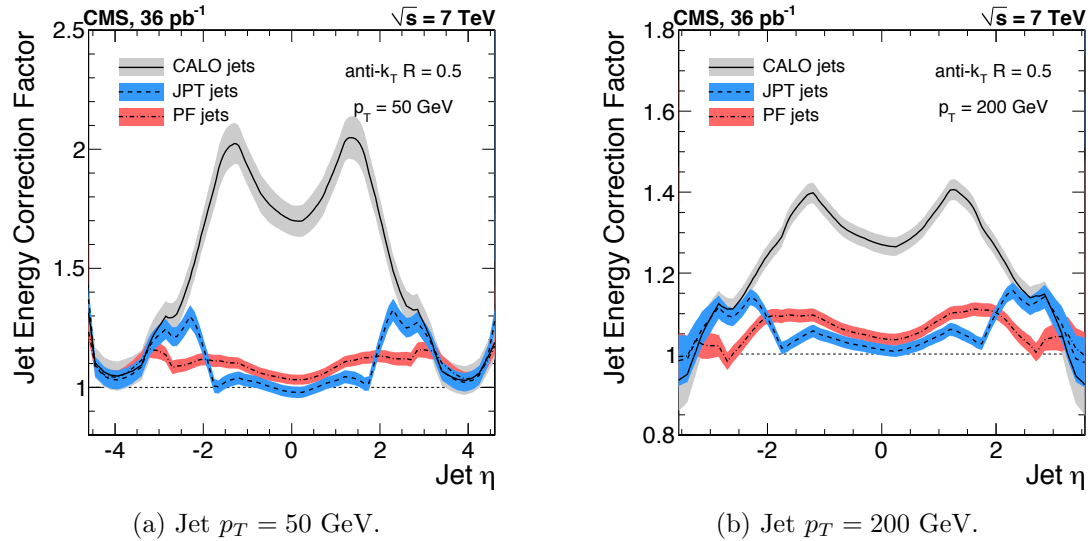


Figure 3.10: Total jet energy correction factor $C_{\text{offset}}C_{\text{MC}}C_{\text{rel}}C_{\text{abs}}$ vs. η , including uncertainty band, for jets reconstructed with the anti- k_T algorithm, $R = 0.5$. Reprinted from Fig. 26 of ref. [46].

where n_{PF} is the number of PF candidates in the event. \cancel{E}_{raw} may be corrected for the same effects that necessitate jet corrections, since \cancel{E}_{raw} is usually the result of jet mis-measurement (except, of course, in electroweak physics processes that include an energetic neutrino, or SUSY production). CMS *Type-I* \cancel{E}_T corrections simply involve replacing the PF jets with their corrected energies (cf. Sec 3.1.3) and recalculating \cancel{E}_T . Only jets with *electromagnetic fraction* (EMF) below 90% and $p_T > 20 \text{ GeV}$ are replaced. This ensures that very electromagnetic jets (as well as isolated leptons, which also receive no correction), which consist chiefly of neutral pions and are measured accurately by the ECAL, do not receive a correction derived for jets with a large fraction of their energy in charged hadrons. In addition, the p_T cut guarantees that jet corrections are only applied where they are known to within a few percent. For this search, the level of agreement between the SM background estimate and the two-photon search sample in a low- \cancel{E}_T control region is the same regardless of whether the \cancel{E}_T is corrected or not, so for simplicity the Type-I \cancel{E}_T corrections are not used (see Sec. ??).

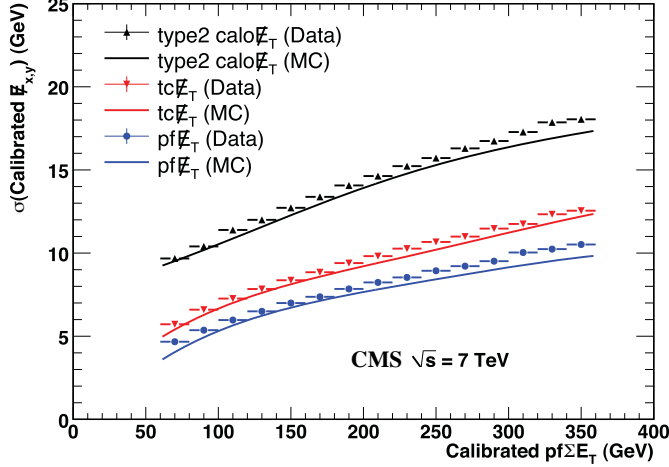


Figure 3.11: σ of a Gaussian fit to the x- and y-components of calibrated E_T vs. the calibrated PF E_T sum in a sample of events containing at least two jets with $p_T > 25$ GeV. σ is calibrated such that the E_T scale is equal for all three algorithms. PF $\sum E_T$ is corrected, on average, to the particle level using a Pythia v8 simulation [54]. The blue markers (data) and line (MC) refer to PF jets. Reprinted from Fig. 13 of ref. [52].

646 Figure 3.11 shows the σ of a Gaussian fit to the x- and y-components of calibrated
 647 E_T vs. the calibrated PF E_T sum in a sample of events containing at least two jets
 648 with $p_T > 25$ GeV. Again, PF E_T outperforms E_T constructed of calorimeter towers
 649 or track-corrected calorimeter deposits.

650 3.2 HLT

651 From the objects described in Sec. 3.1, four samples of events are formed:

- 652 • $\gamma\gamma$ candidate sample, in which the two highest E_T objects are photons,
- 653 • $e\gamma$ control sample, in which the two highest E_T objects are one electron and
 654 one photon,
- 655 • ee control sample, in which the two highest E_T objects are electrons, and
- 656 • ff control sample, in which the two highest E_T objects are fakes.

657 In all samples, the leading EM object is required to have $E_T > 40$ GeV, while the
 658 trailing EM object is required to have $E_T > 25$ GeV. The high level triggers used to
 659 select the four samples, by run range, are listed in Table 3.3. No trigger is prescaled.

Table 3.3: HLT paths triggered by the $\gamma\gamma$, $e\gamma$, ee , and ff samples, by run range. No triggers are prescaled.

Run range	$\gamma\gamma$	$e\gamma$	ee	ff
160404-163261	Photon26_ IsoVL_ Photon18	Photon26_ IsoVL_ Photon18	Photon26_ IsoVL_ Photon18	Photon26_ IsoVL_ Photon18
161216-166967	Photon36_ CaloIdL_ Photon22_ CaloIdL	Photon36_ CaloIdL_ Photon22_ CaloIdL	Photon36_ CaloIdL_ Photon22_ CaloIdL	Photon36_ CaloIdL_ Photon22_ CaloIdL
166347-180252	Photon36_ CaloIdL_ IsoVL_ Photon22_ CaloIdL_ IsoVL	Photon36_ CaloIdL_ IsoVL_ Photon22_ CaloIdL_ IsoVL	Photon36_ CaloIdL_ IsoVL_ Photon22_ R9Id	Photon36_ CaloIdL_ IsoVL_ Photon22_ R9Id
				Photon36_ R9Id_ Photon22_ CaloIdL_ IsoVL
				Photon36_ R9Id_ Photon22_ R9Id

660 Each piece of the HLT path name is defined as follows.

- 661 • “Photon”: Energy deposit in the ECAL that fired an L1 trigger (cf. Sec. ??).

662 For Photon26_IsoVL_Photon18, the L1 seed E_T threshold is 12 GeV, while for
 663 all other triggers in Table 3.3 it is 20 GeV.

664 • Integer following the word “Photon”: E_T threshold in GeV for offline recon-
 665 structed photon, using the full photon reconstruction of Sec. 3.1.1 minus the
 666 laser calibrations and assuming the primary vertex at (0, 0, 0).

667 • “CaloIdL”: For EB photons, $H/E < 0.15$ and $\sigma_{in\eta} < 0.014$.

668 • “IsoVL”: $I_{ECAL} < 0.012E_T + 6$ GeV, $I_{HCAL} < 0.005E_T + 4$ GeV, and $I_{track} <$
 669 $0.002E_T + 4$ GeV.

670 • “R9Id”: $R9 > 0.8$.

671 In addition, the versions of HLT_Photon26_IsoVL_Photon18 and
 672 Photon36_CaloIdL_Photon22_CaloIdL that were active during runs 160404-163268
 673 included a cut $E_{max}/E_{5\times5} < 0.98$ for spike rejection. E_{max} is the energy in the highest
 674 energy crystal of the EM cluster and $E_{5\times5}$ is the energy in the 5×5 crystal matrix
 675 around the seed crystal. For runs after 163268, Swiss cross spike rejection of individual
 676 crystals from HLT quantities was performed (cf. Sec. 3.1.1). All information about the
 677 evolution of the CMS HLT settings can be found in the HLT configuration browser
 678 at <http://j2eeps.cern.ch/cms-project-confdb-hltdev/browser/>.

679 As an example of the naming convention just described, the HLT path Pho-
 680 ton36_CaloIdL_IsoVL_Photon22_R9Id is fired if one photon is found with $E_T > 36$
 681 GeV passing the CaloIdL and IsoVL requirements, and another is found with $E_T > 22$
 682 GeV passing the R9Id requirement.

683 **Add a discussion of trigger efficiency here, with plots.**

684 3.3 Event Quality

685 To suppress instrumental backgrounds, a set of event quality cuts are applied to the
 686 $\gamma\gamma$, $e\gamma$, ee , and ff samples. First, all events are required to pass a good run selec-
 687 tion, as determined by the CMS Physics Validation Team (<https://twiki.cern.ch/twiki/bin/view/CMS/PVTMain>, CERN computing ID needed). The good run selec-
 688 tion excludes luminosity sections during which a sufficient part of the CMS detector
 689 was unpowered or malfunctioning. Such conditions could occur if, for example, a high
 690 voltage supply trips off in the middle of a run, or a DAQ error corrupts data quality
 691 but is not spotted until after the data have been collected. The severity of a detec-
 692 tor problem is judged by its effect on a wide range of analyses and reconstruction
 693 algorithms. Of the **N** fb^{-1} of integrated luminosity delivered by the LHC in 2011,
 694 4.68 fb^{-1} passed the good run selection. This analysis is performed on the entire 2011
 695 certified dataset.

697 Second, all events must contain at least one good interaction vertex. The criteria
 698 for a good vertex are:

699 • $\chi^2 \neq 0 \parallel \text{ndof} \neq 0 \parallel N_{\text{tracks}} \neq 0$, where χ^2 and ndof are calculated for the track
 700 fit to the vertex, and N_{tracks} is the number of tracks in the vertex fit

701 • $\text{ndof} > 4$

702 • $|z| < 24 \text{ cm}$, where z is the z -coordinate of the vertex position

703 • $|\rho| < 2 \text{ cm}$, where ρ is the transverse displacement of the vertex position from
 704 the beam line

705 The good vertex requirement eliminates non-collision backgrounds such as beam
 706 scraping, beam halo, cosmic muon interactions, and instrumental effects.

707 Third, the two electromagnetic objects in the $\gamma\gamma$, $e\gamma$, ee , and ff events must
 708 be separated in ϕ by at least 0.05. This requirement protects against beam halo

709 bremsstrahlung, in which a halo muon traveling parallel to the beam line radiates
710 an energetic photon while itself depositing a large amount of energy in the ECAL.
711 In this case, the two ECAL hits would likely be at the same ϕ (and ρ). An example
712 cartoon is shown in Figure ???. **Insert figure.**

713 Fourth, the two EM objects must be separated in R by at least 0.6. Since the
714 isolation cone size used is 0.3, this ensures that the isolation energy of one EM object
715 cannot be in the veto strip (Fig. 3.5) of the other.

716 Finally, the $\gamma\gamma$, $e\gamma$, ee , and ff events must pass an HCAL noise filter and ECAL
717 dead channel filter. The HCAL noise filter guarantees that all HCAL reconstructed
718 hits are inconsistent with any noise source. Noise sources [55] include:

- 719 • Ion feedback in the HPDs absent any true incident photons, in which a thermal
720 electron ionizes a molecule in the HPD acceleration gap, faking a real signal
- 721 • HPD discharge affecting nearly all channels in the same HPD [56], partially
722 explained by the effect of the 4 T CMS magnetic field on the flashover voltage
723 of the dielectric [58]
- 724 • Concurrent signals in nearly all 72 channels of a single RBX, as yet unexplained
- 725 • HF PMT window hits (as opposed to the usual quartz fiber hits)
- 726 • ADC saturation

727 Since HCAL noise may induce fake jets or E_T , events are rejected if any of the
728 following criteria are true:

- 729 • Any HPD has > 17 hits
- 730 • A single HPD has > 10 hits, but every other HPD has zero hits
- 731 • An RBX has > 10 zero-ADC-count hits

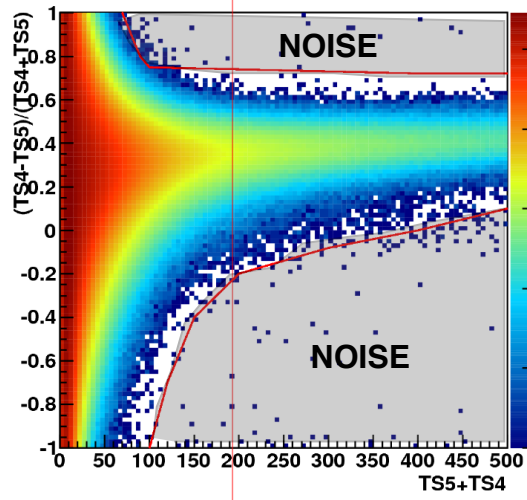


Figure 3.12: $(TS4 - TS5)/(TS4 + TS5)$ vs. $TS4 + TS5$ for a minimum bias sample. HB/HE hits are considered noisy if they lie in the sparsely populated gray region labeled "NOISE" defined by the curved red lines. Adapted from ref. [57].

- 732 • Any HB/HE reconstructed hit corresponding to an RBX with > 50 GeV of
- 733 energy fails a two-dimensional cut defined by the variables $(TS4 - TS5)/(TS4 +$
- 734 $TS5)$ vs. $TS4 + TS5$, where $TS4(TS5)$ is the hit amplitude in the fourth(fifth)
- 735 time sample read out for that hit. The cut is defined in Fig. 3.12.

736 The ECAL dead channel filter is designed to flag events in which significant EM
 737 energy was deposited in a masked region of the ECAL by using the trigger primitive
 738 information for the corresponding trigger tower. Energy deposited in a masked region
 739 of ECAL can cause fake \cancel{E}_T . Events are rejected if the trigger primitive E_T exceeds
 740 the maximum value of 63.75 GeV in any trigger tower that is masked in the readout.

741 **3.4 Photon Identification Efficiency**

742 In order to determine the cross section (or cross section upper limit) for a GGM
 743 signal, the photon identification efficiency is needed. Since no suitably large sample
 744 of $Z \rightarrow \mu\mu\gamma$ events in CMS exists yet, the efficiency calculation relies on the similarity
 745 between detector response to electrons and photons. A scale factor to correct the MC

⁷⁴⁶ photon ID efficiency to the real photon efficiency for the data is obtained from the
⁷⁴⁷ ratio of the electron efficiency from the data to the electron efficiency from MC.

⁷⁴⁸ The different types of photon ID variables—calorimeter and track isolation, ratio
⁷⁴⁹ of hadronic to electromagnetic energy of the shower, and transverse shower shape—
⁷⁵⁰ are chosen so that their distributions for isolated electrons and photons are similar.³
⁷⁵¹ Figure ?? shows distributions of photon ID variables for MC electrons and photons,
⁷⁵² where a MC electron(photon) is a `reco::Photon` object matched to a generated
⁷⁵³ electron(photon) originating from a Z decay(the hard interaction) within $\Delta R = 0.3$.
⁷⁵⁴ MC electrons come from the DYJets0LL sample, while MC photons come from the
⁷⁵⁵ GJet sample (see Appendix A). **Make these plots.** The shapes of the distributions
⁷⁵⁶ agree well. **Also include data/MC comparisons?**

⁷⁵⁷ The photon selection efficiency is

$$\epsilon_{\gamma} = \epsilon_{\gamma}^{\text{MC}} \times \frac{\epsilon_e^{\text{data}}}{\epsilon_e^{\text{MC}}} \quad (3.6)$$

⁷⁵⁸ where

- ⁷⁵⁹ • ϵ_{γ} is the photon ID efficiency in data,
- ⁷⁶⁰ • $\epsilon_{\gamma}^{\text{MC}}$ is the photon ID efficiency in MC,
- ⁷⁶¹ • ϵ_e^{data} is the electron ID efficiency obtained using $Z \rightarrow ee$ electrons in the data
⁷⁶² that satisfy the photon ID cuts, and
- ⁷⁶³ • ϵ_e^{data} is the electron ID efficiency obtained using $Z \rightarrow ee$ electrons in MC that
⁷⁶⁴ satisfy the photon ID cuts.

⁷⁶⁵ The ratio $\epsilon_e^{\text{data}}/\epsilon_e^{\text{MC}}$ is defined as the scale factor by which the GGM signal MC
⁷⁶⁶ photon ID efficiency must be multiplied to give an estimate of the photon ID efficiency

³ $R9$ differs between photons and radiating electrons, but the requirement $R9 < 1$ is loose enough not to introduce problems with the use of electrons to measure the photon ID efficiency.

⁷⁶⁷ in data. The photon ID requirements of Table 3.1 plus the IsoVL HLT requirement
⁷⁶⁸ described in Sec. 3.2 and Table 3.3 are repeated in Table 3.4.

Table 3.4: Candidate photon ID requirements.

Variable	Cut
I_{ECAL}	$< 0.012E_T + 6 \text{ GeV}$
I_{HCAL}	$< 0.005E_T + 4 \text{ GeV}$
I_{track}	$< 0.002E_T + 4 \text{ GeV}$
H/E	< 0.05
$\sigma_{i\eta i\eta}$	< 0.011
$I_{\text{ECAL}} - 0.0792\rho + I_{\text{HCAL}} - 0.0252\rho + I_{\text{track}}$	$< 6 \text{ GeV}$
$R9$	< 1

⁷⁶⁹ 3.4.1 Tag and Probe Method

⁷⁷⁰ A *Z tag and probe* method is utilized to measure the efficiency of the photon ID
⁷⁷¹ cuts in Table 3.1. The tag is a well-identified electron. The probe, by contrast, is as
⁷⁷² loosely identified as possible, and all tags must pass the probe criteria in addition to
⁷⁷³ the stringent tag criteria. The tag and probe criteria used in this study are shown in
⁷⁷⁴ Table 3.5.

⁷⁷⁵ The invariant mass of the tag and probe are required to be within a narrow window
⁷⁷⁶ around Z mass. Assuming that the probabilities of the tag and probe legs of the Z
⁷⁷⁷ decay to pass the photon ID cuts are uncorrelated, the efficiency can be estimated as

$$\epsilon = \frac{N_{\text{tag-pass}}}{N_{\text{tag-pass}} + N_{\text{tag-fail}}} \quad (3.7)$$

⁷⁷⁸ where $N_{\text{tag-pass}}$ is the number of tag-probe pairs in which the probe leg passes the
⁷⁷⁹ photon ID cuts under study and $N_{\text{tag-fail}}$ is the number of tag-probe pairs in which
⁷⁸⁰ the probe leg fails the cuts. Implicit in these definitions is a double counting of pairs
⁷⁸¹ in which both electrons pass the tag and probe criteria [59]. In addition, in the rare

Table 3.5: Tag and probe criteria. The superscript 0.4 indicates that the isolation variable was calculated in a cone of $\Delta R = 0.4$ around the photon candidate. The isolations without superscripts use the standard $\Delta R = 0.3$ cones.

Variable	Cut	
	Tag	Probe
RECO object	photon	photon
HLT	HLT_Ele17_CaloIdVT_CaloIsoVT_TrkIdT_-TrkIsoVT_SC8_Mass30_v* (must have fired the 17 GeV leg)	—
H/E	< 0.05	< 0.15
$I_{\text{ECAL}}^{0.4}$	$< 0.006E_T + 4.2 \text{ GeV}$	—
$I_{\text{HCAL}}^{0.4}$	$< 0.0025E_T + 2.2 \text{ GeV}$	—
$I_{\text{track}}^{0.4}$	$< 0.001E_T + 2.0 \text{ GeV}$	—
E_T	$> 25 \text{ GeV}$	—
SC E_T	—	$> 15 \text{ GeV}$
SC $ \eta $	< 1.4442	< 1.4442
$\sigma_{in\eta}$	< 0.009	—
Has pixel seed?	Yes	—
Track match type	General track	—
Track match ΔR	< 0.04	—
Track match p_T	$> 15 \text{ GeV}$	—
Track match $ \eta $	< 1.479	—

782 circumstance (less than 1% in MC [59]) that two or more probes may be matched to
 783 one tag, the pair with invariant mass closest to the Z mass is chosen.

784 In practice, $N_{\text{tag-pass}}$ and $N_{\text{tag-fail}}$ are returned by a simultaneous unbinned maxi-
 785 mum likelihood fit to the invariant mass distributions of tag-pass and tag-fail events,
 786 with appropriate signal and background PDF assumptions. The fit form used is

$$\begin{aligned} f_{\text{tag-pass}}(m_{\text{tag-pass}}) &= \epsilon N_S f_S^{\text{pass}}(m_{\text{tag-pass}}) + N_B^{\text{pass}} f_B^{\text{pass}}(m_{\text{tag-pass}}) \\ f_{\text{tag-fail}}(m_{\text{tag-fail}}) &= (1 - \epsilon) N_S f_S^{\text{fail}}(m_{\text{tag-fail}}) + N_B^{\text{fail}} f_B^{\text{fail}}(m_{\text{tag-fail}}) \end{aligned} \quad (3.8)$$

787 where $f_{\text{tag-pass}}(m_{\text{tag-pass}})$ and $f_{\text{tag-fail}}(m_{\text{tag-fail}})$ are the tag-pass and tag-fail PDFs,
 788 respectively; ϵ is the efficiency; N_S is the total number of Z signal events summed over
 789 both samples; $f_S^{\text{pass}}(m_{\text{tag-pass}})$ and $f_S^{\text{fail}}(m_{\text{tag-fail}})$ are the tag-pass and tag-fail signal
 790 PDFs, respectively; N_B^{pass} and N_B^{fail} are the numbers of background events in the tag-
 791 pass and tag-fail samples, respectively; and $f_B^{\text{pass}}(m_{\text{tag-pass}})$ and $f_B^{\text{fail}}(m_{\text{tag-fail}})$ are the
 792 tag-pass and tag-fail background PDFs, respectively. This particular implementation
 793 of the tag and probe methodology is based on tag CMSSW_4_2_5 of the CMSSW
 794 package PhysicsTools/TagAndProbe, and uses the MINUIT2 [60] library, as coded
 795 in RooFit [61], for the likelihood maximization. For this study, CMSSWv4.2.8 was
 796 used.

797 For both samples, the signal shape is assumed to be a Crystal Ball function [62]
 798 convoluted with the Z generated lineshape, while the background shape is a PDF that
 799 describes the falling background as well as the kinematic turn-on at low invariant
 800 mass. The background PDF, called ‘‘RooCMSShape’’ [59], is given by

$$\text{RooCMSShape}(x) = \begin{cases} 1e20 & \text{for } (x - \mu)\gamma < -70 \\ 0 & \text{for } (x - \mu)\gamma > 70 \\ \text{erfc}((\alpha - x)\beta) \exp(-(x - \mu)\gamma) & \text{otherwise} \end{cases} \quad (3.9)$$

where α , β , γ , and μ are parameters of the fit, most of which are held fixed. In the three lowest E_T bins, all parameters of the tag-pass and tag-fail background PDFs are left floating, because the effect of the relaxed E_T cuts has a significant effect on the background shape. More details of the signal and background PDFs are given in Table 3.6. The fixed signal and background parameter values were determined by fitting a small sample ($0.0 \leq \eta < 0.25$) of Fall11 MC signal (DYJetsToLL) and background (QCD_Pt-20to30_BCtoE, QCD_Pt-30to80_BCtoE, QCD_Pt-80to170_BCtoE, GJet_Pt-20_doubleEMEnriched, WJetsToLNu, TTJets) with parameters left floating.

Some fit examples are shown in Figures ?? and ???. In Fig. ??, which shows fits to data and MC for $15 \text{ GeV} \leq \text{probe } E_T \leq 20 \text{ GeV}$, the kinematic turn-on is below the invariant mass range covered by the plot. The exponentially falling background is easily seen underneath the signal, and is especially pronounced in the background-dominated tag-fail sample. **Include these plots.**

3.4.2 Photon Efficiency Scale Factor $\epsilon_e^{\text{data}}/\epsilon_e^{\text{MC}}$

Figure 3.13 shows the dependence of the photon ID efficiency scale factor $\epsilon_e^{\text{data}}/\epsilon_e^{\text{MC}}$ on E_T , η , $\Delta R_{\gamma\text{jet}}$, and N_{jet} , where jets are defined as in Sec. 3.5.2 ([insert reference to “Jet Selection” section here](#)). **$\Delta R_{\gamma\text{jet}}$ plot will be added during second round.** Errors are statistical only. For the plot of the scale factor vs. $\Delta R_{\gamma\text{jet}}$, only events with ≥ 1 jets are included. There is no significant dependence of the scale factor on these variables, so only one scale factor is computed from the entire dataset.

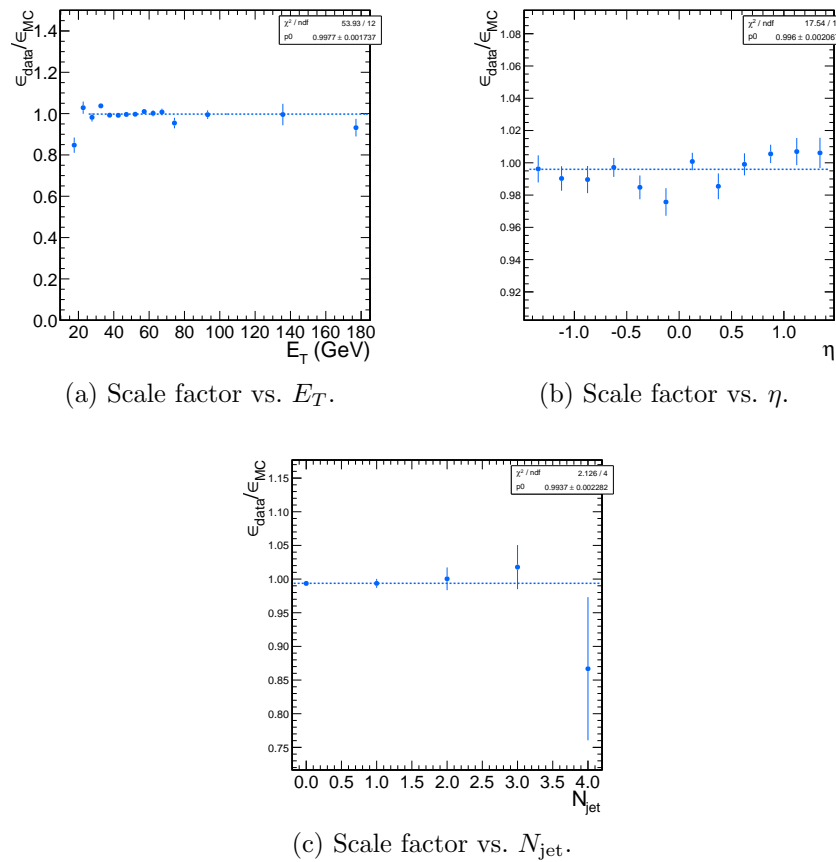


Figure 3.13: Dependence of the photon ID efficiency scale factor on some kinematic variables. Errors are statistical only.

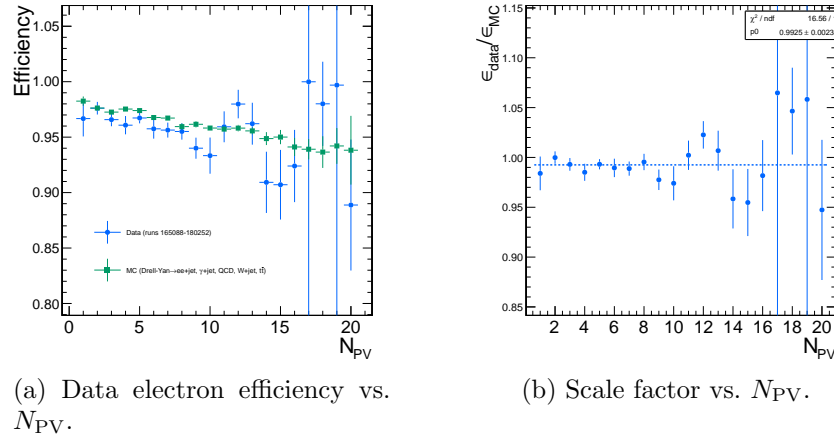


Figure 3.14: Dependence of the photon ID efficiency scale factor on the number of primary vertices per event. Errors are statistical only.

The effect of pileup is studied by comparing the efficiencies ϵ_e^{data} and ϵ_e^{MC} vs. the number of primary vertices (N_{PV}) in the event. The efficiency drops for events with large N_{PV} , even after using pileup-corrected isolation cuts, as can be seen in Figure 3.14a. However, the MC tracks the data, and the scale factor is flat vs. N_{PV} , as shown in Fig. 3.14b.

The scale factor is measured to be $\epsilon_e^{\text{data}}/\epsilon_e^{\text{MC}} = 0.994 \pm 0.002(\text{stat.}) \pm ?(\text{syst.})$. Four main sources of systematic error, in addition to the statistical error of 0.2%, were studied.

Different behavior of electrons and photons in MC Even though the photon ID cuts are designed to be similarly efficient for both electrons and photons, there might be a small difference in the performance between the two kinds of particles, e.g. because of electron bremsstrahlung. To check this effect, the MC electron ID efficiency was calculated using a $Z \rightarrow ee$ sample and the MC photon ID efficiency was calculated using a $\gamma + \text{jets}$ sample. Both samples were reconstructed in CMSSWv3.6. Half the difference between these two results, 0.5%, was taken as an error on the scale factor. **This result is now out of date because it used an older selection. Should this check be redone?**

838 **Pileup** To account for the possibility that the MC simulation may not adequately
 839 reproduce the data in a high pileup environment, the data/MC scale factor
 840 for events with 1-4 good reconstructed primary vertices was calculated, along
 841 with the same for events with ≥ 7 good reconstructed primary vertices. This
 842 particular division of the data was chosen because the pileup distribution in
 843 data peaks at ~ 7 primary vertices per event. The difference between the scale
 844 factors from both samples, ?, was taken as an error on the scale factor from
 845 pileup.

846 **Signal fit over/underestimation** It was found that the signal fit slightly under-
 847 estimates the data in the tag-pass sample, and slightly overestimates it in the
 848 tag-fail sample. To cover this effect with a systematic error, the efficiencies in
 849 data and MC, and then the scale factor, were recalculated using the background
 850 (from fit) subtracted integrals of the tag-pass and tag-fail distributions, rather
 851 than the fitted signal yields in those distributions. The difference between the
 852 scale factor found in this way and the nominal scale factor, ?, was taken as an
 853 error on the scale factor. **Not sure this is a problem anymore.**

854 **Signal and background shape assumption** The largest source of systematic er-
 855 ror comes from the signal and background shape assumptions. To assess the
 856 magnitude of this error, the tag-pass and tag-fail tail parameters (Crystal Ball
 857 ? and n) were varied by $\pm 1\sigma$, and the background shape was varied between
 858 “RooCMSShape, exponential, power law, and quadratic. All possible combi-
 859 nations of varied parameters were generated, and the data and MC were refit
 860 and new scale factors generated according to those combinations. The error was
 861 taken as the largest deviation of the scale factor from nominal, ?%. **Also, in**
 862 **many bins, there is zero background fitted under the tag-pass peak.**
 863 **Background is a small effect here anyway, but we should get a sys-**

864 tematic for this somehow.

865 Add in a MC estimate of the pixel veto efficiency with varied tracker

866 geometries.

Table 3.6: Parameter values for the signal and background PDFs for the different samples. The background PDF applies to all efficiency bins except the four lowest E_T bins, which use a floating RooCMSShape background. When a bracketed range is given, the parameter is allowed to float within that range. When a constant is given, the parameter is fixed to that constant.

PDF	Crystal Ball fit parameters				RooCMSShape fit parameters			
	μ	σ	α	n	μ	α	β	γ
Tag-pass signal	[-1.0, 1.0]	[1.0, 3.0]	0.87	97.0	N/A	N/A	N/A	N/A
Tag-fail signal	[-1.0, 1.0]	[1.0, 3.0]	0.73	134.9	N/A	N/A	N/A	N/A
Tag-pass background	N/A	N/A	N/A	N/A	65.0	61.949	0.04750	0.01908
Tag-fail background	N/A	N/A	N/A	N/A	α	[50.0, 100.0]	0.065	0.048

867

Chapter 4

868

Data Analysis

869 The signature of GGM SUSY particle production in this search is an excess of two-
870 photon events with high \cancel{E}_T . \cancel{E}_T is reconstructed using the particle flow algorithm
871 as described in Sec. 3.1.3. Candidate two-photon events, as well as control events,
872 are selected according to the offline object criteria presented in Secs. 3.1.1, 3.1.2,
873 and 3.1.3; the event quality criteria in Sec. 3.3; and the trigger requirements in Sec. 3.2.
874 These are summarized in Table 4.1.

Table 4.1: Selection criteria for $\gamma\gamma$, $e\gamma$, ee , and ff events.

Variable	Cut			
	$\gamma\gamma$	$e\gamma$	ee	ff
HLT match	IsoVL	IsoVL	IsoVL	IsoVL R9Id
E_T	$> 40/ > 25 \text{ GeV}$			
$\text{SC } \eta $	< 1.4442	< 1.4442	< 1.4442	< 1.4442
H/E	< 0.05	< 0.05	< 0.05	< 0.05
$R9$	< 1	< 1	< 1	< 1
Pixel seed	No/No	Yes/No	Yes/Yes	No/No
$I_{\text{comb}}, \sigma_{inj\eta}$	$< 6 \text{ GeV} \&& < 0.011$	$< 6 \text{ GeV} \&& < 0.011$	$< 6 \text{ GeV} \&& < 0.011$	$< 20 \text{ GeV} \&& (\geq 6 \text{ GeV} \parallel \geq 0.011)$
JSON	Yes	Yes	Yes	Yes
No. good PVs	≥ 1	≥ 1	≥ 1	≥ 1
ΔR_{EM}	> 0.6	> 0.6	> 0.6	> 0.6
$\Delta\phi_{\text{EM}}$	≥ 0.05	≥ 0.05	≥ 0.05	≥ 0.05

875 This search utilizes 4.7 fb^{-1} of CMS data collected during the period April
 876 December 2011, corresponding to the following datasets [63]:

- 877 • /Photon/Run2011A-05Jul2011ReReco-ECAL-v1/AOD
- 878 • /Photon/Run2011A-05Aug2011-v1/AOD
- 879 • /Photon/Run2011A-03Oct2011-v1/AOD
- 880 • /Photon/Run2011B-PromptReco-v1/AOD

881 The search strategy is to model the backgrounds to the GGM SUSY signal using
 882 \cancel{E}_T shape templates derived from the control samples, and then to look for a high- \cancel{E}_T
 883 excess above the estimated background in the $\gamma\gamma$ sample. There are two categories
 884 of backgrounds: QCD processes with no real \cancel{E}_T and electroweak processes with real
 885 \cancel{E}_T from neutrinos. The relevant QCD background processes are multijet production
 886 with at least two jets faking photons, photon + jet production with at least one jet
 887 faking a photon, and diphoton production, and Z production with a radiated photon
 888 where at least one of the Z decay products (typically a jet) fakes a photon. The
 889 relevant electroweak background processes, which are small compared to the QCD
 890 background, involve $W \rightarrow e\nu$ decay with a recoiling jet that fakes a photon or a
 891 real radiated photon (the W may come from the decay of a top quark in $t\bar{t}$ events).
 892 In both cases, the electron is misidentified as a photon due to a small inefficiency
 893 in reconstructing the electron pixel seed. The main diagrams contributing to the
 894 QCD(electroweak) backgrounds are shown in Figure 4.1(4.2).

895 Data control samples are used to model all of the backgrounds. The primary
 896 control sample used to model the QCD background is the ff sample, which is similar
 897 to the candidate $\gamma\gamma$ sample but with combined isolation or $\sigma_{inj\eta}$ cuts inverted. The cuts
 898 on these variables are used to distinguish between photons and jets, so by inverting
 899 those cuts, the resulting ff sample becomes enriched with QCD dijets. Because the

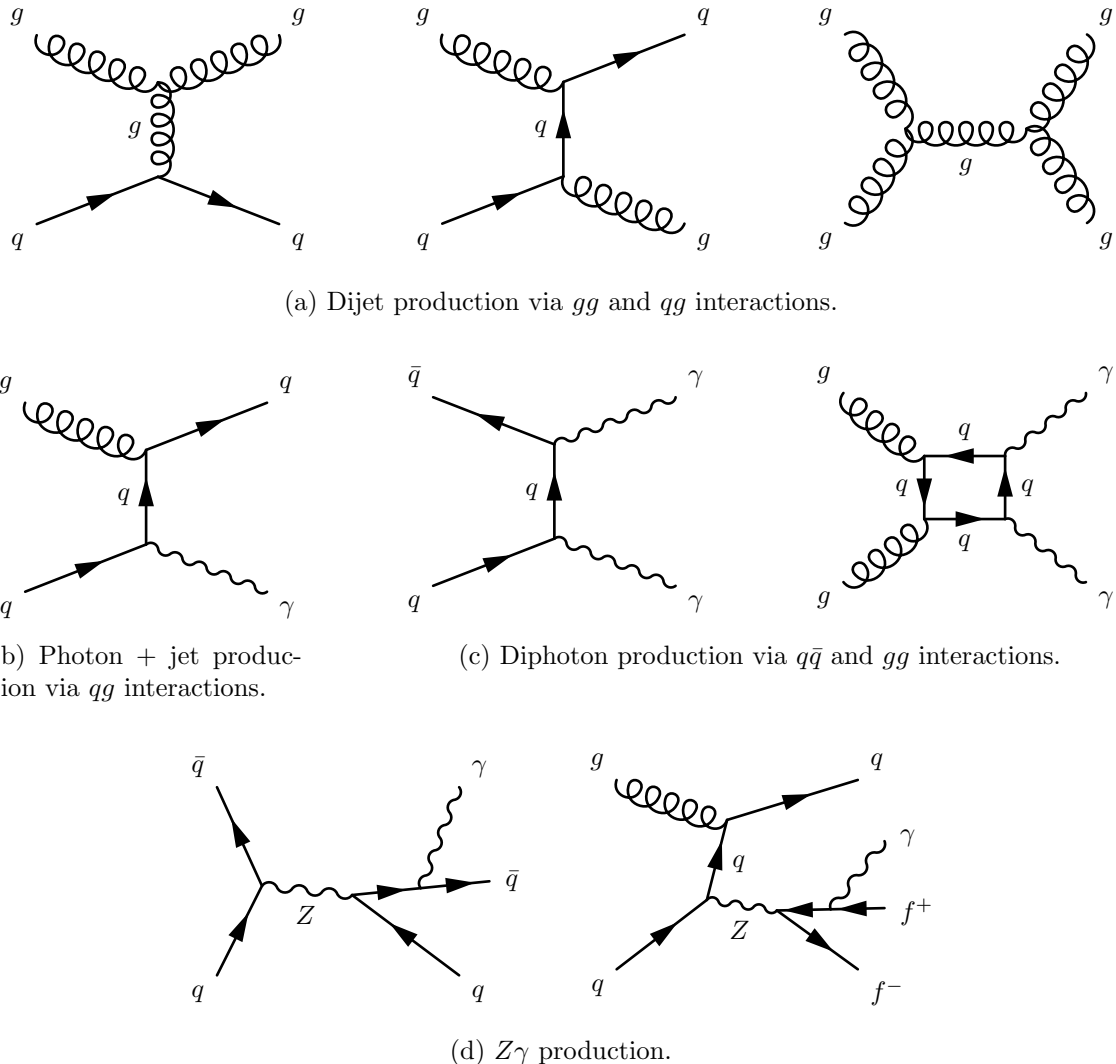


Figure 4.1: Representative Feynman diagrams of some QCD backgrounds to the GGM SUSY search.

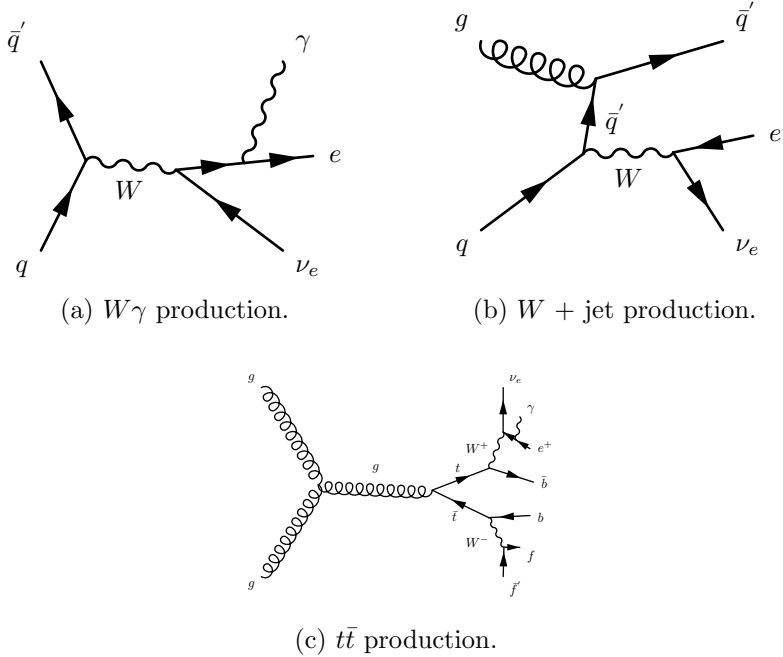


Figure 4.2: Representative Feynman diagrams of some electroweak backgrounds to the GGM SUSY search.

fake photons are still required to pass a tight cut on H/E , they are guaranteed to be very electromagnetic jets, with an EM energy scale and resolution similar to that of the candidate photons. This insures that the resulting estimate of the \cancel{E}_T shape does not have too long of a tail from severe HCAL mis-measurements that are actually rare in the $\gamma\gamma$ sample.

As a cross-check, the ee sample is also used to model the QCD background. This sample of Z decays should have no true \cancel{E}_T , just like the ff sample, and the electron definition (differing from the photon definition only in the presence of a pixel seed) insures that the electron energy scale and resolution is similar to that of the photon.

Finally, the $e\gamma$ sample is used to model the electroweak background from $W \rightarrow e\nu$ decays. The $e\gamma$ \cancel{E}_T distribution is scaled by the electron \rightarrow photon misidentification rate to predict the number of $W\gamma$, $W +$ jet, and $t\bar{t}$ events in the $\gamma\gamma$ sample.

The remainder of this chapter describes the data analysis procedures and the final results of the search. Sec. 4.1 addresses the QCD background estimation. Sec. 4.2

914 addresses the electroweak background estimation. The chapter concludes with a dis-
 915 cussion of systematic errors in Sec. 4.3 and a presentation of the final results in
 916 Sec. 4.4.

917 4.1 Modeling the QCD Background

918 4.1.1 Outline of the Procedure

919 Due to the fact that the CMS ECAL energy resolution is much better than the
 920 HCAL energy resolution, the energies of the two candidate photons in the events of
 921 the $\gamma\gamma$ sample are typically measured to far greater accuracy and precision than the
 922 energy of the hadronic recoil in those events. Therefore, fake E_T in the $\gamma\gamma$ sample
 923 is almost entirely the result of hadronic mis-measurement in QCD dijet, photon +
 924 jet, and diphoton events. The strategy employed to model this background is to find
 925 a control sample in data consisting of two well-measured EM objects, just like the
 926 candidate $\gamma\gamma$ sample, and assign each event a weight to account for the underlying
 927 kinematic differences between the control and candidate samples. Once the reweighted
 928 E_T spectrum of the control sample is created, it is then normalized in the low- E_T
 929 region, the assumption being that GGM SUSY does not predict a significant amount
 930 of events at low E_T . There are three aspects of this QCD background estimation
 931 procedure that bear highlighting:

932 **Choice of control sample** Since the underlying cause of E_T in the candidate sam-
 933 ple is mis-measured hadronic activity, a control sample with similar hadronic
 934 activity to the candidate sample should be chosen. Hadronic activity refers to
 935 number of jets, jet E_T , pileup, etc.

936 **Reweighting** The control sample is reweighted so that its E_T spectrum appears as it
 937 would if the control sample had the same kinematic properties as the candidate

sample (i.e. particle p_T and η distributions, etc.). By choosing an appropriate control sample and reweighting it, the control \cancel{E}_T distribution should now match both the hadronic activity and the kinematics of the candidate sample.

Normalization Finally, the control E_T distribution is normalized in a region of low \cancel{E}_T , where contamination from the expected GGM SUSY signal is small. This implies an extrapolation of the low- \cancel{E}_T QCD background prediction to the high- \cancel{E}_T signal region.

As explained in the beginning of this chapter, the ff sample is used as the primary QCD control sample, while the ee sample is used as a cross-check. Both samples have two well-measured EM objects per event, no real \cancel{E}_T , and similar hadronic activity to the $\gamma\gamma$ sample. Figure 4.3 shows a comparison of the shapes of some distributions relevant to hadronic activity between the $\gamma\gamma$, ee , and ff samples. In general, the ee sample has less hadronic activity than the $\gamma\gamma$ and ff samples, as shown by the more steeply falling ee distributions in Figs. 4.3a, 4.3b, 4.3c, and 4.3d. In addition to the kinematic reweighting, there is also a reweighting by number of jets per event, which attempts to correct for this difference (see Sec. 4.1.2).

4.1.2 Reweighting

To reweight the control sample events to match the kinematics of the candidate sample events, a weight based on the p_T of the di-EM-object system and the number of jets in the event is used. As explained in Sec. 4.1.1, E_T in the $\gamma\gamma$, ff , and ee samples is due to the poorly measured hadronic recoil off the well-measured di-EM system. Therefore, the p_T of the di-EM system is a good handle on the true magnitude of the hadronic recoil, which affects the measured \cancel{E}_T . The di-EM system is depicted in Figure 4.4. As shown in Figure 4.5, \cancel{E}_T is largely uncorrelated with di-EM p_T , so there is little danger of reweighting away a true signal excess.

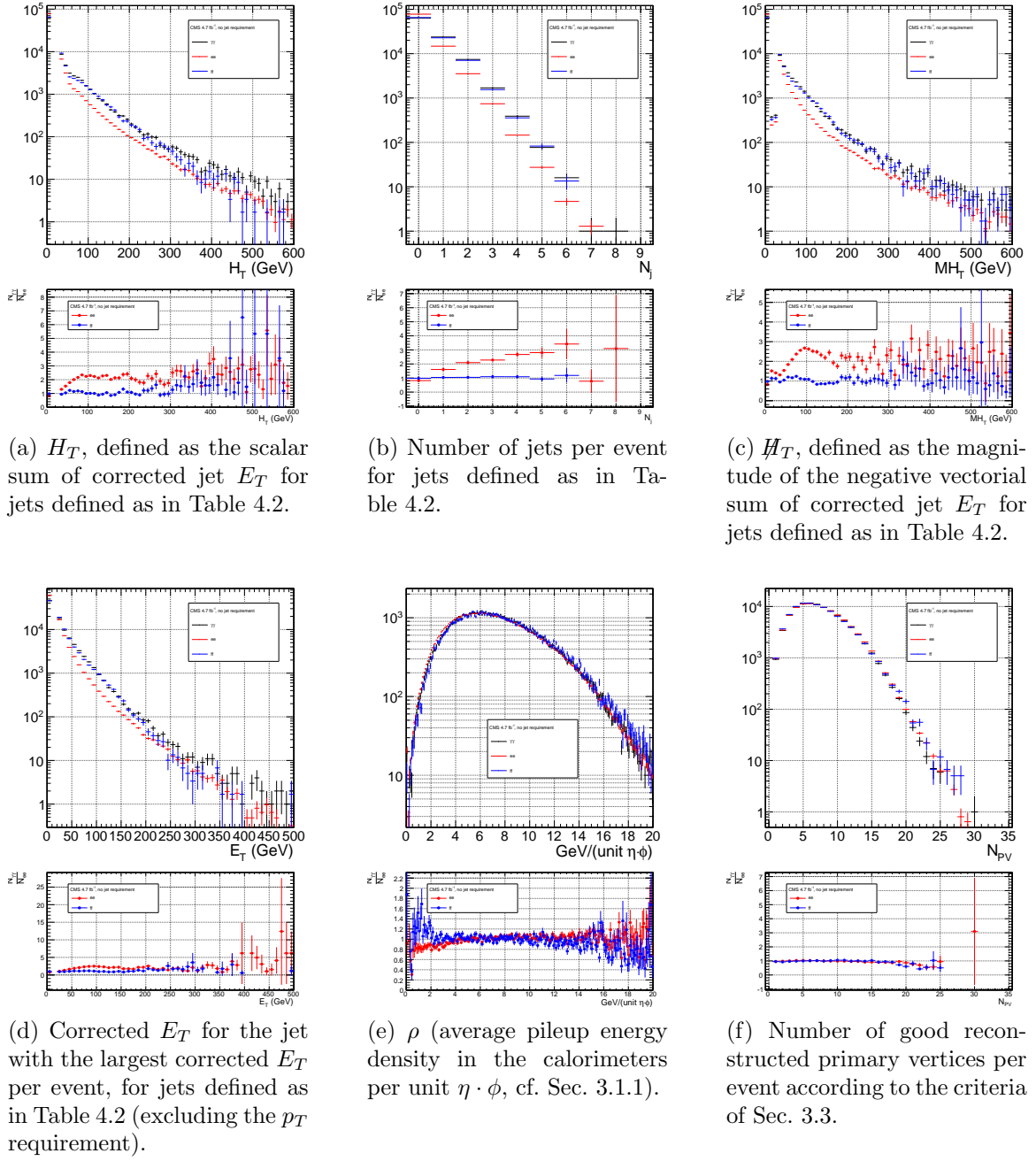


Figure 4.3: Comparison of the shapes of some distributions relevant to hadronic activity between the $\gamma\gamma$, ee ($81 \text{ GeV} \leq m_{ee} < 101 \text{ GeV}$), and ff samples. The ee and ff distributions are normalized to the number of events in the $\gamma\gamma$ distribution. Errors are statistical only.

Table 4.2: Definition of HB/HE/HF hadronic jets.

Variable	Cut
Algorithm	L1FastL2L3Residual corrected PF (cf. Sec. 3.1.3)
p_T	$> 30 \text{ GeV}$
$ \eta $	< 5.0
Neutral hadronic energy fraction	< 0.99
Neutral electromagnetic energy fraction	< 0.99
Number of constituents	> 1
Charged hadronic energy	$> 0.0 \text{ GeV}$ if $ \eta < 2.4$
Number of charged hadrons	> 0 if $ \eta < 2.4$
Charged electromagnetic energy fraction	< 0.99 if $ \eta < 2.4$
ΔR to nearest PF electron ^a , muon ^b , or one of the two primary EM objects	> 0.5

^aA PF electron is defined as an electron reconstructed with the PF algorithm [41] with $p_T > 15 \text{ GeV}$, $|\eta| < 2.6$, and $(I_{\text{charged}} + I_{\text{photon}} + I_{\text{neutral}})/p_T < 0.2$, where $I_{\text{charged}}(I_{\text{photon}})(I_{\text{neutral}})$ is the sum of PF charged hadron(PF photon)(PF neutral hadron) momenta in a $\Delta R = 0.4$ cone around the PF electron.

^bMuons are reconstructed [42] from a combination of muon station and inner tracker hits. Here, a muon must have track $\chi^2 < 10$, at least one good muon station hit, inner track transverse impact parameter $< 0.02 \text{ cm}$, inner track longitudinal impact parameter $< 0.5 \text{ cm}$, $p_T > 15 \text{ GeV}$, $|\eta| < 2.6$, and $(I_{\text{ECAL}} + I_{\text{HCAL}} + I_{\text{track}})/p_T < 0.2$, where $I_{\text{ECAL}}(I_{\text{HCAL}})(I_{\text{track}})$ is the sum of ECAL(HCAL)(track) momenta in a $\Delta R = 0.3$ cone around the muon.

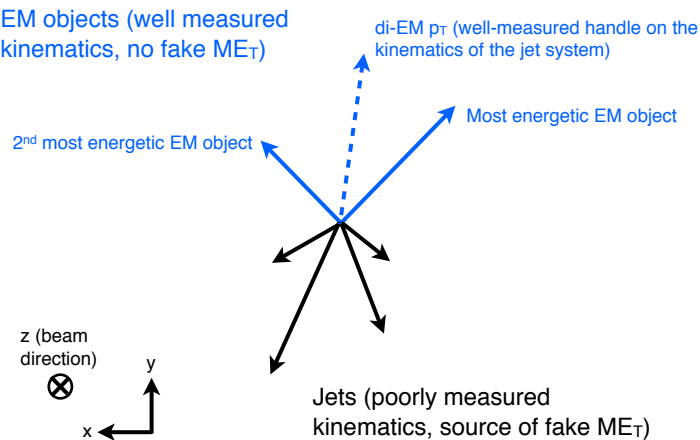


Figure 4.4: Cartoon showing the di-EM system in blue and the hadronic recoil in black. The di-EM p_T (dashed blue line) is used to reweight the control sample kinematic properties to match those of the candidate $\gamma\gamma$ sample.

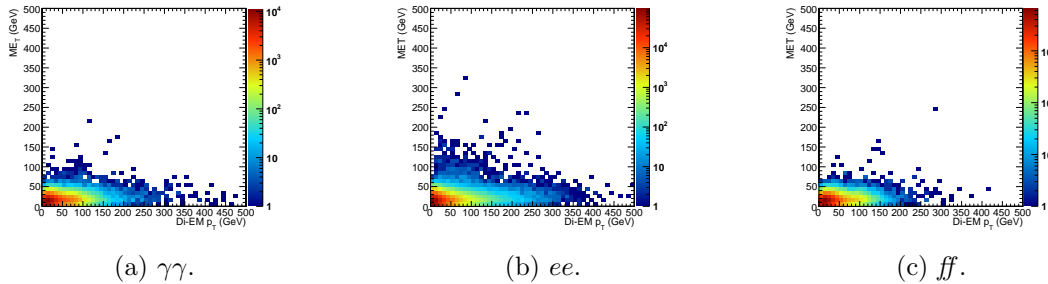


Figure 4.5: E_T vs. di-EM p_T .

Whereas the di-EM p_T reweighting accounts for differences in production kinematics between the control and $\gamma\gamma$ samples, a simultaneous reweighting based on the number of jets in the event accounts for differences in hadronic activity between the samples, especially between ee and $\gamma\gamma$ (cf. Fig. 4.3). Jets are defined as in Table 3.2. Figure 4.6 shows the effect of reweighting by number of jets per event, which is to increase(decrease) the tail of the $ee(ff) E_T$ spectrum.

Although the electron and photon energies are well measured by the ECAL, the
 ECAL-only measurement of the fake photon energy (cf. Sec 3.1.1) is biased slightly
 low due to the fact that fakes (which are really jets) tend to deposit some energy in
 the HCAL. This can be seen in Figs. 4.7 and 4.8, which show the relative difference
 between the ECAL-only E_T measurement and the PF E_T measurement vs. EMF for
 electrons, photons, and fakes. PF E_T is defined as the L1Fast-corrected E_T of the
 nearest PF jet with $p_T \geq 20$ GeV (i.e., the E_T of the PF jet object reconstructed from
 the same ECAL shower as the fake photon). On average, the fakes tend to deposit
 a few percent more energy in the HCAL than the electrons or photons, which is
 recovered by the PF algorithm. For this reason, the PF p_T is used in the calculation
 of di-EM p_T rather than the ECAL-only p_T .¹ This leads to a modest improvement in
 the agreement between the ee and ff E_T spectra, as shown in Figure 4.9.

981 The control sample event weights are defined as

¹In the few events ($\mathcal{O}(10^{-3})$) in which two PF jet objects, corresponding to the two electrons or fakes, are not found, the ECAL-only p_T is used.

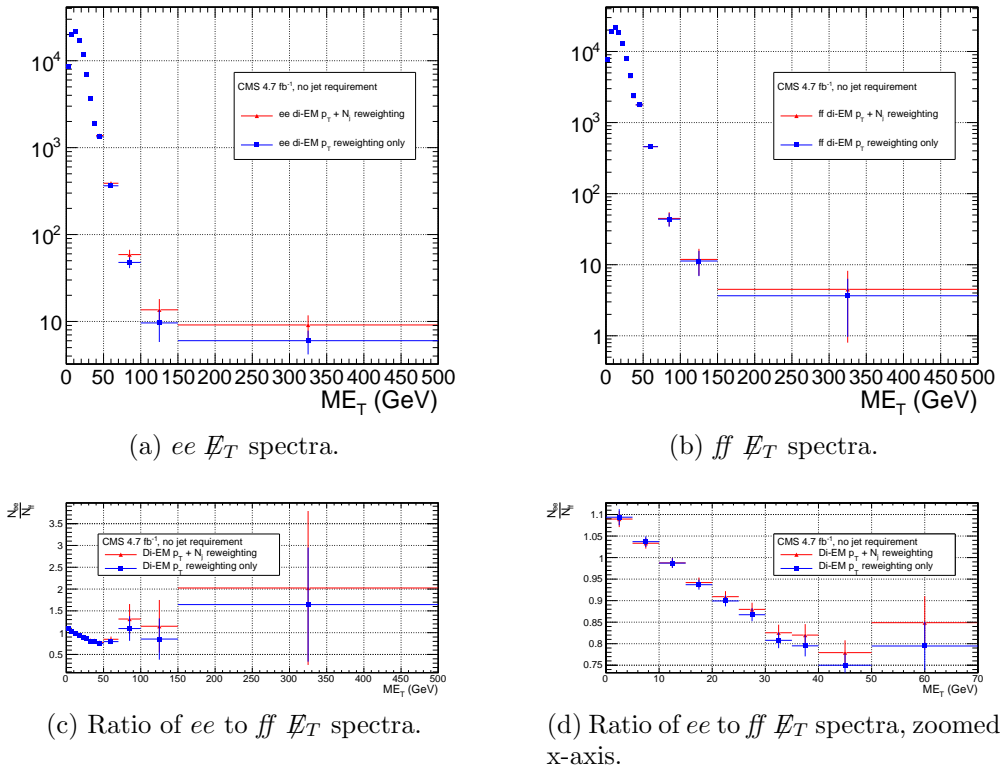


Figure 4.6: \mathbb{E}_T spectra of the reweighted ee ($81 \text{ GeV} \leq m_{ee} < 101 \text{ GeV}$) and ff control samples. Blue squares indicate di-EM p_T reweighting only; red triangles indicate di-EM $p_T + \text{number of jets}$ reweighting. PF p_T (cf. p. 71) is used to calculate the di-EM p_T . The full normalization procedure is employed, along with ee sideband subtraction (discussed at the end of this section). Error bars are statistical only.

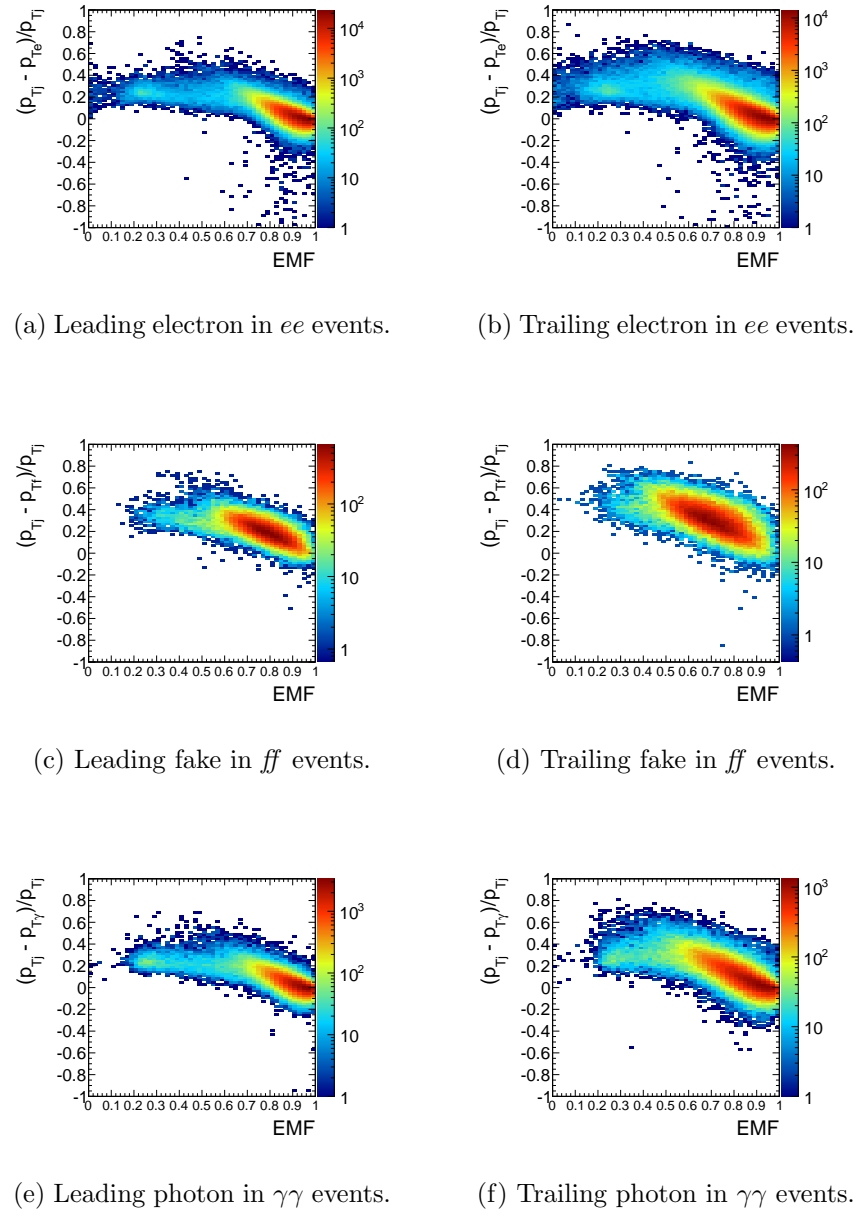


Figure 4.7: Relative difference between the ECAL-only E_T measurement and the PF E_T measurement vs. EMF. PF E_T is defined in the text.

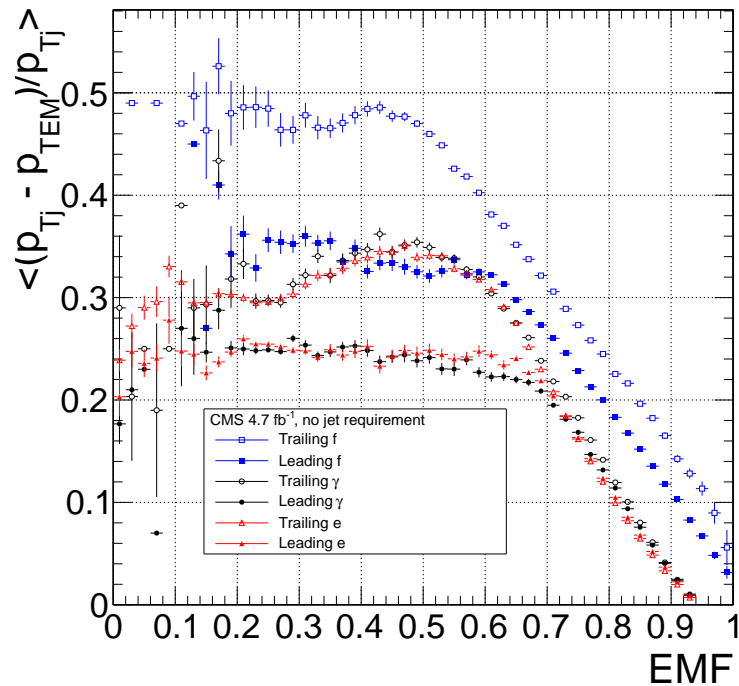


Figure 4.8: Average relative difference between the ECAL-only E_T measurement and the PF E_T measurement vs. EMF for the leading (filled marker) and trailing (open marker) electrons in ee events (red triangles), fakes in ff events (blue squares), and photons in $\gamma\gamma$ events (black circles). These are nothing more than profile histograms of Fig. 4.7. PF E_T is defined in the text. Error bars are statistical only.

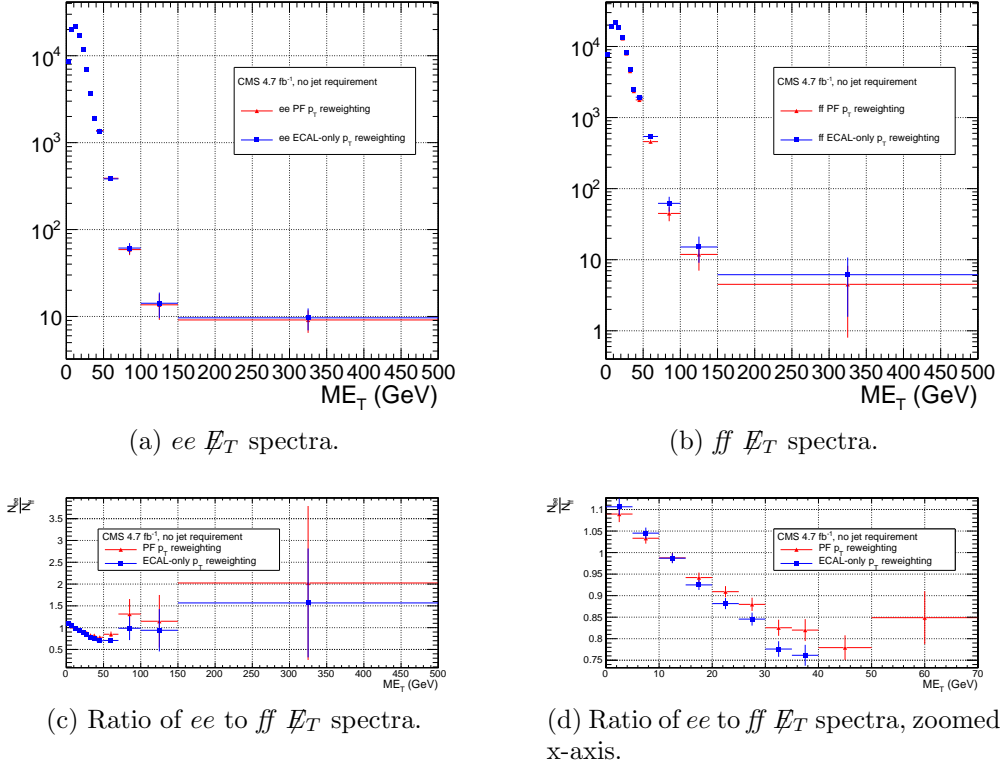


Figure 4.9: E_T spectra of the reweighted ee ($81 \text{ GeV} \leq m_{ee} < 101 \text{ GeV}$) and ff control samples. Blue squares indicate reweighting using the ECAL-only p_T estimate; red triangles indicate reweighting using the PF p_T estimate. The full reweighting and normalization procedure is employed, along with ee sideband subtraction (discussed at the end of this section). Error bars are statistical only.

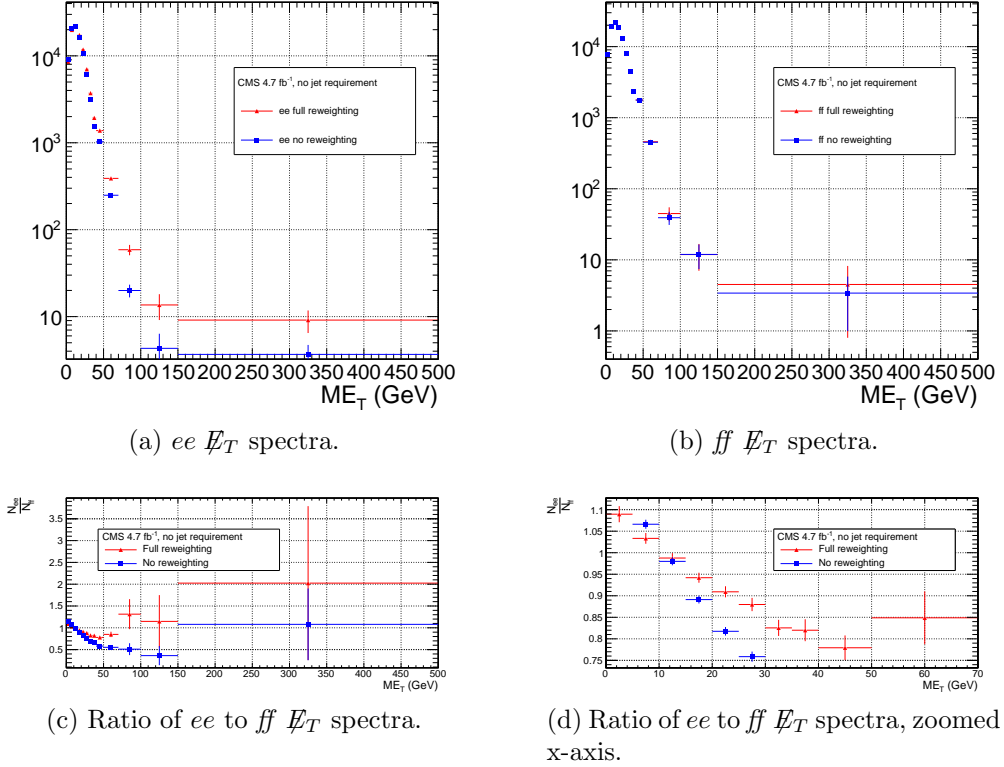


Figure 4.10: E_T spectra of the ee ($81 \text{ GeV} \leq m_{\text{ee}} < 101 \text{ GeV}$) and ff control samples. Red triangles indicate full di-EM $p_T +$ number of jets reweighting; blue squares indicate no reweighting. PF p_T (cf. p. 73) is used to calculate the di-EM p_T . The full normalization procedure is employed, along with ee sideband subtraction (discussed at the end of this section). Error bars are statistical only.

$$w_{ij} = \frac{N_{\text{control}}}{N_{\gamma\gamma}} \frac{N_{\gamma\gamma}^{ij}}{N_{\text{control}}^{ij}} \quad (4.1)$$

where i runs over the number of di-EM p_T bins, j runs over the number of jet bins, N_{control} is the total number of events in the control sample, $N_{\gamma\gamma}$ is the total number of events in the $\gamma\gamma$ sample, $N_{\gamma\gamma}^{ij}$ is the number of $\gamma\gamma$ events in the i^{th} di-EM p_T bin and j^{th} jet bin, and N_{control}^{ij} is the number of control sample events in the i^{th} di-EM p_T bin and j^{th} jet bin. The effect of the reweighting is more significant for the ee sample than for the ff sample, as shown in Figure 4.10.

988 The ee sample contains a non-negligible background of $t\bar{t}$ events in which both
 989 W bosons decay to electrons. These events have significant real \cancel{E}_T from the two
 990 neutrinos (unlike the $\gamma\gamma$ events), and therefore inflate the background estimate at
 991 high \cancel{E}_T . In order to remove the $t\bar{t}$ contribution from the ee sample, a sideband
 992 subtraction method is employed.

993 Only events in the ee sample with $81 \text{ GeV} \leq m_{ee} < 101 \text{ GeV}$, where m_{ee} is the
 994 di-electron invariant mass, are used in the QCD background estimate. This choice
 995 maximizes the ratio of Z signal to background. The sidebands used to estimate the
 996 background contribution within the Z window are defined such that $71 \text{ GeV} \leq m_{ee} <$
 997 81 GeV and $101 \text{ GeV} \leq m_{ee} < 111 \text{ GeV}$.

998 The full reweighting procedure is applied to the Z signal region and the two
 999 sideband regions independently. Only Z signal events are used in the calculation of
 1000 the di-EM p_T weights for the Z signal region, and likewise only the events within
 1001 a given sideband region are used in the calculation of the weights for that region.
 1002 Assuming a constant $t\bar{t}$ background shape, the resulting reweighted sideband \cancel{E}_T
 1003 distributions are added together and subtracted from the reweighted Z signal \cancel{E}_T
 1004 distribution. The sideband subtracted Z signal \cancel{E}_T distribution is then normalized
 1005 as discussed in Secs. 4.1.1 and 4.1.3. The statistical and reweighting error from the
 1006 sideband regions is propagated to the error on the final ee QCD \cancel{E}_T estimate.

1007 The di-EM p_T weights for the two ee sideband regions are shown in Figure 4.11.
 1008 The overall scale of the weights, as well as the trend with di-EM p_T , is similar for
 1009 the two regions (except at high di-EM p_T , where the statistics are poor anyway).
 1010 Figure 4.12 shows the \cancel{E}_T spectra for the two sideband regions and the Z signal
 1011 region after subtraction. The shapes of the spectra indicate that the high- \cancel{E}_T $t\bar{t}$ tail,
 1012 present in the sideband distributions, was successfully subtracted from the Z signal
 1013 distribution.

1014 The ee ($81 \text{ GeV} \leq m_{ee} < 101 \text{ GeV}$), ff , and $\gamma\gamma$ di-EM p_T spectra for events with

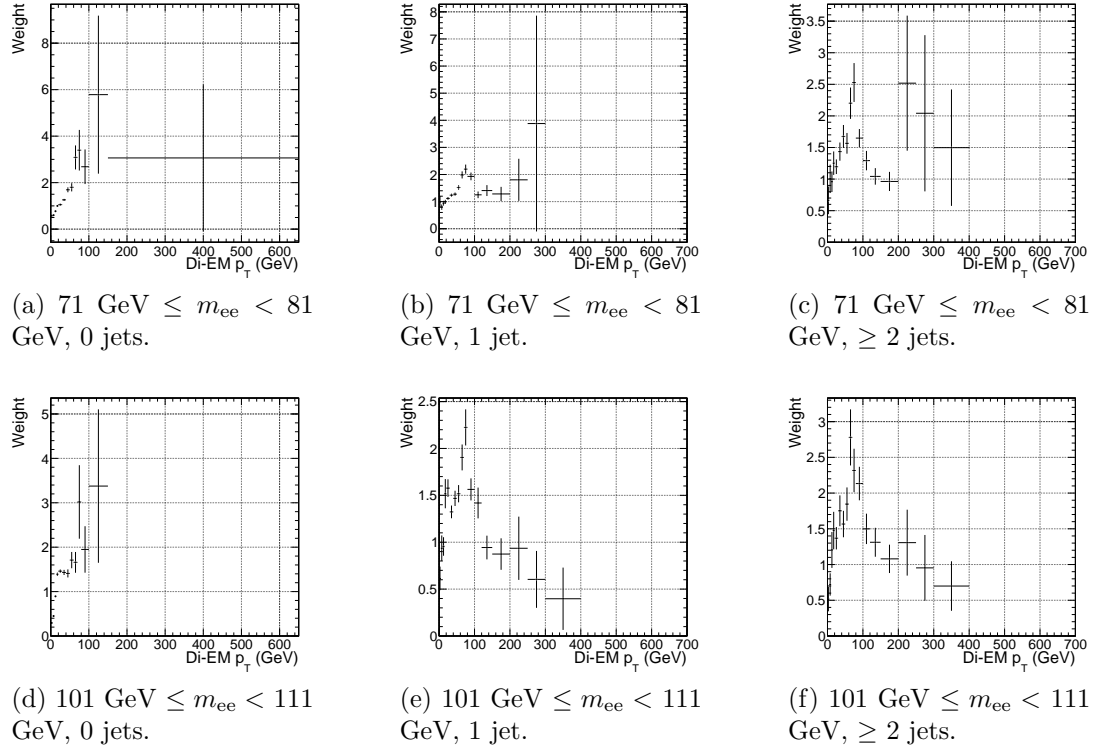


Figure 4.11: ee sideband di-EM p_T weights for events with 0, 1, or ≥ 2 jets (as in Table 3.2). Errors are statistical only.

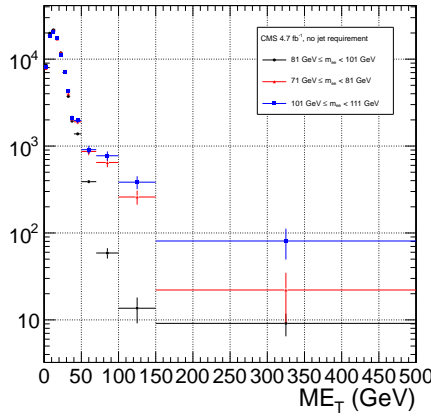


Figure 4.12: E_T spectra of the ee sample for $71 \text{ GeV} \leq m_{ee} < 81 \text{ GeV}$ (red triangles), $81 \text{ GeV} \leq m_{ee} < 101 \text{ GeV}$ (black circles), and $101 \text{ GeV} \leq m_{ee} < 111 \text{ GeV}$ (blue squares). The two sideband distributions (red and blue) and the Z signal distribution (black) are normalized to the total number of $\gamma\gamma$ events. Errors are statistical only.

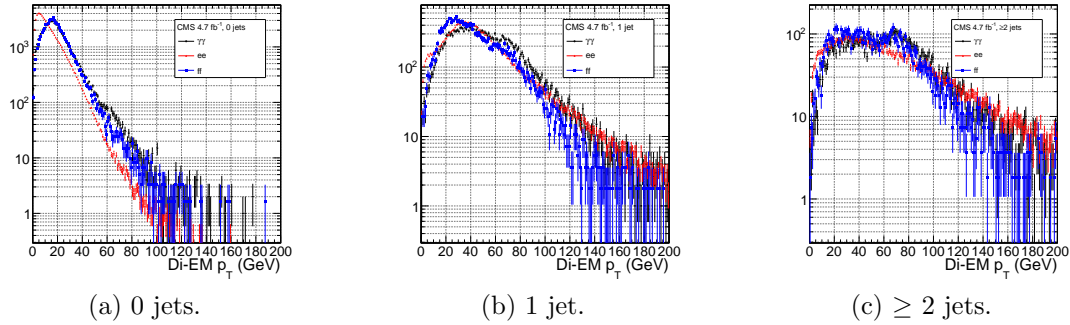


Figure 4.13: ee ($81 \text{ GeV} \leq m_{ee} < 101 \text{ GeV}$) (red triangles), ff (blue squares), and $\gamma\gamma$ (black circles) di-EM p_T spectra for events with 0, 1, or ≥ 2 jets (as in Table 3.2). Errors are statistical only.

1015 0, 1, or ≥ 2 jets (as in Table 3.2) are shown in Figure 4.13. Broad humps in the ff
 1016 and $\gamma\gamma$ spectra are due to kinematic ΔR and p_T turn-ons that are suppressed in the
 1017 ee sample due to the invariant mass cut. Figure 4.14 shows the weights applied to
 1018 the ee ($81 \text{ GeV} \leq m_{ee} < 101 \text{ GeV}$) and ff \cancel{E}_T spectra as a function of di-EM p_T and
 1019 number of jets per event.

1020 4.1.3 Normalization

After reweighting, the \cancel{E}_T distributions of the QCD control samples are normalized to the $\cancel{E}_T < 20$ GeV region of the candidate $\gamma\gamma \cancel{E}_T$ spectrum, where signal contamination is low. The normalization factor is $(N_{\gamma\gamma}^{\cancel{E}_T < 20\text{GeV}} - N_{e\gamma}^{\cancel{E}_T < 20\text{GeV}})/N_{\text{control}}^{\cancel{E}_T < 20\text{GeV}}$, where $N_{e\gamma}^{\cancel{E}_T < 20\text{GeV}}$ is the expected number of electroweak background events with $\cancel{E}_T < 20$ GeV (discussed in Section 4.2).

4.2 Modeling the Electroweak Background

¹⁰²⁷ $W\gamma$, $W + \text{jet}$, and $t\bar{t}$ processes in which the W decay electron is misidentified as a
¹⁰²⁸ photon (due to a failure to properly associate a pixel seed to the electron candidate)
¹⁰²⁹ can contribute significantly to the high- \cancel{E}_T tail of the $\gamma\gamma$ \cancel{E}_T spectrum. To estimate

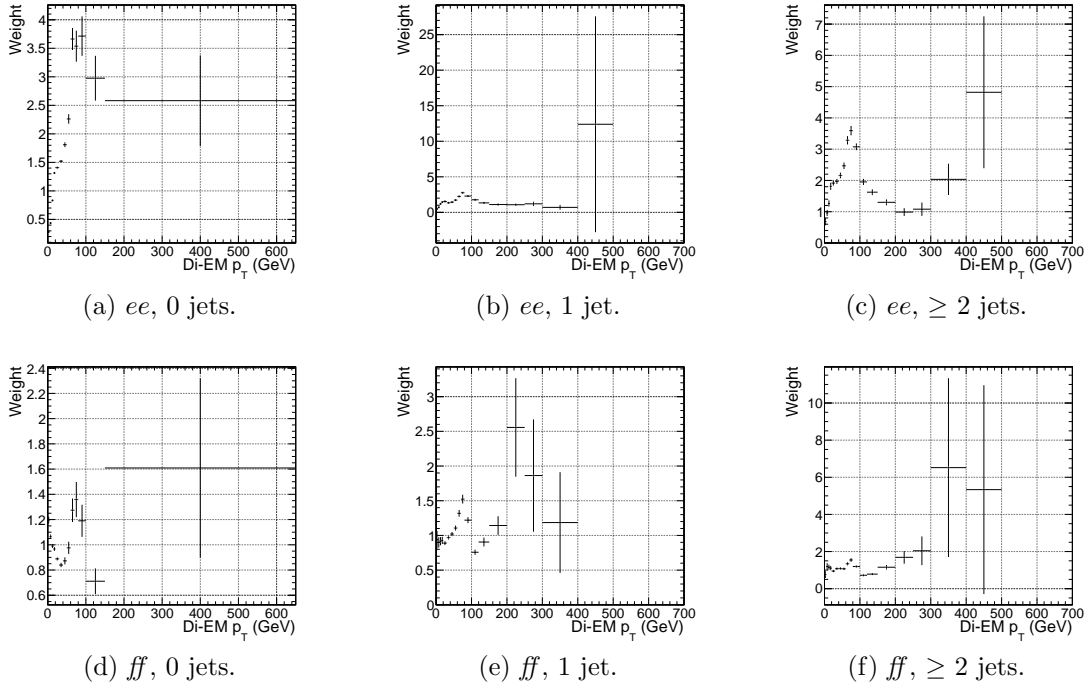


Figure 4.14: ee ($81 \text{ GeV} \leq m_{ee} < 101 \text{ GeV}$) and ff di-EM p_T weights for events with 0, 1, or ≥ 2 jets (as in Table 3.2). Errors are statistical only.

1030 this background, the $e\gamma$ sample, which is enriched in $W \rightarrow e\nu$ decays, is scaled by
 1031 $f_{e \rightarrow \gamma}/(1 - f_{e \rightarrow \gamma})$, where $f_{e \rightarrow \gamma}$ is the rate at which electrons are misidentified as photons.
 1032 The derivation of this scaling factor comes from the two equations

$$N_{e\gamma}^W = f_{e \rightarrow e} N_W \quad (4.2)$$

$$N_{\gamma\gamma}^W = (1 - f_{e \rightarrow e}) N_W \quad (4.3)$$

1033 where $N_{e\gamma}^W$ is the number of W events in the $e\gamma$ sample in which the electron was
 1034 correctly identified, $f_{e \rightarrow e}$ is the probability to correctly identify an electron, N_W is
 1035 the true number of triggered $W \rightarrow e\nu$ events, and $N_{\gamma\gamma}^W$ is the number of W events in
 1036 the $\gamma\gamma$ sample in which the electron was misidentified as a photon. The contribution
 1037 from $Z \rightarrow ee$ can be neglected (i.e. $f_{e \rightarrow \gamma}$ is small and the Z contribution involves
 1038 $f_{e \rightarrow \gamma}^2$, since both electrons have to be misidentified). Since $f_{e \rightarrow e} = 1 - f_{e \rightarrow \gamma}$, solving

1039 for $N_{\gamma\gamma}^W$ gives

$$N_{\gamma\gamma}^W = \frac{f_{e\rightarrow\gamma}}{1 - f_{e\rightarrow\gamma}} N_{e\gamma}^W \quad (4.4)$$

1040 $f_{e\rightarrow\gamma}$ is measured by fitting the Z peaks in the ee and $e\gamma$ samples. The number of
1041 Z events fitted in the ee and $e\gamma$ samples, respectively, is given by

$$N_{ee}^Z = (1 - f_{e\rightarrow\gamma})^2 N_Z \quad (4.5)$$

$$N_{e\gamma}^Z = 2f_{e\rightarrow\gamma}(1 - f_{e\rightarrow\gamma}) N_Z \quad (4.6)$$

1042 where N_Z is the true number of triggered $Z \rightarrow ee$ events. Solving for $f_{e\rightarrow\gamma}$ gives

$$f_{e\rightarrow\gamma} = \frac{N_{e\gamma}^Z}{2N_{ee}^Z + N_{e\gamma}^Z} \quad (4.7)$$

1043 A Crystal Ball function is used to model the Z signal shape in both the ee and
1044 $e\gamma$ samples, while an exponential convoluted with an error function (`RooCMSShape`,
1045 see Sec. 3.4.1) is used to model the background shape. The fixed fit parameters are
1046 identical for the two samples, but the other parameters are allowed to float indepen-
1047 dently. Table 4.3 shows the values and ranges of the fixed and floating fit parameters,
1048 respectively.

1049 Fits to the ee and $e\gamma$ invariant mass spectra are shown in Figure 4.15. Figure 4.16
1050 indicates that the dependence of $f_{e\rightarrow\gamma}$ on the electron p_T and η is small. (Note that all
1051 fit parameters are floating in the p_T -dependent fits.) Therefore, a constant misidenti-
1052 fication rate (derived from all ee and $e\gamma$ events), rather than a p_T - and η -dependent
1053 misidentification rate, is used in the final electroweak background estimate, with the

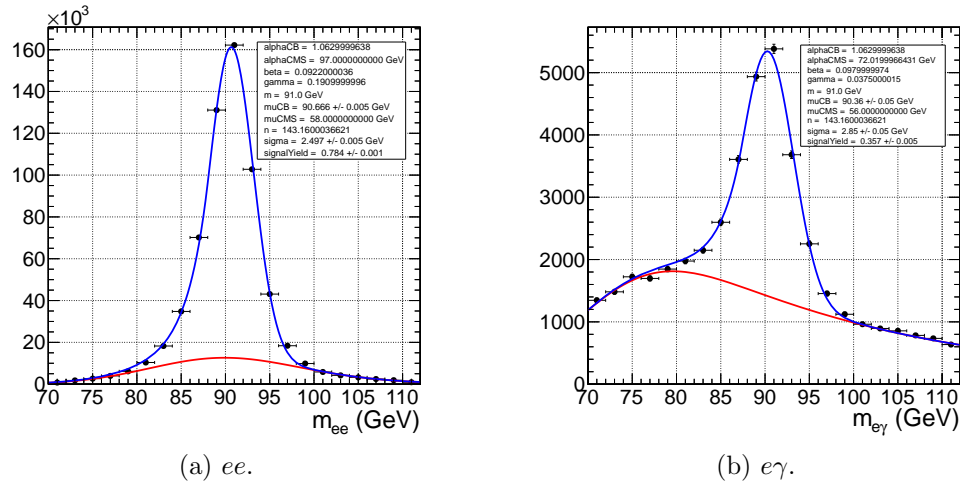


Figure 4.15: Fits to the ee and $e\gamma$ invariant mass spectra using the Crystal Ball RooCMSShape function described in the text and in Table 4.3. The total fit is shown in blue, while the background component is shown in red.

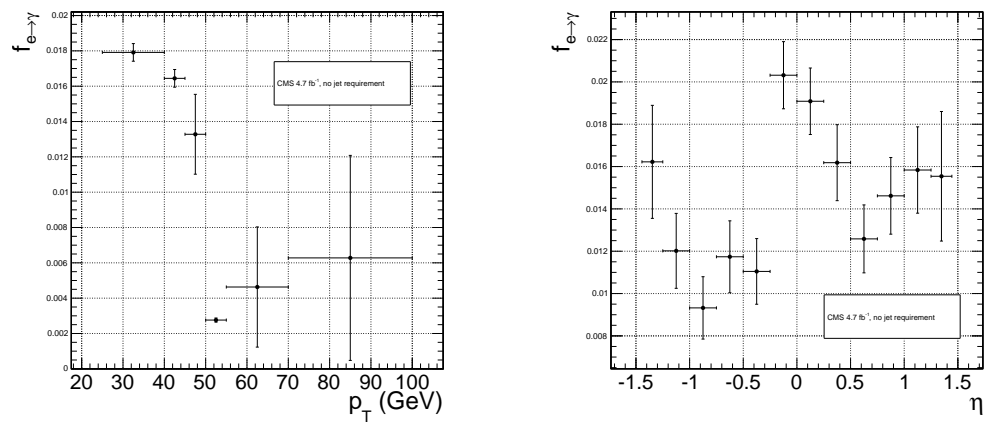
difference between the constant rate and the rate for electrons with p_T between 25 and 40 GeV (the range in which the bulk of the trailing photons in the $\gamma\gamma$ sample lie) taken as a systematic error.

Using the integrals of the Z fits shown in Fig. 4.15, Eq. 4.7, and the p_T systematic discussed above, $f_{e \rightarrow \gamma}$ is calculated to be $0.014 \pm 0.000(\text{stat.}) \pm 0.004(\text{syst.})$. The scaled $e\gamma$ MET distribution is shown in Figure 4.17.

In the 36 pb^{-1} version of this analysis [64], it was shown that the ee sample could
 accurately predict the QCD and real Z contribution to the $e\gamma$ sample at low \cancel{E}_T , and
 that the expectation from $W \rightarrow e\nu$ MC accounted for the remaining W contribution
 at high \cancel{E}_T . A plot of the \cancel{E}_T distributions of the 2010 $e\gamma$ sample and the predicted
 components is shown in Figure 4.18. This exercise helps to validate both the QCD
 and electroweak background prediction methods.

Table 4.3: Parameter values for the signal and background PDFs for the ee and $e\gamma$ samples. When a bracketed range is given, the parameter is allowed to float within that range. When a constant is given, the parameter is fixed to that constant.

PDF	Crystal Ball fit parameters				RooCMSShape fit parameters			
	μ	σ	α	n	μ	α	β	γ
ee signal	[86.2, 96.2]	[1.0, 5.0]	1.063	143.16	N/A	N/A	N/A	N/A
$e\gamma$ signal	[86.2, 96.2]	[1.0, 5.0]	1.063	143.16	N/A	N/A	N/A	N/A
ee background	N/A	N/A	N/A	N/A	58	97.0	0.0922	0.191
$e\gamma$ background	N/A	N/A	N/A	N/A	56	72.02	0.098	0.0375



(a) $f_{e \rightarrow \gamma}$ vs. electron p_T . For the lowest p_T bin, the fit to the $e\gamma$ spectrum does not converge well, so the Z signal fraction is fixed to the value in Fig. 4.15b.

(b) $f_{e \rightarrow \gamma}$ vs. electron η .

Figure 4.16: $f_{e \rightarrow \gamma}$ vs. electron p_T and η .

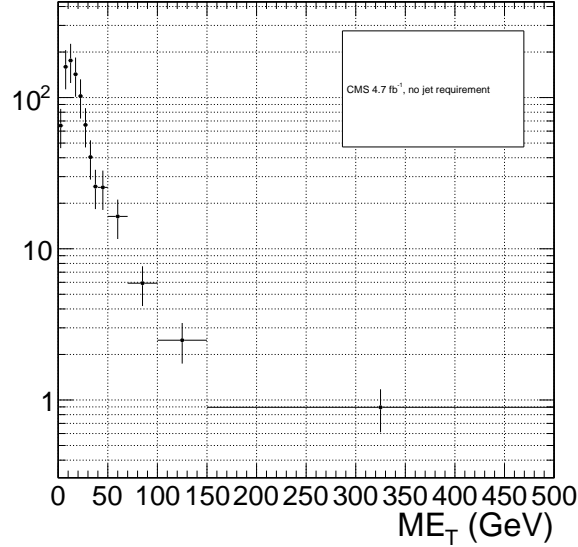


Figure 4.17: E_T spectrum of the $e\gamma$ sample after scaling by $f_{e \rightarrow \gamma}$. The total error on $f_{e \rightarrow \gamma}$ is propagated to the total error on the electroweak background estimate.

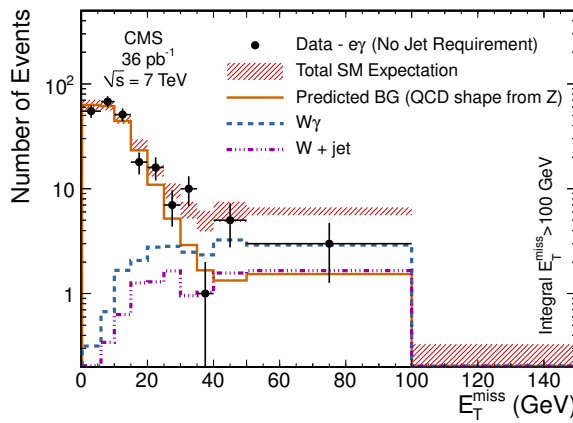


Figure 4.18: E_T spectrum of the $e\gamma$ sample in 36 pb^{-1} of 2010 LHC data scaled by the 2010 measured $f_{e \rightarrow \gamma}$ (black dots), QCD and real Z predicted background from the 2010 ee sample (solid orange line), MC $W + \text{jet}$ estimate (dash-dotted purple line), and MC $W\gamma$ estimate (dashed blue line). The total $e\gamma$ prediction (red band) is the sum of the ee , $W + \text{jet}$, and $W\gamma$ predictions. Reprinted from Fig. 2 of ref. [64].

1066 4.3 Errors on the Background Prediction

1067 The statistical error on the final background estimate in a particular \cancel{E}_T bin comes
 1068 from three sources: the number of control sample events collected in that bin, the
 1069 statistical error on the weights applied to events in that bin, and the statistics of the
 1070 normalization region. In the case of the ee control sample, there are contributions
 1071 from the statistics of the m_{ee} sidebands as well.

1072 In order to estimate the statistical error due to the reweighting procedure, 1000
 1073 toy sets of weights are generated. Each set includes a weight for each (di-EM p_T , N_j)
 1074 bin, with the values picked from a Gaussian distribution with mean and standard
 1075 deviation equal to the observed weight for that bin and its statistical error. The effect
 1076 of reweighting error is not correlated between \cancel{E}_T bins. For each of the 1000 exper-
 1077 iments, the control sample data are reweighted according to the generated weights,
 1078 and the background estimates are calculated for each \cancel{E}_T bin. Since the distribution
 1079 of the toy background estimates follows a Gaussian distribution in each \cancel{E}_T bin, the
 1080 RMS spread of the estimates is taken as the statistical error due to reweighting. This
 1081 procedure is carried out for the ff , ee , low sideband ee , and high sideband ee samples.

1082 The total statistical error on the background estimate per \cancel{E}_T bin is given by

$$\sigma_{\text{stat}}^2 = \sigma_{\text{stat,QCD}}^2 + \sigma_{\text{stat,EW}}^2 \quad (4.8)$$

1083 where $\sigma_{\text{stat,QCD}}^2$ is the square of the total statistical error on the QCD prediction in
 1084 the \cancel{E}_T bin

$$\sigma_{\text{stat,QCD}}^2 = \sigma_{\text{stat},s}^2 + \sigma_{\text{Poisson,QCD}}^2 + \sigma_{\text{reweight},s}^2 + \sigma_{\text{reweight,QCD}}^2 \quad (4.9)$$

1085 and $\sigma_{\text{stat,EW}}$ is the Poisson error on the number of $e\gamma$ events in the \cancel{E}_T bin ($= \sqrt{N_{e\gamma}}$,
 1086 where $N_{e\gamma}$ is the prediction in the \cancel{E}_T bin after scaling by $f_{e\rightarrow\gamma}$). The contributions
 1087 to $\sigma_{\text{stat,QCD}}^2$ are discussed below.

- 1088 • $\sigma_{\text{stat},s}^2$ is the statistical error contributed by the normalization factor s (i.e. from
 1089 Poisson error in the normalization region $\cancel{E}_T < 20$ GeV):

$$\begin{aligned}\sigma_{\text{stat},s}^2 = & \frac{N_{\text{control}}^2}{(N_{\gamma\gamma}^{\text{norm}} - N_{e\gamma}^{\text{norm}})^2} ([\sigma_{\text{Poisson},\gamma\gamma}^{\text{norm}}]^2 + [\sigma_{\text{Poisson},e\gamma}^{\text{norm}}]^2) + \\ & \frac{N_{\text{control}}^2}{(N_{\text{control}}^{\text{norm}})^2} (\sigma_{\text{Poisson,control}}^{\text{norm}})^2\end{aligned}\quad (4.10)$$

1090 where N_{control} is the number of reweighted, normalized events in the \cancel{E}_T bin,
 1091 $N_{\gamma\gamma}^{\text{norm}}$ is the number of $\gamma\gamma$ events in the normalization region, $N_{e\gamma}^{\text{norm}}$ is the num-
 1092 ber of $e\gamma$ events in the normalization region (after scaling by $f_{e\rightarrow\gamma}$), $\sigma_{\text{Poisson},\gamma\gamma}^{\text{norm}}$
 1093 is the Poisson error on the number of $\gamma\gamma$ events in the normalization region
 1094 ($= \sqrt{N_{\gamma\gamma}^{\text{norm}}}$), $\sigma_{\text{Poisson},e\gamma}^{\text{norm}}$ is the Poisson error on the number of $e\gamma$ events in the
 1095 normalization region ($= \sqrt{N_{e\gamma}^{\text{norm}}}$), $N_{\text{control}}^{\text{norm}}$ is the number of QCD control (ee
 1096 or ff) events in the normalization region, and $\sigma_{\text{Poisson,control}}^{\text{norm}}$ is the Poisson error
 1097 on the number of QCD control (ee or ff) events in the normalization region
 1098 ($= \sqrt{\sum_{i=1}^{N_{\text{control}}^{\text{norm}}} w_i^2}$, where w_i is the di-EM p_T weight applied to event i). For
 1099 the ee control region, N_{control} and $N_{\text{control},\text{norm}}$ are sideband subtracted, and
 1100 $\sigma_{\text{Poisson,control}}^{\text{norm}}$ includes the Poisson error on the number of sideband events.

- 1101 • $\sigma_{\text{Poisson,QCD}}$ is the Poisson error due to the number of QCD control (ee or ff)
 1102 events in the \cancel{E}_T bin, equal to $\sqrt{\sum_{i=1}^{N_{\text{control}}^{\text{norm}}} w_i^2}$, where w_i is the di-EM p_T weight
 1103 applied to event i . For the ee control region, $\sigma_{\text{Poisson,QCD}}$ includes the Poisson
 1104 error on the number of subtracted sideband events.
- 1105 • $\sigma_{\text{reweight},s}$ is the error contributed by the control sample reweighting in the nor-

1106 malization region ($= \frac{N_{\text{control}}^2}{(N_{\text{control}}^{\text{norm}})^2} \sigma_{\text{reweight,control}}^{\text{norm}}$). $\sigma_{\text{reweight,control}}^{\text{norm}}$ is the quadrature
 1107 sum of the RMS of the 1000 toy reweighting experiments for each \cancel{E}_T bin in the
 1108 normalization region. For the ee control sample, it also includes (in quadrature)
 1109 the RMS of the toys in the sideband samples.

- 1110 • $\sigma_{\text{reweight,QCD}}$ is the error contributed by the control sample reweighting in the \cancel{E}_T
 1111 bin ($= s\sigma_{\text{reweight,control}}$). $\sigma_{\text{reweight,control}}$ is the RMS of the 1000 toy reweighting
 1112 experiments for the E_T bin. For the ee control sample, it also includes (in
 1113 quadrature) the RMS of the toys in the sideband samples.

1114 The dominant source of systematic error on the background estimate is the slight
 1115 difference in hadronic activity between the ee , ff , and $\gamma\gamma$ samples. This results in a
 1116 small bias (~ 1 GeV) of the ee \cancel{E}_T distribution towards lower values with respect to
 1117 the ff and $\gamma\gamma$ samples, as shown in Figure 4.19. Therefore, the ff sample is used as
 1118 the primary QCD background estimator, and the difference between the ee and ff
 1119 predictions is assigned as an error on the knowledge of the hadronic activity. For \cancel{E}_T
 1120 > 100 GeV, this error amounts to 43% of the total QCD + electroweak background
 1121 estimate.

1122 The second largest source of systematic error comes from the p_T dependence of the
 1123 $e \rightarrow \gamma$ misidentification rate (see 4.2). For $\cancel{E}_T > 100$ GeV, the expected electroweak
 1124 background is 3.4 ± 1.0 events, so this error amounts to 4.8% of the total QCD +
 1125 electroweak background estimate.

1126 Finally, the assumption of a constant $t\bar{t}$ and $W + \text{jets}$ background shape under
 1127 the Z peak in the ee sample induces a systematic error on the ee sideband-subtracted
 1128 background prediction. To assess the magnitude of this error, the sideband subtraction
 1129 (see Sec. 4.1.2) is performed once using only the prediction from the high sideband,
 1130 and once using only the prediction from the low sideband. In each of these cases, the
 1131 prediction is weighted by a factor of two, to account for the fact that the sideband
 1132 regions are only half as wide (10 GeV) as the signal region (20 GeV). The maximum

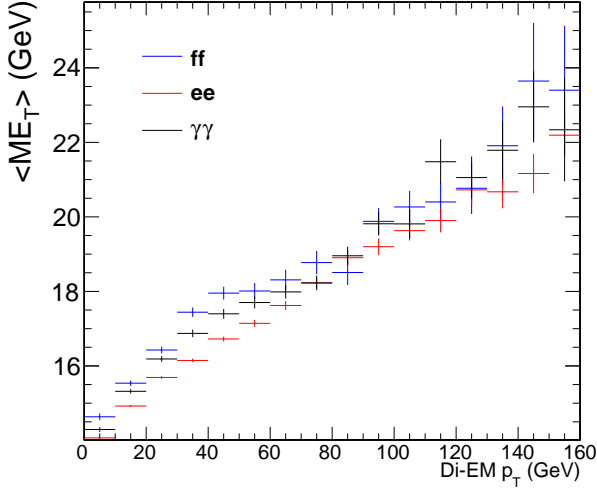


Figure 4.19: Average \cancel{E}_T vs. di-EM p_T for the ff (blue), ee (red), and $\gamma\gamma$ (black) samples.

1133 variation from the nominal ee estimate is taken as the error, which amounts to 11%
 1134 for $\cancel{E}_T > 100$ GeV. \cancel{E}_T distributions using the nominal ee sideband subtraction, the
 1135 low-sideband-only subtraction, and the high-sideband-only subtraction are shown in
 1136 Figure 4.20.

1137 The uncertainty in how to define the (di-EM p_T , N_j) bins, especially at high di-
 1138 EM p_T where the statistics are low, is covered by the 1000-toys procedure as long as
 1139 the bins are not too coarse. This is shown in Figure 4.21. If the bins are too coarse,
 1140 the details of the shape of the di-EM p_T spectra are lost, and the reweighting has a
 1141 smaller effect.

1142 The use of uncorrected instead of corrected PF \cancel{E}_T (see Sec. 3.1.3) makes no
 1143 difference in the agreement of the background predictions and the search sample in
 1144 a control region at low \cancel{E}_T , as shown in Figure 4.22. Since the control samples are
 1145 derived from the same data as the search sample, any biases in the \cancel{E}_T reconstruction
 1146 due to jet energy scale are present equally in both samples.

1147 Tables 4.4 and 4.5 list all the errors on the ee and ff QCD background predictions,
 1148 respectively, for the \cancel{E}_T bins used in the search. Table 4.6 lists the errors on the

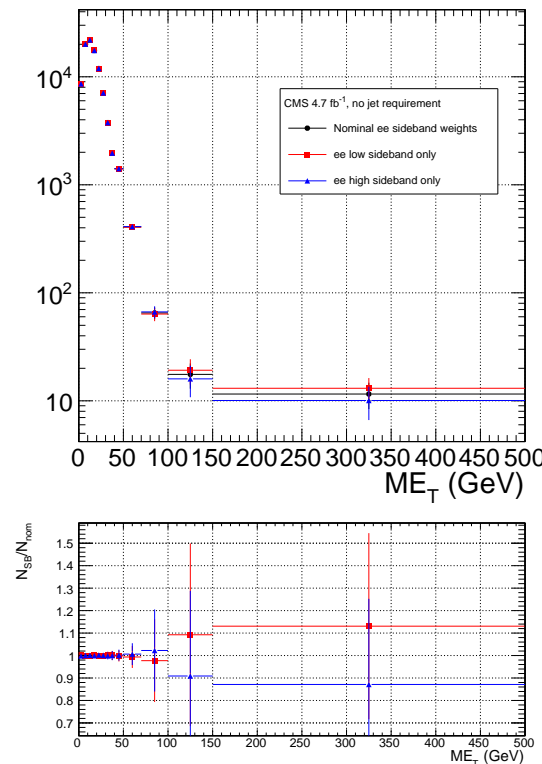


Figure 4.20: ee E_T distributions using the nominal sideband subtraction (black circles), low sideband only (red squares), and high sideband only (blue triangles). The bottom plot shows the ratio of the low sideband distribution to the nominal (red squares) and the ratio of the high sideband distribution to the nominal (blue triangles).

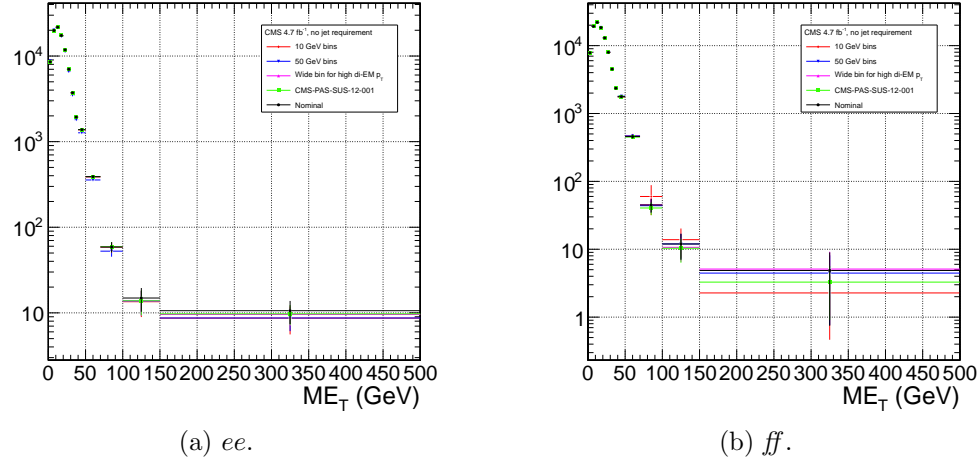


Figure 4.21: Comparison of E_T distributions for five different di-EM p_T bin definitions: uniform bins of width 10 GeV (red diamonds); uniform bins of width 50 GeV (blue downward-pointing triangles); bins with lower edges $\{0.0, 5.0, 10.0, 15.0, 20.0, 30.0, 40.0, 50.0, 60.0, 70.0, 80.0, 100.0, 750.0\}$ GeV for 0-jet events and $\{0.0, 5.0, 10.0, 15.0, 20.0, 30.0, 40.0, 50.0, 60.0, 70.0, 80.0, 100.0, 150.0\}$ GeV for ≥ 1 -jet events (magenta upward-pointing triangles), i.e. a single wide bin at high di-EM p_T ; bins with lower edges $\{0.0, 5.0, 10.0, 15.0, 20.0, 30.0, 40.0, 50.0, 60.0, 70.0, 80.0, 100.0, 150.0\}$ GeV for 0-jet events and $\{0.0, 5.0, 10.0, 15.0, 20.0, 30.0, 40.0, 50.0, 60.0, 70.0, 80.0, 100.0, 120.0, 150.0, 200.0, 700.0\}$ GeV for ≥ 1 -jet events (green squares), i.e. the bins used in ref. [19]; and the nominal bin definitions shown in Fig. 4.14 (black circles).

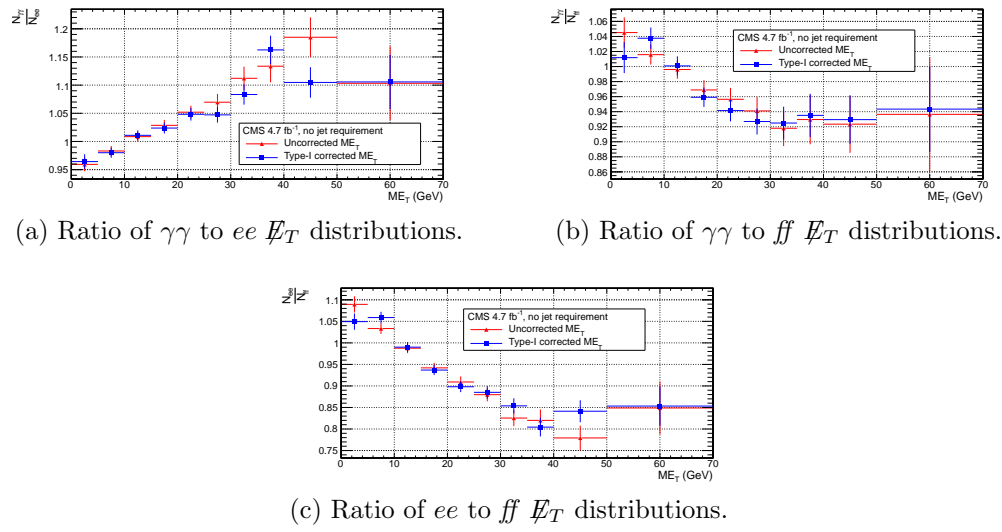


Figure 4.22: Agreement between $\gamma\gamma$, ee , and ff samples for uncorrected (red triangles) and corrected (blue squares) E_T .

1149 electroweak background prediction. Finally, Table 4.7 shows the errors on the total
1150 QCD + electroweak background prediction, broken down by origin (statistical or
1151 systematic) and QCD background estimation sample (ee or ff). In the final result,
1152 only the ff QCD estimate is used.

Table 4.4: Errors on the ee QCD background prediction as a fraction of the ee prediction.

Source of error	Fractional uncertainty (%)				
	[50, 60)	[60, 70)	[70, 80)	[80, 100)	≥ 100
Total	3.9	8.1	16	25	25
Statistics	3.6	7.8	16	24	22
No. events	3.6	7.7	15	24	20
In norm. region	0.43	0.44	0.46	0.55	0.51
In this E_T bin	3.5	7.7	15	24	20
Reweighting	0.73	1.2	3.5	4.3	7.7
In norm. region	0.19	0.19	0.2	0.24	0.23
In this E_T bin	0.71	1.2	3.5	4.3	7.7
Systematics	1.4	2	0.72	5.5	12
$f_{e \rightarrow \gamma}$ (in norm. region)	0.0012	0.0012	0.0013	0.0015	0.0014
m_{ee} background shape	1.4	2	0.72	5.5	12

Table 4.5: Errors on the ff QCD background prediction as a fraction of the ff prediction.

Source of error	Fractional uncertainty (%)				
	[50, 60)	[60, 70)	[70, 80)	[80, 100)	≥ 100
Total	15	25	61	34	64
Statistics	7.2	14	30	33	38
No. events	7.1	14	29	33	36
In norm. region	0.64	0.64	0.64	0.64	0.64
In this E_T bin	7.1	14	29	33	36
Reweighting	0.85	2.7	5.1	6.9	13
In norm. region	0.27	0.27	0.27	0.27	0.27
In this E_T bin	0.81	2.6	5.1	6.9	13
Systematics	13	21	53	5.5	52
ee/ff difference	13	21	53	5.5	52
$f_{e \rightarrow \gamma}$ (in norm. region)	0.0012	0.0012	0.0012	0.0012	0.0012

Table 4.6: Errors on the $e\gamma$ electroweak background prediction as a fraction of the $e\gamma$ prediction.

Source of error	Fractional uncertainty (%)				
	[50, 60)	[60, 70)	[70, 80)	[80, 100)	≥ 100
Total	29	29	30	30	30
Statistics	3.6	5.2	6.7	7.2	6.5
Systematics ($f_{e \rightarrow \gamma}$)	29	29	29	29	29

Table 4.7: Errors on the total QCD + electroweak background prediction as a fraction of the total prediction.

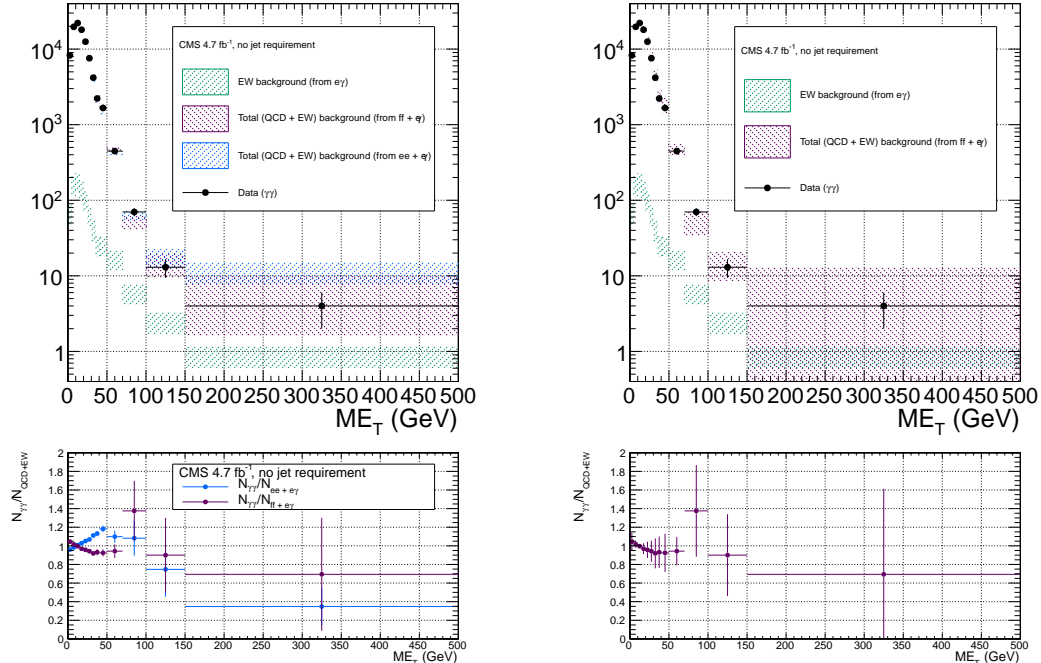
Source of error	Fractional uncertainty (%)				
	[50, 60)	[60, 70)	[70, 80)	[80, 100)	≥ 100
Total ($ee + e\gamma$)	3.9	7.8	15	22	22
Statistics	3.4	7.3	14	21	18
QCD	3.4	7.3	14	21	18
Electroweak	0.13	0.3	0.53	0.79	0.76
Systematics	1.7	2.5	2.4	5.8	11
QCD	1.4	1.9	0.66	4.9	11
Electroweak	1	1.7	2.3	3.2	3.4
Total ($ff + e\gamma$)	14	24	54	30	54
Statistics	6.9	13	26	29	30
QCD	6.9	13	26	29	30
Electroweak	0.11	0.24	0.79	0.83	1.1
Systematics	12	20	47	5.9	43
QCD	12	20	47	4.9	43
Electroweak	0.9	1.3	3.4	3.4	4.8

1153 4.4 Results

1154 Figure 4.23(4.24) shows the \cancel{E}_T distribution of the inclusive(≥ 1 -jet) $\gamma\gamma$ search sample
 1155 along with the predicted \cancel{E}_T distributions of the QCD and electroweak backgrounds.
 1156 The observed number of two-photon events, background estimates and their errors,
 1157 and expected number of inclusive(≥ 1 -jet) two-photon events from two representative
 1158 GGM SUSY models are listed in Table 4.8(4.9). (Details of the SUSY MC production
 1159 are given in Chapter 5 and App. A.) No deviation from the Standard Model prediction
 1160 is observed in the $\gamma\gamma$ search sample.

Table 4.8: Observed numbers of two-photon events, background estimates and their errors, and expected numbers of two-photon events from two representative GGM SUSY models (details of MC simulation given in Chapter 5 and App. A) for the \cancel{E}_T bins used in the search. Errors on the background estimates are detailed in Tables 4.4, 4.5, 4.6, and 4.7. Errors on the expected numbers of GGM events are purely statistical.

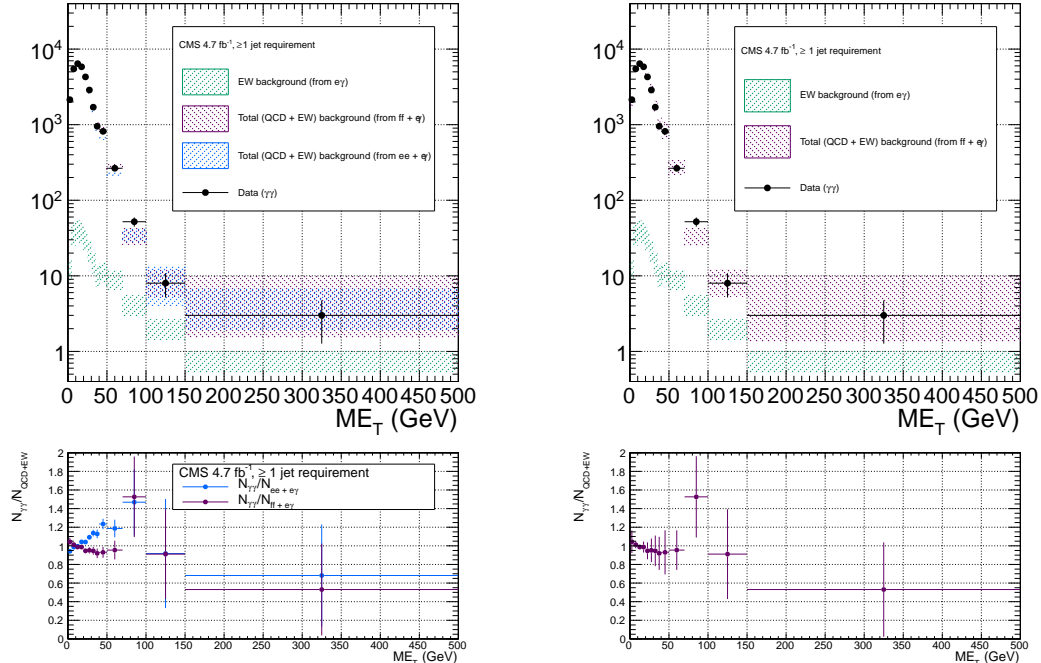
Source	No. events				
	[50, 60)	[60, 70)	[70, 80)	[80, 100)	≥ 100
Data observed ($\gamma\gamma$)	354	93	37	33	17
Background predicted ($ff + e\gamma$)	361 ± 51.5	113 ± 27.1	26.9 ± 14.5	23.9 ± 7.23	20.2 ± 10.9
GGM1 expected (fill in)					
GGM2 expected (fill in)					



(a) $ee + e\gamma$ and $ff + e\gamma$. The widths of the bands correspond to the errors given in Table 4.7, excluding the error associated with the difference between the ee and ff QCD estimates for the $ff + e\gamma$ E_T distribution.

(b) $ff + e\gamma$. The widths of the bands correspond to the errors given in Table 4.7, including the error associated with the difference between the ee and ff QCD estimates.

Figure 4.23: \not{E}_T distribution of the $\gamma\gamma$ search sample (black circles) along with the predicted \not{E}_T distributions of the QCD and electroweak backgrounds (blue band for ee QCD prediction + electroweak prediction, purple band for ff QCD prediction + electroweak prediction). The electroweak background prediction is shown in green. The bottom plots show the ratio of the $\gamma\gamma$ \not{E}_T distribution to the $ee + e\gamma$ background distribution (blue) and $ff + e\gamma$ background distribution (purple).



(a) $ee + e\gamma$ and $ff + e\gamma$. The widths of the bands correspond to the errors given in Table 4.7, excluding the error associated with the difference between the ee and ff QCD estimates for the $ff + e\gamma$ E_T distribution.

(b) $ff + e\gamma$. The widths of the bands correspond to the errors given in Table 4.7, including the error associated with the difference between the ee and ff QCD estimates.

Figure 4.24: E_T distribution of the $\gamma\gamma + \geq 1$ jet search sample (black circles) along with the predicted E_T distributions of the QCD and electroweak backgrounds (blue band for ee QCD prediction + electroweak prediction, purple band for ff QCD prediction + electroweak prediction). The electroweak background prediction is shown in green. The bottom plots show the ratio of the $\gamma\gamma E_T$ distribution to the $ee + e\gamma$ background distribution (blue) and $ff + e\gamma$ background distribution (purple).

Table 4.9: Observed numbers of two-photon + ≥ 1 -jet events, background estimates and their errors, and expected numbers of two-photon + ≥ 1 -jet events from two representative GGM SUSY models (details of MC simulation given in Chapter 5 and App. A) for the \cancel{E}_T bins used in the search. Errors on the background estimates are detailed in Tables 4.4, 4.5, 4.6, and 4.7. Errors on the expected numbers of GGM events are purely statistical.

Source	No. events				
	[50, 60)	[60, 70)	[70, 80)	[80, 100)	≥ 100
Data observed ($\gamma\gamma + \geq 1$ jet)	202	63	27	25	11
Background predicted ($ff + e\gamma$)	200 ± 35.4	77.7 ± 28.1	19.4 ± 8.55	14.7 ± 7.04	14.4 ± 5.59
GGM1 expected (fill in)					
GGM2 expected (fill in)					

1161 **Chapter 5**

1162 **Interpretation of Results in Terms
1163 of GMSB Models**

1164 As shown in Figs. 4.23 and 4.24 and Tables 4.8 and 4.9, no excess of events above
1165 the Standard Model expectation is found in either the ≥ 0 - or ≥ 1 -jet analyses for
1166 the GMSB-sensitive region $\cancel{E}_T \geq 50$ GeV. Therefore, upper limits on the production
1167 cross sections $\times \mathcal{BR}(\tilde{\chi}_1^0 \rightarrow \gamma \tilde{G})^2$ of various GMSB models are calculated and then
1168 translated into statements of exclusion. Section 5.1 describes the GMSB models that
1169 were generated with MC and tested for exclusion. The upper limit calculation is laid
1170 out in Section 5.2, and the translation to model exclusions is described in Section 5.3.
1171 The upper limits themselves are presented in Section 5.4, and, finally, the exclusions
1172 are presented in Section 5.5.

1173 **5.1 Simplified Models**

1174 **5.2 Upper Limit Calculation**

1175 The upper limits are calculated according to the prescription followed for the 2011
1176 ATLAS + CMS Higgs limit combination [65]. This prescription utilizes the frequentist

1177 CL_s method [66] with profile likelihood test statistic [67]. The CL_s method and the
1178 profile likelihood are explained in Section 5.2.2, using specific signal MC points to
1179 illustrate the procedure. First, however, the signal MC acceptance \times efficiency, which
1180 is an input to the limit setting procedure, is presented in Section 5.2.1.

1181 **5.2.1 Signal Acceptance \times Efficiency**

1182 **5.2.2 CL_s and the Profile Likelihood Test Statistic**

1183 **5.3 Translation of Upper Limits to Model Exclu-
1184 sions**

1185 **5.4 Cross Section Upper Limits**

1186 **5.5 Exclusion Contours**

¹¹⁸⁷ **Appendix A**

¹¹⁸⁸ **Monte Carlo Samples**

¹¹⁸⁹ A number of MC samples are utilized in this analysis and referred to throughout the
¹¹⁹⁰ text. Below is a list of the MC samples used and an explanation of what the sample
¹¹⁹¹ names mean.

¹¹⁹² **A.0.1 List of Samples**

¹¹⁹³ 1. Drell-Yan:

¹¹⁹⁴ /DYJetsToLL_TuneZ2_M-50_7TeV-madgraph-tauola/
¹¹⁹⁵ Fall11-PU_S6_START42_V14B-v1/AODSIM

¹¹⁹⁶ 2. QCD enriched with B and D meson decays to electrons:

¹¹⁹⁷ /QCD_Pt-20to30_BCToE_TuneZ2_7TeV-pythia6/
¹¹⁹⁸ Fall11-PU_S6_START42_V14B-v1/AODSIM,
¹¹⁹⁹ /QCD_Pt-30to80_BCToE_TuneZ2_7TeV-pythia6/
¹²⁰⁰ Fall11-PU_S6_START42_V14B-v1/AODSIM,
¹²⁰¹ /QCD_Pt-80to170_BCToE_TuneZ2_7TeV-pythia6/
¹²⁰² Fall11-PU_S6_START42_V14B-v1/AODSIM

¹²⁰³ 3. Photon + jet doubly enriched with jets passing an EM filter:

1204 /GJet_Pt-20_doubleEMEnriched_TuneZ2_7TeV-pythia6/
 1205 Fall11-PU_S6_START42_V14B-v1/AODSIM

1206 4. W leptonic decays:

1207 /WJetsToLNu_TuneZ2_7TeV-madgraph-tauola/
 1208 Fall11-PU_S6_START42_V14B-v1/AODSIM

1209 5. $t\bar{t}$:

1210 /TTJets_TuneZ2_7TeV-madgraph-tauola/
 1211 Fall11-PU_S6_START42_V14B-v2/AODSIM

1212 A.0.2 Explanation of Naming Conventions

1213 • L: charged lepton

1214 • B: B hadron

1215 • C: D , or charmed, hadron

1216 • E: electron or positron

1217 • G: photon

1218 • W: W boson

1219 • Nu: neutrino

1220 • T: top quark

1221 • TuneZ2: Pythia tune incorporating 2010 LHC data with CTEQ6L1 [68] PDFs
 1222 [69]

1223 • M-50: Generated l^+l^- invariant mass threshold of 50 GeV

1224 • 7TeV: Generated center-of-mass energy 7 TeV

- 1225 ● **pythia6**: Parton showering and hadronization simulated with Pythia v6.424
- 1226 [70]
- 1227 ● **madgraph**: Hard interaction generated with MadGraph [71]
- 1228 ● **tauola**: τ decays generated with Tauola [72]
- 1229 ● **PU_S6**: Generated with S6 pileup scenario
- 1230 ● **START42_V14B**: Reconstructed with best alignment and calibration constants
1231 and magnetic field conditions as of August 3, 2011
- 1232 ● **Pt_XtoY**: $X \leq$ generated $\hat{p}_T < Y$
- 1233 ● **BCToE**: Enriched in B and D meson decays to electrons
- 1234 ● **doubleEMEnriched**: Enriched in electromagnetic jets

₁₂₃₅

Bibliography

- ₁₂₃₆ [1] S.L. Glashow, J. Iliopoulos, and L. Maiani, *Phys. Rev. D* **2** (1970) 1285; S.L.
₁₂₃₇ Glashow, *Nucl. Phys.* **22(4)** (1961) 579; J. Goldstone, A. Salam, and S. Weinberg,
₁₂₃₈ *Phys. Rev.* **127** (1962) 965; S. Weinberg, *Phys. Rev. Lett.* **19** (1967) 1264; A.
₁₂₃₉ Salam and J.C. Ward, *Phys. Lett.* **13(2)** (1964) 168.
- ₁₂₄₀ [2] M. Gell-Mann, *Phys. Lett.* **8** (1964) 214; G. Zweig, *CERN 8419/TH. 412* (1964)
₁₂₄₁ (unpublished).
- ₁₂₄₂ [3] J. Drees, *Int. J. Mod. Phys.* **A17** (2002) 3259.
- ₁₂₄₃ [4] P.W. Higgs, *Phys. Lett.* **12(2)** (1964) 132; P.W. Higgs, *Phys. Rev. Lett.* **13** (1964)
₁₂₄₄ 508; P.W. Higgs, *Phys. Rev.* **145** (1966) 1156.
- ₁₂₄₅ [5] I. Aitchison, *Supersymmetry in Particle Physics: An Elementary Introduction*
₁₂₄₆ (Cambridge University Press, Cambridge 2007), p. 4.
- ₁₂₄₇ [6] S. P. Martin, *A Supersymmetry Primer* **v4** (2006) 86. arXiv:hep-ph/9709356.
- ₁₂₄₈ [7] M. Dine and W. Fischler, *Phys. Lett.* **B110** (1982) 227; C.R. Nappi and B.A.
₁₂₄₉ Ovrut, *Phys. Lett.* **B113** (1982) 175; L. Alvarez-Gaumé, M. Claudson, and M.B.
₁₂₅₀ Wise, *Nucl. Phys.* **B207** (1982) 96; M. Dine and A.E. Nelson, *Phys. Rev.* **D48**
₁₂₅₁ (1993) 1277; M. Dine, A.E. Nelson, and Y. Shirman, *Phys. Rev.* **D51** (1995)
₁₂₅₂ 1362; M. Dine, A.E. Nelson, Y. Nir, and Y. Shirman, *Phys. Rev.* **D53** (1996)
₁₂₅₃ 2658.

- 1254 [8] A.H. Chamseddine, R. Arnowitt, and P. Nath, *Phys. Rev. Lett.* **49** (1982) 970; R.
 1255 Barbieri, S. Ferrara, and C.A. Savoy, *Phys. Lett.* **B119** (1982) 343; L.E. Ibáñez,
 1256 *Phys. Lett.* **B118** (1982) 73; L.J. Hall, J.D. Lykken, and S. Weinberg, *Phys. Rev.*
 1257 **D27** (1983) 2359; N. Ohta, *Prog. Theor. Phys.* **70** (1983) 542; J. Ellis, D.V.
 1258 Nanopoulos, and K. Tamvakis, *Phys. Lett.* **B121** (1983) 123; L. Alvarez-Gaumé,
 1259 J. Polchinski, and M. Wise, *Nucl. Phys.* **B221** (1983) 495.
- 1260 [9] P. Meade, N. Seiberg, and D. Shih, *Progr. Theor. Phys. Suppl.* **177** (2009) 143.
- 1261 [10] G. Aad et al., *CERN-PH-EP-2011-160* (2011).
- 1262 [11] T. Aaltonen et al., *Phys. Rev. Lett.* **104** (2010) 011801.
- 1263 [12] CMS Collaboration, *CMS-PAS-SUS-11-009* (2011).
- 1264 [13] <http://en.wikipedia.org/wiki/Tevatron>.
- 1265 [14] E. Fernandez et al., *Phys. Rev. Lett.* **54** (1985) 1118; E. Fernandez et al., *Phys.*
 1266 *Rev.* **D35** (1987) 374; D. Decamp et al., *Phys. Lett.* **B237(2)** (1990) 291; F.
 1267 Abe et al., *Phys. Rev. Lett.* **75** (1995) 613; S. Abachi et al., *Phys. Rev. Lett.* **75**
 1268 (1995) 618; G. Alexander et al., *Phys. Lett.* **B377(4)** (1996) 273; S. Aid et al.,
 1269 *Z. Phys.* **C71(2)** (1996) 211; S. Aid et al., *Phys. Lett.* **B380(3-4)** (1996) 461; B.
 1270 Aubert et al., *Phys. Rev. Lett.* **95** (2005) 041802.
- 1271 [15] O. Buchmueller et al., *CERN-PH-TH/2011-220* (2011).
- 1272 [16] <https://twiki.cern.ch/twiki/bin/view/CMSPublic/PhysicsResultsSUS>.
- 1273 [17] G. Aad et al., *JINST* **3** (2008) S08003.
- 1274 [18] B.C. Allanach et al., *Eur. Phys. J.* **C25** (2002) 113.
- 1275 [19] CMS Collaboration, *CMS-PAS-SUS-12-001* (2012).

- 1276 [20] A. Boyarsky, J. Lesgourgues, O. Ruchayskiy, and M. Viel, *CERN-PH-TH/2008-*
 1277 *234* (2009).
- 1278 [21] E. Komatsu et al., *Astrophys. J. Suppl. Ser.* **180** (2009) 330.
- 1279 [22] C.-H. Chen and J.F. Gunion, *Physical Review D***58** (1998) 075005.
- 1280 [23] F. Staub, W. Porod, J. Niemeyer, *JHEP* **1001** (2010) 058.
- 1281 [24] R. Brunelière, *Nucl. Instr. Meth. Res.* **A572** (2007) 33.
- 1282 [25] S. Chatrchyan et al. (CMS Collaboration), *JINST* **5** (2010) T03011.
- 1283 [26] CMS Collaboration, *CMS PAS EGM-10-002* (2010).
- 1284 [27] P. Meridiani and C. Seez, *CMS IN-2011/002* (2011).
- 1285 [28] P. Adzic et al. (CMS Electromagnetic Calorimeter Group), *Eur. Phys. J.* **C44S2**
 1286 (2006) 1.
- 1287 [29] P. Adzic et al. (CMS Electromagnetic Calorimeter Group), *JINST* **3** (2008)
 1288 P10007.
- 1289 [30] M. Malberti, *Nuc. Sci. Symposium Conference Record NSS/MIC IEEE* (2009)
 1290 2264.
- 1291 [31] S. Chatrchyan et al. (CMS Collaboration), *JINST* **5** (2010) T03010.
- 1292 [32] R. Paramatti, *J. Phys. Conf. Ser.* **293** (2011) 012045.
- 1293 [33] Y. Yang, [http://www.hep.caltech.edu/cms/posters/Pi0Poster_](http://www.hep.caltech.edu/cms/posters/Pi0Poster_CMSWeekDec2011.pdf)
 1294 CMSWeekDec2011.pdf (2011).
- 1295 [34] M. Anderson, A. Askew, A.F. Barfuss, D. Evans, F. Ferri, K. Kaadze, Y. Maravin,
 1296 P. Meridiani, and C. Seez, *CMS IN-2010/008* (2010).

- 1297 [35] <https://twiki.cern.ch/twiki/bin/view/CMS/ECALEnergyScaleCorrections>.
- 1298 [36] The H $\rightarrow \gamma\gamma$ working group, *CMS AN-2011/426* (2011).
- 1299 [37] M. Cacciari, *LPTHE-P06-04* (2006).
- 1300 [38] M. Cacciari, G.P. Salam, and G. Soyez, *CERN-PH-TH-2011-297* (2011).
- 1301 [39] S. Chatrchyan et al. (CMS Collaboration), *Phys. Rev. Lett.* **106** (2011) 082001.
- 1302 [40] A. Askew, B. Cox, D. Elvira, Y. Gershtein, M. Hildreth, D. Jang, Y.-F. Liu, D.
- 1303 Mason, D. Morse, U. Nauenberg, M. Paulini, R. Stringer, R. Yohay, and S.L.
- 1304 Zang, *CMS AN-2011/515* (2011).
- 1305 [41] F. Beaudette, D. Benedetti, P. Janot, and M. Pioppi, *CMS AN-2010/034* (2010).
- 1306 [42] M. Konecki, in Proceedings of the European Physical Society Europhysics Con-
- 1307 ference on High Energy Physics, Krakow, 2009, Eur. Phys.Soc. Mulhouse (ed.)
- 1308 (unpublished).
- 1309 [43] W. Adam, R. Früwirth, A. Strandlie, and T. Todorov, *J. Phys.* **G31** No. 9 (2005).
- 1310 [44] CMS Collaboration, *CMS PAS PFT-09-001* (2009).
- 1311 [45] CMS Collaboration, *CMS PAS PFT-10-002* (2010).
- 1312 [46] S. Chatrchyan et al., *JINST* **6** (2011) P11002.
- 1313 [47] CMS Collaboration, *CERN-PH-EP 2011-102* (2011).
- 1314 [48] M. Cacciari, G.P. Salam, and G. Soyez, *JHEP* **0804** (2008) 063.
- 1315 [49] G. Salam, talk given at CERN Theory Institute: SM and BSM Physics at the
- 1316 LHC (2009).
- 1317 [50] C.W. Fabjan and R. Wigmans, *Rep. Prog. Phys.* **52** (1989) 1519.

- 1318 [51] <http://www-cdf.fnal.gov/physics/new/top/2004/jets/cdfpublic.html>
 1319 (visited on 16 January 2011).
- 1320 [52] S. Chatrchyan et al. (CMS Collaboration), *JINST* **6** (2011) P09001.
- 1321 [53] CMS Collaboration, *CMS PAS JME-09-002* (2009).
- 1322 [54] T. Sjöstrand, S. Mrenna, and P. Z. Skands, *Comput. Phys. Commun.* **178** (2008)
 1323 852.
- 1324 [55] S. Chatrchyan et al. (CMS Collaboration), *JINST* **5** (2010) T03014.
- 1325 [56] J. P. Chou, S. Eno, S. Kunori, S. Sharma, and J. Wang, *CMS IN-2010/006*
 1326 (2010).
- 1327 [57] Y. Chen, talk given at a meeting of the CMS JetMET group (2011).
- 1328 [58] R. Korzekwa et al., *iEEE Trans. Elec. Dev.* **38** (1991) 745.
- 1329 [59] G. Daskalakis, D. Evans, C.S. Hill, J. Jackson, P. Vanlaer, J. Berryhill, J. Haupt,
 1330 D. Futyan, C. Seez, C. Timlin, and D. Wardrope, *CMS AN-2007/019* (2007).
- 1331 [60] F. James and M. Roos, *Comput. Phys. Commun.* **10** (1975) 343.
- 1332 [61] W. Verkerke and D.P. Kirkby, *CHEP-2003-MOLT007* (2003).
- 1333 [62] J.E. Gaiser, Ph.D. thesis, Stanford University (1982).
- 1334 [63] Information about all CMS datasets is available from the CMS Data Aggregation
 1335 System (DAS), located at the URL <https://cmsweb.cern.ch/das/>.
- 1336 [64] S. Chatrchyan et al., *Phys. Rev. Lett.* **106** (2011) 211802.
- 1337 [65] G. Aad et al. (ATLAS Collaboration), S. Chatrchyan et al. (CMS Collaboration),
 1338 and LHC Higgs Combination Group, *CMS-NOTE-2011/005* (2011).

- 1339 [66] A.L. Read, in *Proceedings of the First Workshop on Confidence Limits, Geneva,*
1340 2000, edited by L. Lyons, Y. Perrin, and F.E. James (CERN, Geneva, 2000), p.
1341 81.
- 1342 [67] G. Cowan, K. Cranmer, E. Gross, and O. Vitells, *Eur. Phys. J.* **C71** (2011) 1554.
- 1343 [68] P. M. Nadolsky, H.-L. Lai, Q.-H. Cao, J. Huston, J. Pumplin, D. Stump, W.-K.
1344 Tung, and C.-P. Yuan, *Phys. Rev.* **D78** (2008) 013004.
- 1345 [69] R. Field, talk given at LHC Physics Centre at CERN Minimum Bias and Un-
1346 derlying Event Working Group Meeting (2011).
- 1347 [70] T. Sjöstrand, S. Mrenna, and P. Z. Skands, *JHEP* **0605** (2006) 026.
- 1348 [71] dummy
- 1349 [72] dummy